



Dispersion and shattering strength of rocky and frozen planetesimals studied by laboratory experiments and numerical simulations

Arakawa, Masahiko ; Okazaki, Masashi ; Nakamura, Masato ; Jutzi, Martin ; Yasui, Minami ; Hasegawa, Sunao

(Citation)

Icarus, 373:114777

(Issue Date)

2021-12-06

(Resource Type)

journal article

(Version)

Accepted Manuscript

(Rights)

© 2021 Elsevier Inc. All rights reserved.

This manuscript version is made available under the CC-BY-NC-ND 4.0 license

<https://creativecommons.org/licenses/by-nc-nd/4.0/>

(URL)

<https://hdl.handle.net/20.500.14094/0100476423>



**Dispersion and shattering strength of rocky and frozen planetesimals studied by
laboratory experiments and numerical simulations**

Masahiko Arakawa^{1*}, Masashi Okazaki¹, Masato Nakamura¹, Martin Jutzi², Minami
Yasui¹, Sunao Hasegawa³

1. Graduate School of Science, Kobe University, Kobe 657-8501, Japan.
2. Physics Institute, Space Research and Planetary Sciences, University of Bern,
Gesellschaftsstrasse 6, 3012, Bern, Switzerland.
3. Institute of Space and Astronautical Science, Japan Aerospace Exploration Agency,
Sagamihara 252-5210, Japan.

*Author for Correspondence: Masahiko Arakawa, Graduate School of Science, Kobe
University, Kobe 657-8501, Japan; Tel: +81-78-803- 6684; Fax: +81-78-803-6684; E-
mail: masahiko.arakawa@penguin.kobe-u.ac.jp

Total pages: 52, including 28 figures and 3 tables.

Proposed running head: Dispersion and shattering strength of planetesimals

23 Abstract

24 We have developed a method to investigate the whole mass–velocity distribution of
 25 impact fragments generated by catastrophic disruption of simulated planetesimals. Flash
 26 X-ray radiography including 12 iron particles for tracers was used to visualize the interior
 27 of the target, and the velocity distribution of the whole target was estimated by using the
 28 velocities of the tracers measured by X-ray images. High-velocity impact experiments in
 29 the laboratory and numerical simulations were conducted for four types of targets
 30 simulating rocky and frozen planetesimals at various specific energies, Q . These targets
 31 consisted of frozen clays with three different water contents ranging from 25 to 45 wt.%
 32 and porous gypsum with a porosity of 51%. The shattering strength, Q_s^* , and the mass–
 33 velocity distribution (MVD) were studied for these targets. The Q_s^* of the frozen clays
 34 varied by a factor of 3-4 times, depending on the water content, and the Q_s^* for porous
 35 gypsum was almost the same as that for the frozen clays with lower water contents. The
 36 numerical impact simulations led to slightly different Q_s^* and MVD values for the frozen
 37 clay targets, possibly because of the partly ductile behavior of these samples. The MVDs
 38 resulting from the porous gypsum targets were well reproduced in the simulations. The
 39 cumulative mass of fragments with an ejection velocity slower than a specific velocity
 40 was examined to introduce a median velocity, v^* , charactering the mass–velocity
 41 distribution. The v^* is defined as the velocity at which the cumulative mass corresponds
 42 to a half of the original target mass in the distribution. The v^* values of the frozen clays
 43 were described by the empirical equation $v^* = \varepsilon Q^\gamma$ with almost the same ε and γ ,

irrespective of the water content, but the v^* of porous gypsum was about 1/3 that of the frozen clays. These experimental results were well reproduced by the numerical simulations for both frozen clays and porous gypsum targets. The dispersion strength, Q_D^* , could be derived by comparing v^* with the escape velocity, v_{esc} , of a target body with an effective mass, M , and radius, R . From this, a semi-theoretical equation showing the dispersion strength was derived: $Q_D^* = \left[\frac{1}{\varepsilon} \left(\frac{2GM}{R} \right)^{1/2} \right]^{1/\gamma}$. Numerical simulations of catastrophic disruptions including self-gravity were conducted to directly determine Q_D^* at large scale. These calculations showed that the effective mass of the target body, which is used in the computation of $v_{\text{esc}}=v^*$, should be a half of the original target mass, $M=M_{\text{target}}/2$. Our results suggest that this approach for computing the semi-theoretical dispersion strength is suitable for bodies larger than ~ 10 km.

Key words:

Asteroids, Catastrophic disruption, Planetesimals, Impact strength

1. Introduction

Catastrophic disruption of planetary bodies is one of the most important physical processes in the solar system. During the planetary accretion process in the solar nebula, planetary growth is generally followed by mutual collisions of planetesimals: Planetesimals are catastrophically disrupted into countless fragments by impact and a portion of these impact fragments are gravitationally re-accumulated to grow a planetary embryo, while other fragments that escaped from the embryo are relocate to the solar nebula. These fragments might sometimes reduce or enhance the planetary growth rate of a planetary embryo because they are easily removed by the inward drift to the sun or they are effectively captured by the atmosphere of a planetary embryo by gas drag (Kobayashi et al., 2010; 2011). In addition to these roles in the planetary growth process, catastrophic disruption is one of the main mechanisms inducing diversity of small planetary bodies such as asteroids, satellites of outer planets and trans-Neptunian Objects (TNOs). Especially in the asteroid belt region, there are many small bodies with a relative impact velocity of about 4 kms^{-1} (Bottke Jr. et al., 1994), so that mutual impacts among asteroids can sometimes induce catastrophic disruption and scatter numerous fragments, causing the size frequency distribution (SFD) of asteroids to undergo continuous change. The evolution of the SFD in the asteroid belt has been studied theoretically to elucidate the initial size distribution of planetesimals in the asteroid belt (Bottke et al. 2005). Moreover, it is widely accepted that asteroid families originated from the catastrophic disruption of parent bodies, and rubble-pile bodies such as asteroid (25143) Itokawa and (162173) Ryugu could be formed gravitationally through the re-accumulation of impact fragments

after the catastrophic disruption (Fujiwara et al., 2006; Watanabe et al., 2019). Therefore, impact strength is a key to controlling the planetary growth process and inducing a diversity of asteroids.

The impact strength is usually described by a specific energy, Q , which is the ratio of the projectile kinetic energy to the target mass in units of Jkg^{-1} , and it is defined as a specific energy when the largest fragment of the disrupted target is a half of the initial target mass. According to previous studies on the impact strength, the strength could be mainly controlled by the material strength in the so called strength regime at target sizes smaller than ~ 300 m, but at target sizes larger than ~ 300 m, it could be mainly controlled by the self-gravity; this is the so called gravity regime (Benz and Asphaug, 1999). Thus, the impact strength, Q^* , is described as a shattering strength, Q_S^* , for the strength regime and a dispersion strength, Q_D^* , for the gravity regime. The shattering strength has been studied in laboratory experiments for various materials simulating planetary bodies since the 1970s (e.g., Fujiwara et al., 1977; Takagi et al., 1984; Kawakami et al., 1983). The results of the material dependence on Q_S^* were summarized in Holsapple et al. (2002). Moreover, the effects of porosity on Q_S^* were reviewed in Collins et al. (2019), and the effect of multiple impacts on Q_S^* and the Q_S^* of compounds were studied by Yasui et al. (2014) and Yasui and Arakawa (2011), respectively, and the scale effects on Q_S^* were systematically studied by Housen and Holsapple (1999). According to these results, a scaling law for the catastrophic disruption was proposed based on a non-dimensional analysis or shock pressure decay in the target (Housen and Holsapple, 1990; Mizutani et al., 1990).

The dispersion strength in the gravity regime has been studied only by numerical simulations and not by laboratory experiments, because the re-accumulated mass of disrupted fragments is necessary to determine the Q_D^* . Numerical simulations are a suitable method to obtain the re-accumulated mass due to the self-gravity in the large-scale catastrophic disruptions. Previous theoretical studies showed that the Q_D^* increased with the increase of the target body to larger than 100 m to 10 km, but the size dependence of Q_D^* varies greatly depending on the models in more than one order of magnitude, although self-gravity must control the re-accumulation of impact fragments, not material strength. In order to clarify this discrepancy among the adopted models for Q_D^* , Jutzi (2015) studied the effects of material properties such as friction, cohesion, and compaction on Q_D^* , and found that these material properties affected the Q_D^* by one order of magnitude because the velocity distribution of the deformed target clearly depended on these properties and the deformation velocity was restricted by each dispersion mechanism. Thus, Jutzi (2015) mentioned that the material properties were still important factors to control the impact strength, although the gravity mainly dominated in this regime, and the Q_D^* could be determined by the velocity distribution of the deformed target after the catastrophic disruption.

Studies of the velocity distribution of impact fragments for various materials in laboratories are required to confirm the material dependence of Q_D^* obtained by Jutzi (2015), but these studies are very limited due to technical difficulties (Nakamura and Fujiwara, 1991; Giblin et al., 1998). One difficulty is the challenge of observing the fragments ejected from the target interior: The fragments formed at the interior are usually

hidden by the fragments formed on the surface and by the dusty cloud made of fine fragments. Another problem is the difficulty of tracing each fragment in order to obtain the velocity vector, because it is quite difficult to identify the same fragment in successive images taken by a high-speed video, and we also need to trace the same fragment in two different successive images taken from different directions in order to measure the velocity in 3-D. These are strong barriers to measurement of the velocity distribution of impact fragments.

Flash X-ray radiography has been used to observe small debris covered with a dusty cloud formed by a high-velocity impact (Mizusako et al., 2005), and Yasui et al. (2012) applied this technique to observe the crater cavity and the crack growth in a porous target. In this study, we used flash X-ray radiography to observe catastrophic disruption of the target, because this technique enabled us to see through the whole target, including the interior, without obstacles such as dusty cloud and overlapping fragments. We developed a new technique to measure the mass–velocity distribution of the target disrupted catastrophically, and we succeeded in obtaining the relationship between the impact fragment mass and the ejection velocity for most target masses. We then introduced a new parameter of a median velocity, v^* , which was defined as follows: One half of the original target mass had a velocity lower than v^* . We studied the material dependence of the v^* using frozen clays and a porous gypsum that collectively simulated various types of planetesimals, and these results were compared with the results of new numerical simulations, extending the study by Jutzi (2015) to confirm the theoretical model. Leinhardt and Stewart (2012) studied the scaling laws of catastrophic disruption in

gravity-dominated regime by mean of numerical simulations, and they introduced V^* as the impact velocity necessary for the impact strength. Our v^* showing the median velocity is a similar symbol to their V^* but v^* is different from V^* .

2. Experimental methods

2.1 Sample preparation

Impact experiments were conducted for two types of targets simulating frozen and rocky planetesimals, i.e., frozen clay targets simulating frozen planetesimals composed of an ice-rock mixture, and porous gypsum targets simulating rocky planetesimals with large porosity. Frozen clay targets were prepared by using bentonite powder and water. Bentonite is composed of clay minerals and the main component is montmorillonite. This bentonite powder was homogeneously mixed with water and kneaded, and then clay samples with water contents of 25 wt.%, 35 wt.%, and 45 wt.% were prepared. These clay samples were added to a hemispherical mold to form the initial target shape, and then additional clay mixture was piled up on the hemispherical mold to form a spherical target. The piled-up mixture was covered with another hemispherical mold to shape the upper hemisphere of the target. Finally, the spherical target was extracted from the two hemispherical molds. The target diameter was chosen to be 4, 5, 6, 7, and 9 cm for the impact experiments to obtain Q_s^* , and a target with a diameter of 6 cm was used for the flash X-ray radiography. For the X-ray radiography, iron tracer particles of 3 mm diameter were used to measure the displacement of the target interior, so that they were set at the

mid-plane of the target. These iron tracers were arranged on a plane surface that was added to the top of the first hemispherical mold before addition of the second hemisphere (Fig. 1a). The arrangement of iron tracers on the plane is shown in Fig.1b. Two squares with sides of 2 and 4 cm were drawn on the plane, with their centers being the same as the center of the circle describing a cross section of the target. On the large square, tracers were set at the corners and at the midpoint of each side. On the small square, tracers were set only at the midpoint of each side. In this manner, 12 tracers were set on the plane; for purposes of identification, they were numbered from #1 to #12. The projectile was launched in the direction of the center line passing through tracers #2 and #11, and it impacted the point on the target surface crossing the center line shown in Fig.1b; hereafter we call this the aiming point.

Fig. 1

The shaped clay samples were frozen in a freezer at -20°C for more than 5 hrs (Fig. 2a), and kept in the freezer until just before the impact experiment. The bulk densities of the frozen clay targets with water contents of 25 wt.% (FC25), 35 wt.% (FC35), and 45 wt.% (FC45) were 1.67 g cm³, 1.57 g cm³, and 1.42 g cm³, respectively, and the tensile strengths of FC25 and FC45 were measured to be 2.24 MPa and 1.10 MPa at -15°C, respectively. The bulk sound velocities of FC25 and FC45 were also measured to be 2.19 km s⁻¹ and 2.38 km s⁻¹ at -15°C, respectively. The bulk densities of these frozen samples indicated that they did not have a sufficient number of pores to increase the interior porosity to more than 5%.

Fig. 2

Porous gypsum targets were prepared by using commercial CaSO₄·1/2H₂O powder and water, which were mixed to form a slurry that was poured into a spherical mold. The

preparation method was the same as that in Yasui et al. (2020). The twelve iron tracers were placed on the middle plane in the same arrangement as for the frozen clay target. The prepared porous gypsum targets had a spherical shape with a diameter of 60 mm, and the bulk density and the porosity were calculated to be 1.12 g cm^{-3} and $51 \pm 1\%$ (Fig. 2b). The tensile strength and the bulk sound velocity were estimated to be 2.3 MPa and 1.42 km s^{-1} based on the previous results (Yasui et al., 2020).

2.2 Impact experiments

Impact experiments were conducted by using a two-stage light gas gun located at the Institute of Space and Astronautical Science (ISAS), Japan Aerospace Exploration Agency (JAXA), and the same type of gun located at Kobe University. Flash X-ray radiography was only conducted at ISAS/JAXA, and impact recovery experiments for frozen clays were only performed in the cold room equipped with a gun at Kobe University. At ISAS/JAXA, a spherical polycarbonate (PC) projectile with a diameter of 7 mm and a mass of 228 mg impacted a target with a diameter of 6 cm in a head-on collision at a velocity from 1 km s^{-1} to 6 km s^{-1} (Table 1). The corresponding specific energy was from 1.2×10^3 to $2.5 \times 10^4 \text{ J kg}^{-1}$, which was **large enough** to disrupt the target catastrophically, with most of the largest fragments being less than 10% of the original target mass. Since these experiments were made at room temperature, all of the impact fragments of frozen clays except for the largest fragment were melted to form a slurry soon after the shot. Thus, we were not able to recover these melted fragments to measure the mass distribution, and it was difficult to determine Q_S^* using only the recovered

Table 1

fragments at ISAS/JAXA.

Impact disruption was observed by not only flash X-rays but also a high-speed camera, and both systems were triggered by a PVDF gauge attached to the metal platform (Fig. 3a-d): When the projectile passed through the gauge, the observation systems were triggered with appropriate delays. The high-speed camera (HPV-X; Shimazu Co.) observed the impact disruption from the direction perpendicular to both the irradiation of the CH3 and the projectile trajectory. The camera took images at 1×10^5 FPS with an exposure time of $4 \mu\text{s}$ or 2×10^5 FPS with an exposure time of $6 \mu\text{s}$, and these images were used to determine the impact point on the target surface together with the X-ray image from the CH3 and to measure the antipodal velocity, which was the expansion velocity of the ejecta envelope at the point antipodal to the impact point.

Fig. 3

2.3 Impact disruption in a cold room

We then conducted impact experiments for frozen clay targets in a cold room of Kobe University kept at -15°C and recovered all fragments without melting after the shot. In these experiments, a spherical PC projectile with a diameter of 4.7 mm and mass of 68 mg impacted the target in a head-on collision at a velocity of 2.5 km s^{-1} . The target diameter was changed from 4 cm to 9 cm to control the specific energy from 3.7×10^2 to $5.9 \times 10^3 \text{ J kg}^{-1}$, and the Q_S^* was determined for the frozen clay targets (Table 2). The target was set in a transparent acrylic recovery box; a hammock-like support net made of thin threads was hung from the ceiling of the box, and the target was placed on the net before the shot. The inside of the recovery box was covered with sponge except for the two sides

Table 2

used as the optical windows in order to prevent impact fragments from being disrupted by collisions with the box walls. The recovery box was set in a large vacuum chamber with large transparent windows to observe the impact and evacuated below 100 Pa before the shot. Impact disruptions were observed from the side through these two transparent windows by using a high-speed digital video camera (Phantom v1612; Vision Research) (see Yasui et al., (2020)). The camera recorded the images at 10^5 frames per second and the exposure time was 380 ns. After the shot, impact fragments were taken from the recovery box in the cold room and each fragment with a size larger than 9.5 mm was measured by an electric mass balance. Small fragments were sifted by using sieves with different opening sizes of 1, 2, 4, 9.5 mm, and the total mass remaining on each sieve was measured to construct the fragment mass distribution (Fig. 4). The average mass of one fragment remaining on each sieve was estimated by the total mass of 100 fragments, and this average fragment was used to calculate the number of fragments remaining on each sieve. The total mass of the recovered fragments was greater than 90% of the initial target mass.

Fig. 4

2.4 Flash X-ray radiography

Flash X-ray radiography was performed by using a method similar to that described in Yasui et al. (2012). Three 300 kV flash X-ray tubes (Model 43733A; L-3 Communications) were equipped on a large vacuum chamber of the horizontal-type gas gun at ISAS/ JAXA, and the installed directions of these tubes are shown in Fig. 3a-d. The CH3 tube is installed at the top of the chamber normally, and the CH1 tube and the

CH2 tube are installed at positions rotated 45° clockwise and counterclockwise from the launching direction, respectively. An imaging plate (IP) was set at the side opposite each flash X-ray tube, and the X-rays passing through the target from three different directions were observed by the IPs. The CH1, CH2, and CH3 were observed by the IP1, IP2, and IP3, respectively, so each IP was set perpendicular to the X-ray irradiation, with the IP1 and IP2 being inclined 45° from the floor. The target was placed on a hammock-like support net hung from a metal platform (Fig. 3a-c) in the vacuum chamber. In order to coordinate the direction of the X-ray irradiation with the iron tracers set at the middle plane of the target (hereafter called a tracer plane), a target was placed so that the tracer plane was perpendicular to the direction of irradiation from the CH3 and the aiming point was on the projectile trajectory. To avoid melting, the placement of the frozen clay targets was carried out as soon as possible after the targets were taken from the freezer. Before the shot, the vacuum chamber was evacuated below 100 Pa, and the target was thermally insulated from the chamber wall. Though the target surface was partially melted during the preparation, the surface refroze during the evacuation. The porous gypsum target was impacted at the vacuum condition below 3 Pa, and the impact fragments were recovered after the shot to measure their masses.

The initial positions of the iron tracers were imaged by X-ray radiography from three directions before the shot, and these images were compared with that taken after the shot and used to measure the displacements of each tracer. During the impact disruption, each flash X-ray tube was triggered at between $5\ \mu\text{s}$ and $2\ \text{ms}$, with an irradiation duration of 30 ns after the impact of the projectile on the target surface. We preset the irradiation

timings— t_1 , t_2 , and t_3 for CH1, CH2, and CH3, respectively—as $t_3 < t_2 \leq t_1$. Most observations for frozen clay targets were made at $t_2 < t_1$ to examine the variation of tracer velocities with time, but several observations were made at $t_2 = t_1$ to determine tracer positions in three dimensions precisely. For porous gypsum targets, all the observations were made at $t_2 = t_1$. The X-ray image from CH3 was used to determine the impact point and to support the measurement of tracer velocities in the components perpendicular to the irradiation.

2.5 Analysis of X-ray images

2.5.1 Tracer positions

Figure 5 shows typical X-ray images of a frozen clay target taken before the shot (Run no. 170224-1), which were used to determine the initial positions of tracers in a target; these figures correspond to the images of IP1, 2 and 3 irradiated from CH1, CH2, and CH3, respectively. The twelve iron tracers are well recognized in these images as small circles darker than the surrounding area, because the mass absorption coefficient and the density of iron are several times larger than those of the oxides making up the targets, and thus the tracers absorb the X-rays more effectively than the surrounding material. We can then easily derive the position of the center of each tracer in these images. Since Fig. 5a and c were taken by the irradiations inclined 45° from the tracer plane, the horizontal interval between neighboring tracers is shrunk to $1/\sqrt{2}$ times the interval on the tracer plane, though the vertical interval is the same as that on the tracer plane.

Fig. 5

In order to determine the displacement of each tracer during the disruption, we

measured the position vector of each tracer by using the Cartesian coordinate system shown in Fig. 6a and b. The origin of this coordinate system is the center of the target; the y -axis is defined as the direction of the projectile trajectory, with the downward direction being positive. The plane including both the x and the y axes is perpendicular to the gravity direction; the right side of the x -axis from the perspective of the direction of the projectile is positive. The z -axis is directed vertically, and the upward direction is positive. The tracer plane is usually in the x - y plane, but it tilted slightly into the x - y plane from time to time due to the unavoidable difficulty of target setting. The plane including IP1 (IP1 plane) and that including IP2 (IP2 plane) inclined 45° clockwise from the x - y plane and from the z - y plane, respectively (Fig. 6b), so we can define another Cartesian coordinate system rotating around the y -axis 45° clockwise: the IP1 plane is in the x' - y plane and the IP2 plane is in the z' - y plane. The position vector measured in this $x'y'z'$ coordinate system can be converted to the position vector in the xyz coordinate system using a rotation matrix with $\delta = -45^\circ$; the coordinate conversion is thus as follows:

$$\begin{pmatrix} x \\ y \\ z \end{pmatrix} = \begin{pmatrix} \cos \delta & 0 & \sin \delta \\ 0 & 1 & 0 \\ -\sin \delta & 0 & \cos \delta \end{pmatrix} \begin{pmatrix} x' \\ y \\ z' \end{pmatrix} \quad (1).$$

The displacement of each tracer was measured by overlaying the post-impact image on the pre-impact image; that is, each tracer was identified on both the pre- and the post-impact image, and the center of an individual tracer was positioned on both images so that the displacement vector between them could be measured (e.g., Fig. 7). We thus used the post-impact images of IP1 and IP2 taken at the same time point together with their pre-impact images to determine the 3-D displacement vectors of tracers. Since the

Fig. 6

Fig. 7

displacement vector, $\vec{d}' = (d'_x, d'_y, d'_z)$, of each tracer was measured in the $x'y'z'$ coordinate system, this vector was converted to the displacement vector, $\vec{d} = (d_x, d_y, d_z)$, in the xyz coordinate system by using the rotation matrix of Eq. (1), where d_y measured on both the IP1 and IP2 images was the same theoretically, so d_y was adopted as the average of these values.

The velocity vector \vec{v} of each tracer in the laboratory system was simply calculated from \vec{d} and the interval of the X-ray irradiation, Δt , as follows:

$$\vec{v} = (v_x, v_y, v_z) = (d_x/\Delta t, d_y/\Delta t, d_z/\Delta t). \quad (2)$$

The velocity vector \vec{V} of each tracer in the center-of-mass system was also derived using the velocity of the center-of-mass, v_g . The velocity components of the v_g are assumed to be only along the y -axis, and calculated by $v_g = m_p v_i / (m_p + M_t)$, where m_p and M_t are a projectile and a target mass, respectively, and v_i is an impact velocity in the laboratory system. \vec{V} is written as follows:

$$\vec{V} = (V_x, V_y, V_z) = (v_x, v_y - v_g, v_z). \quad (3)$$

The flash X-ray timing of t_1 and t_2 for most frozen clay targets was set to be $t_1 > t_2$, so that no IP2 images were available to obtain 3-D vectors in most cases. In these cases, we assumed that each tracer moved in uniform linear motion and constructed the IP2 image at t_1 by multiplying the displacement vector of each trace by t_1/t_2 , and the modeled IP2 images were used for the analysis together with the IP1 images. The time dependence of the tracer motion was studied as described in section 4.4, and the uniform linear motion of the tracer was almost always within the margin of error.

2.5.2 Impact point and antipodal velocity

The projectile was launched toward an aiming point, but the impact point was scattered slightly to achieve variance in the velocity distribution of tracers. We then derived the impact point using the images taken by the high-speed camera and that obtained from IP3. The latitude of the impact point, θ , was measured by using the high-speed camera image (Fig. 8a). We were able to trace the projectile trajectory at an impact velocity slower than 2 km s^{-1} . The impact point was then determined as the cross point between the trajectory and the target surface; we defined a head-on collision as the impact at the latitude of 90° . At a velocity higher than 2 km s^{-1} , the projectile was not observed due to the strong emission of light from plasma of a PVFD gauge evaporated by the collision of a projectile. We instead used the ejecta curtain to determine the impact point; this method is similar to that used in Yasui et al. (2020). In this case, we assumed that the ejecta curtain was axial symmetrical against the line connecting the impact point to the target center, and we determined the neck of the eject curtain as shown in Fig. 8a. The impact point was the cross point between the target surface and the vertical bisector of the line linking both ejecta necks. The θ is defined to be positive on the upper hemisphere. The longitude of the impact point, ϕ , was measured by using the image of IP3 in Fig. 8b and c. We can usually observe the axisymmetric crater cavity in early stage of the catastrophic disruption as shown in Fig. 8b and c, so we compared the pre-impact image of IP3 with this cavity and determined the intersections between the crater cavity and the figure of the target in the pre-impact image. The impact point was the cross point between the target surface and the vertical bisector of the line linking both these intersections; we

Fig. 8

defined a head-on collision as the impact at the longitude of 0° . The ϕ is defined to be positive on the right side of an impact axis. We define an impact axis as the line which connects the impact point with the antipodal point. An antipodal point is often chosen to be a position showing the representative fragment velocity, and for our present purposes it was determined as the intersection point between the line connecting the impact point with the target center and the downward target surface (Fig. 8b and c).

3. Numerical simulation

For the impact simulations, we use a Smoothed Particle Hydrodynamics (SPH) impact code (Benz and Asphaug, 1994; 1995; Nyffeler, 2004; Jutzi et al., 2008; Jutzi, 2015) that includes self-gravity as well as material strength models. To model fractured, granular material, a pressure-dependent shear strength (friction) is included by using a standard Drucker-Prager yield criterion (Jutzi, 2015). Porosity is modeled using a sub-resolution approach based on the P -alpha model (Jutzi et al., 2008), taking into account the enhanced dissipation of energy during the compaction of porous materials. We further use the Tillotson Equation of State (EOS) with parameters as discussed below.

3.1 Modelling frozen clay targets

To model the impacts in frozen clay targets, we use non-porous targets with initial bulk densities that correspond to those in the experiments described in section 2.1. The bulk modulus (leading term of the Tillotson EOS) is set to $A = 0.7 \times 10^{11}$ dyn/cm². This leads to a bulk sound speed of ~ 2.2 km/s, which is roughly consistent with the measured

bulk sound velocities of 2.19 km/s (FC25) and 2.38 km/s (FC45), respectively (Table 2). We further set the parameter $B = A$, while for the remaining Tillotson parameters we use basalt values. For the tensile fracture model, we use Weibull parameters that lead to tensile strengths of ~ 1 MPa and ~ 2 MPa, respectively (see Jutzi et al., 2009 for the estimation of the tensile strength from these parameters).

For the yield curve (see Jutzi, 2015), we use a cohesion of $Y_0 = 2$ MPa and a coefficient of friction of 0.2 (for both the “internal friction” and the “damaged friction”). As discussed in section 4.6.1, such a low value is required to match the measured velocity distribution.

3.2 Modelling porous gypsum targets

To model the impacts in gypsum targets, we use the same approach and parameters as in the simulations carried out by Jutzi (2015). However, we use Weibull parameters which result in a slightly higher minimum strain threshold for failure (4×10^{-5} instead of 3×10^{-5} ; see Jutzi, 2015) and a corresponding tensile strength which is ~ 2 MPa (instead of 1.5 MPa in Jutzi, 2015). As discussed in section 4.6.2, the shattering strength found in the experiments presented here is slightly different from the one in the previous experiments (although this is at least partly explained by the different mass ratio of projectile/target).

3.3 Initial conditions

For both the frozen clay and gypsum targets we simulate impacts using the same

initial conditions (mass and velocity of impactor; target mass) as in the experiments. We use runs 171110-3, 170913-1, 171025-4, 170608-4, 170727-3, 170608-3 for frozen clay and runs 180329-5, 180329-4, 180912-2, 180328-1, 180328-2, 180913-1, 180329-3, 180329-2, 180329-1 for gypsum (see Table 1). We then compute the resulting fragment size as well as the velocity distribution for comparison with the experimental results. In addition, we perform impact simulations at large scale in order to verify the extrapolation of Q_D^* (section 5.2).

4. Results

4.1 Shattering strength

The largest fragment mass of the impact fragments, m_l , was measured to determine the shattering strength, Q_S^* , of frozen clays (FC) and porous gypsum. The Q_S^* is defined as the specific energy at which the largest fragment mass was a half of the original target mass, M_t , and it was conventionally obtained from the relationship between Q and m_l/M_t . Figure 9 shows the m_l/M_t for the targets of FC25, FC35, FC45, and porous gypsum in this experiment together with previous results for water ice, basalt and porous gypsum (Arakawa, 1999; Fujiwara and Tsukamoto, 1977; Yasui et al., 2020). The data for FC25 are well mixed with those for FC35, so the difference in their shattering strength is not recognized, and both data are fitted by the same power law equation as follows:

$$\frac{m_l}{M_t} = a Q^{-b} , \quad (4)$$

where $a=10^{2.69 \pm 1.54}$ and $b=1.05 \pm 0.41$, and then the Q_S^* is derived to be $705_{-521}^{+563} \text{ J kg}^{-1}$.

Fig. 9

429 The data of FC45 are also fitted by Eq. (4), and then we derive $a=10^{1.95\pm0.50}$, $b=0.98\pm0.16$,
 430 and $Q_s^*=198_{-62}^{+61} \text{ J kg}^{-1}$. The shattering strength of FC25 and FC35 is similar to that of
 431 basalt, $Q_s^* = 709 \text{ J kg}^{-1}$, although the static tensile strength of basalt, 19 MPa (Nakamura
 432 et al., 2007), is several times larger than that of 2.24 MPa for FC25. It is well known that
 433 the porosity is able to increase the shattering strength because the impact energy could be
 434 consumed by pore collapse effectively: Porous gypsum targets with a porosity of 50%
 435 show the largest shattering strength in Fig. 9a. The porosity of FC25 and FC35 could be
 436 less than 5%, so the porosity effect might be quite limited to their shattering strength. The
 437 shattering strength of FC45 is in between that of water ice and basalt, so the Q_s^* of FC45
 438 is larger than that of water ice, though the static tensile strength of water ice, $\sim 1 \text{ MPa}$
 439 (Schulson and Duval, 2009), is similar to that of FC45. The Q_s^* of FC25 and FC35 is
 440 larger than that expected from the tensile strength of crystalline rocks, and this behavior
 441 could not be explained by their porosity. However, the Q_s^* of FC45 is smaller than that
 442 of FC25, and the shattering strength has a good correlation with the static tensile strength:
 443 The tensile strength of FC45 is smaller than that of FC25. Thus, we speculate that the
 444 ductile behavior of FC samples might be important to control the shattering strength,
 445 because the impact-induced heating just below the impact point might change the frozen
 446 target from brittle to ductile to reduce crack growth. Nonetheless, a detailed study of the
 447 mechanism by which the Q_s^* of FC samples is enhanced is beyond the scope of this paper,
 448 and it should be clarified in the future. The data of porous gypsum targets are fitted by
 449 Eq. (4), and we derived them to be $a=10^{2.09\pm0.38}$, $b=0.83\pm0.09$, and $Q_s^* = 760_{-238}^{+268} \text{ J kg}^{-1}$;
 450 our Q_s^* for porous gypsum was thus a half of that reported in the previous study (Fig.

9b). This difference might have been caused by the difference in the mass ratio of the project to the target: The previous study used a mass ratio that was one third of that used here.

4.2 Mass frequency distribution

The mass frequency distributions of the recovered impact fragments for frozen clay and porous gypsum targets are shown in Fig. 10a-c. These figures show the relationships between the cumulative number of fragments and the fragment mass normalized by the original target mass for FC45, FC25 and FC35, and the porous gypsum targets, respectively. All the figures of these distributions showed the same features—namely, the fragment mass at the cumulative number of 1, m_1/M_t , decreased with the increase of the specific energy, and the total number of fragments increased with the increase of the specific energy, as was recognized in the previous studies (Yasui et al., 2020). Furthermore, these figures showed the similar characteristic that the distributions could be approximated by the power law equation of $N = N_0(m/M_t)^{-\alpha}$, which has been reported in previous studies for the impact disruption of rocks, water ice, etc. The α of FC45 was obtained as 0.85 (± 0.15), and those of FC25 and FC35 were obtained as 0.74 (± 0.05), and these values were slightly larger than that obtained for water ice, 0.66, by Arakawa (1999). Moreover, the α of porous gypsum was determined to be 0.66 (± 0.05), which is slightly smaller than the α of 0.75 obtained for porous gypsum by Yasui et al. (2020).

Fig. 10

The recovered fragments from the FC45 target of Run no. 170922-2 are shown in Fig.

4. As can be seen, a portion of the largest fragment might be removed by spallation to form a core-like shape, and thus the FC45 target may show a core-type disruption like those typical for non-porous rocky materials. However, other targets of FC25, FC35 and porous gypsum do not show a core-type disruption. Small fragments of frozen clay and porous gypsum targets exhibited irregular shapes that were lumpy or sharp (Fig. 11a, b); these could have been formed by brittle failure caused by shear and tensile crack growth.

Fig. 11

4.3 Antipodal velocity

The relationships between antipodal velocity, v_a , and specific energy, Q , for frozen clays and porous gypsum are shown in Fig. 12a and b, along with previous results for water ice, basalt and porous gypsum. The measured v_a was found to increase with the increase of the specific energy, and the v_a of FC45 targets was slightly below that of basalt and almost parallel to that in the previous relationships (Fig. 12a). These v_a values with a dimension of ms^{-1} were fitted by a power law equation:

Fig. 12

$$v_a = c Q^d, \quad (5)$$

where c and d were determined to be $10^{-1.91 \pm 0.20}$ and 0.847 ± 0.055 , respectively. The obtained d is slightly higher than that of the previous results: 0.76 for basalt, 0.71 for water ice, and 0.78 for porous gypsum (Fujiwara and Tsukamoto, 1980; Arakawa, 1999; Yasui et al., 2020). The v_a values for FC25 and FC35 were well mixed, and a significant difference was not recognized, as it was found that both FC targets had very similar shattering strength. They were then fitted together; the values of c and d were $10^{-2.24 \pm 0.36}$ and 0.882 ± 0.095 , respectively. These values were slightly below that of the FC45 targets,

but the difference among these three types of FC targets was not significant. Then, all the data of three types of FC targets were fitted together to derive c and d ; they are $10^{-1.67 \pm 0.19}$ and 0.757 ± 0.052 , respectively. On the other hand, the v_a of FC targets was clearly higher than that of porous gypsum targets (Fig. 12a). The v_a of our porous gypsum targets was well consistent with the previous results obtained by Yasui *et al.* (2020) although a small offset can be seen due to the difference of the porosity $\sim 4\%$ between them (Fig. 12b).

When we compare the results of the largest fragment mass and the antipodal velocity obtained for the targets including the tracers with those obtained for the targets without tracers, there were no clear difference between them as shown in Fig. 9 and 12. Thus, it could be reasonable to think that the effects of tracers inside the targets were too small to affect the catastrophic disruption process clearly in these experiments

4.4 Flash X-ray images

Figure 13 (a–c) shows the flash X-ray images taken at various time points after the impact for frozen clay targets of FC45, and these targets were impacted at different projectile velocities from 1.42 km s^{-1} to 3.75 km s^{-1} and specific energies from $1.4 \times 10^3 \text{ J kg}^{-1}$ to $9.6 \times 10^3 \text{ J kg}^{-1}$. Figure 13a shows successive images of the disrupted target for Run no. 170609-2 taken at $100 \text{ }\mu\text{s}$ (left panel), $500 \text{ }\mu\text{s}$ (middle panel) and 1 ms (right panel) after the impact. In these images, the projectile was impacted at 1.42 km s^{-1} . In the left panel, the impact crater and the ejecta curtain are found around the impact point, but we cannot recognize the motion of each tracer and the cracks generated inside the target. In the middle panel, we can find many white lines showing open cracks and visible motions

Fig. 13

of iron tracers at the hemisphere including the impact point (we call this the impact hemisphere), but these white lines do not appear around the antipodal point. In the right panel, there are many fragments as small as several mm formed at the impact site, and it is recognized that the motions of iron tracers are large in the impact hemisphere. At the hemisphere including the antipodal point (we call this the antipodal hemisphere), there are several cracks that generate relatively large fragments and the iron tracers move a small distance. Figure 13d shows the velocity vector of each iron tracer on the x - y plane (left panel) and y - z plane (right panel) in the center-of-mass system (CMS); these vectors were obtained from Fig. 13a according to the analytical method introduced in section 2.5.1. As the projectile impacts just at the edge of the tracer plane, at a point called the aiming point, the velocity components of the z -axis are quite small and the tracers move only on the x - y plane. In the left panel, the tracers in the central region remain almost stationary because this region moves at the velocity of the center-of-mass system, and the fragments located at the antipodal hemisphere move at a velocity as small as 10 m s^{-1} toward the impact direction called downstream. On the other hand, the region close to the impact site moves at the direction opposite to the impact direction, called upstream, at a velocity from 20 to 30 m s^{-1} .

Figure 13b provides successive images of the disrupted target for Run no. 170727-1 taken at $250 \text{ } \mu\text{s}$ (left panel), $750 \text{ } \mu\text{s}$ (middle panel) and 1.5 ms (right panel) after the impact, and the projectile impacts at 2.07 km s^{-1} . In the left panel, the impact crater is found to grow as large as the target radius and many vertical cracks are also found to grow from the crater floor toward the interior. The tracers with initial positions inside the crater are

539 recognized to move at a large distance. In the middle panel, the target is full of cracks and
 540 completely disrupted into small pieces, and the small fragments with a size similar to the
 541 tracer align with each other to form an arch shape. The antipodal hemisphere almost
 542 maintains its initial round shape, but then deforms to widen the width. The size of the
 543 fragments appears to be finer close to the impact site, and this tendency is clearer in the
 544 right panel. At 1.5 ms after the impact, every tracer is distinctively found to have moved
 545 a large distance, and the ejected fragments are observed to form a fan shape with the pivot
 546 located close to the antipodal point. The velocity vectors in the y - z plane are shown in
 547 the right panel of Fig. 13e, and we notice that the z component of each vector is relatively
 548 small except in the case of the tracers close to the impact point, because the projectile
 549 almost impacts at the aiming point. The initial positions of tracers near the impact point
 550 are slightly deviated from the tracer plane, so these tracers could be accelerated toward
 551 the z -axis. The characteristics of the distribution of the tracer's vectors in the x - y plane
 552 are qualitatively similar to those in Fig. 13d: The minimum velocity is found at the central
 553 region, though the maximum velocity is as high as 40 m s^{-1} and the velocity at the central
 554 region is less than 10 m s^{-1} .

555 Figure 13c shows successive images of the disrupted target for Run no. 171025-4
 556 taken at $50 \text{ }\mu\text{s}$ (left panel), $750 \text{ }\mu\text{s}$ (middle panel) and $750 \text{ }\mu\text{s}$ (right panel) after the impact,
 557 with the projectile impacted at 3.75 km s^{-1} . In the left panel, the hemispherical crater
 558 cavity with a diameter larger than the target radius is found to form even at $50 \text{ }\mu\text{s}$ after
 559 the impact, and the tracers have moved slightly everywhere in the target. The target is
 560 completely disrupted into small pieces at $750 \text{ }\mu\text{s}$, and it deforms into a characteristic

crescent-like shape with a sharp boundary. Moreover, this crescent area is divided into several domains composed of small fragments by many thick cracks (indicated by white lines). Unlike in the images in Fig. 13a and b, these fragment sizes appeared to be independent of their initial positions. The velocity vectors of tracers in the x - y plane are symmetric to the impact axis in Fig. 13f, and the velocity component of the z -axis is smaller than that of other components, as shown in the right panel of Fig. 13f, because the projectile impacts at the aiming point. All the tracers move radially from the impact point, and the velocity is fastest around the impact point and slowest in the target center. Since the difference in the velocity components along the y -axis is so large between the impact hemisphere and the antipodal hemisphere, the shape made of the fragments appears to be deformed and compressed along the impact axis and forms a crescent-like figure. Based on the images in Fig. 13d-f, it is clear that all the tracers accelerated faster as the specific energy increased.

Figure 14 shows the effects of the shattering strength on the velocity distribution of tracers at the constant specific energy of $5 \times 10^3 \text{ J kg}^{-1}$; Figures 14a and b show successive X-ray images for the frozen clay targets of FC45 and FC25, respectively. It is very clear that the impact fragment sizes are quite different in the right plates of each figure taken at 0.75 or 1 ms, because the shattering strength of the frozen clay FC45 is about four times smaller than that of FC25 according to Fig. 9a. The envelopes constructed from the impact fragments of these targets look quite different, and their appearance depends on the shattering strength. The fine fragments of FC45 distribute to form an envelope resembling a bow in Fig. 14a, but the FC25 target yields fewer fine fragments than the FC45 target,

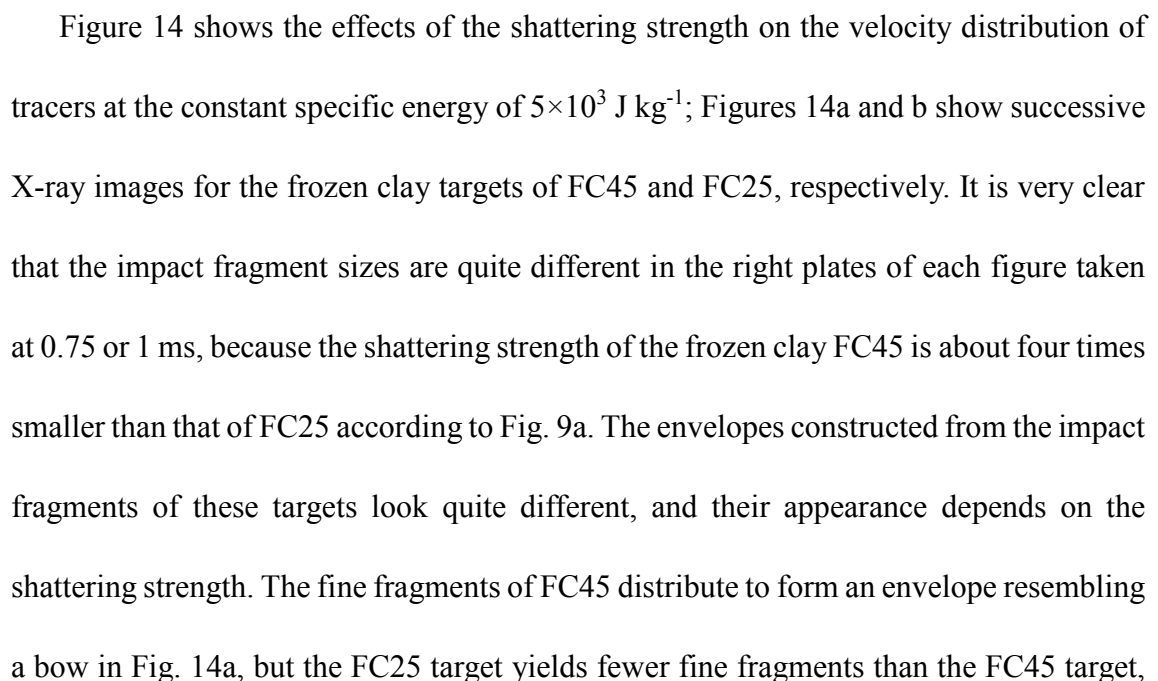

 Figure 14 consists of two side-by-side X-ray images, labeled (a) and (b), showing the impact fragments of frozen clay targets. Image (a) shows the fragments of FC45, which are distributed in a bow-like shape. Image (b) shows the fragments of FC25, which are fewer and more distinct. The images are taken at 0.75 ms and 1 ms after impact.

Fig. 14

and the antipodal hemisphere of the former is not completely disrupted. Thus, large fragments divided by several vertical cracks still remain at the antipodal hemisphere and the initial target shape can be recognized. On the other hand, the velocity vectors of each tracer in the x - y plane for FC45 and FC25 in the left panels of Fig. 14c and d are very similar for the tracers having the same initial tracer position, although the velocity vectors on the y - z plane in the right panels of Fig. 14c and d are slightly different depending on the difference in the tracer initial positions and the impact point.

Figure 15 (a and b) shows a comparison of the flash X-ray images of the frozen clay of FC45 with those of the porous gypsum when these targets were impacted at the same specific energy of 10^4 J kg^{-1} , and clearly illustrates the effects of these target materials on the velocity distribution of tracers. Because of the difference in the shattering strength between FC45 and porous gypsum, the disrupted fragments found in the middle and right panels of Fig. 15a are rather smaller than those found in Fig. 15b. We already showed that the velocity distribution of tracers for F45 and F25 at the same specific energy was almost the same, although the impact fragments of FC45 were smaller than those of FC25 (Fig. 14c and d). But it is quite noteworthy that the velocity distribution of tracers in the FC45 target is quite different from that in the porous gypsum (Fig. 15b and d), despite the specific energy being nearly equivalent between the two cases. The maximum velocity of tracers in the porous gypsum was about 30 ms^{-1} , and the original round shape of the target was maintained in the antipodal hemisphere (Fig. 15b and d). In contrast to the velocity of the tracers in porous gypsum, the maximum velocity of tracers in FC45 was greater than 80 ms^{-1} , and all of the tracers moved higher than those in the porous gypsum.

Fig. 15

Moreover, the change in velocity that occurred with the change in initial position was larger in the FC45 target, so the fragments moved to form a crescent-like shape in Fig. 15a and c.

The reproducibility of the impact experiments was studied by repeating the experiment under the same impact condition and taking the images at different time points from 0.5 ms to 1 ms after the impact. Figure 16 shows the tracer velocities in the center-of-mass system depending on the initial position for the three different runs (Run nos. 171025-3, 171025-4, 171025-5), and the horizontal axis is the distance from the impact point to the initial positions of each tracer set. The projectile impacted close to tracer #2. Although the fluctuation in the tracer velocity was a little bit large for tracers #1 and #3, which had initial positions near the impact point, the reproducibility of the tracer velocities was confirmed within the error of 50% for all tracers. Furthermore, the tracer velocity appeared to be completely independent of the timing of the flash X-ray irradiation, indicating that all tracers moved at almost constant velocities. The six tracers located at the outer region of the target (#1, #3, #6, #7, #10, #12) showed velocities higher than that of the six tracers located at the inner region of the target (#2, #4, #5, #8, #9, #11) at the same distance. This indicates that the tracer velocity depended not only on the distance from the impact point but also the distance from the target surface. Thus we clearly showed that both the shock pressure attenuation and the reflection wave from the target surface controlled the tracer velocity.

Fig. 16

4.5 Cumulative mass–velocity distribution

4.5.1 Estimation of the mass around iron tracers

In order to obtain the velocity distribution of impact fragments, we assume that the impact fragments had the same velocity as that of the nearest iron tracer observed by the flash X-ray radiography. The initial positions of the iron tracers were determined by X-ray images and were plotted on the sectioned tracer plane (Fig. 17). Figure 17 shows an example of the division of the areas having the same velocity as the nearest iron tracer, so that there are twelve area corresponding to iron tracers. In deriving mass-velocity distribution for the whole target with the velocity of iron tracers it is assumed that the distributions of ejecta velocity vectors at the left and the right side of the impact axis are axial symmetrical to the impact axis and its out-of-plane component is negligible or zero, based on the observation described in section 4.4. As schematically shown in Fig 17, two-dimensional mesh in polar coordinates (r, θ) are created in cross section of the target sphere containing iron tracers in this plane. Then the volume of shell is numerical calculated by revolving the meshed element 180° around the impact axis, and for the velocity we assumed it identical to its nearest iron tracer for this study. In our calculation mesh is gridded 0.01 mm radially and in 0.1° . The mass of each meshed element was estimated by the product of the target density and the calculated volume, so we can determine the relationship between the mass of the element and the ejection velocity that was represented by the iron tracer nearest the element.

Fig. 17

4.5.2 Median velocity

By using the relationship between the mass and the ejection velocity of each element

649 in each impact experiment, we can reconstruct the mass–velocity distribution on the
 650 catastrophic disruption. In this study, the mass of the element with an ejection velocity
 651 lower than a specific velocity was examined, and this cumulative mass related to the
 652 velocity was studied to determine its mass–velocity distribution. Figure 18 (a–c) shows
 653 the relationship between the ejection velocity in the center-of-mass system, v_{cms} , and the
 654 mass normalized by the original target mass with a velocity lower than v_{cms} for frozen
 655 clay targets. Figure 18 (a–c) summarizes the mass–velocity distributions at a constant
 656 Q of 3×10^3 , 5×10^3 and 1×10^4 Jkg^{-1} , respectively. The normalized cumulative mass
 657 linearly increases with the increase of v_{cms} at velocities lower than ~ 10 ms^{-1} for $Q =$
 658 $2 \sim 3 \times 10^3$ Jkg^{-1} , ~ 20 ms^{-1} for $Q = 5 \sim 6 \times 10^3$ Jkg^{-1} , and ~ 30 ms^{-1} for $Q = 9 \sim 11 \times 10^3$ Jkg^{-1} , and
 659 then the slope of the distribution declines abruptly at the normalized cumulative mass of
 660 ~ 0.8 in all figures. The difference in the distribution depending on the water content of
 661 the target cannot be recognized in all figures, although the Q_s^* shattering strength of FC45
 662 was clearly different from those of FC25 and FC35. Thus, the reproducibility of the
 663 distribution at each Q looks quite good, irrespective of the target water content. In order
 664 to characterize the mass–velocity distribution, we determined the v_{cms} at the normalized
 665 cumulative mass of 0.5 for each distribution and named it the median velocity, which is
 666 written by v^* : The half of the original target mass has an ejection velocity of v_{cms} that is
 667 lower than v^* , so that the median velocity would be one of the best parameters to describe
 668 the velocity distribution of impact fragments caused by the catastrophic disruption. Then,
 669 the difference of the velocity distributions among Fig. 18a, b, and c can be characterized
 670 by the v^* for the distributions in each figure, which increased from ~ 8 ms^{-1} to ~ 22 ms^{-1}

Fig. 18

671 with the increase of Q from $\sim 3 \times 10^3 \text{ Jkg}^{-1}$ to $\sim 1 \times 10^4 \text{ Jkg}^{-1}$.

672 The velocity distributions characterized by the normalized cumulative mass and the
 673 v_{cms} for porous gypsum targets are shown in Fig. 19, where each symbol represents the
 674 specific energy Q directed at one of the targets. Just as observed for the frozen clay targets,
 675 the distributions obtained in the same Q were well merged to have almost the same v^* and
 676 the normalized cumulative mass linearly increased by 0.8, but these slopes were rather
 677 steeper than those of the frozen clay targets at the same Q . The v^* for the porous gypsum
 678 targets was roughly estimated to increase from $\sim 3 \text{ ms}^{-1}$ to $\sim 15 \text{ ms}^{-1}$ with the increase from
 679 $Q = \sim 4 \times 10^3 \text{ Jkg}^{-1}$ to $\sim 2.5 \times 10^4 \text{ Jkg}^{-1}$. These v^* values were remarkably lower than those of
 680 the frozen clay targets at the same Q , although the shattering strength Q_s^* of the porous
 681 gypsum was almost the same as those of FC35 and FC45.

Fig. 19

682 The v^* values of the frozen clay targets against the specific energy Q are compared to
 683 those of the porous gypsum targets in Fig. 20. It is clear that the values of v^* are very well
 684 correlated to those of Q for each data set, and that FC25, FC35, and FC45 were very
 685 closely related to each other. This means that they could be independent of the target
 686 tensile strength and Q_s^* caused by the water content. However, the v^* of the porous
 687 gypsum targets was systematically lower than those of the frozen clay targets: It was half
 688 that of the frozen clay targets. Since the Q_s^* of the porous gypsum was similar to that of
 689 FC25, the Q_s^* might not be the cause of the systematic change of the median velocity, v^* .
 690 The porosity of the gypsum targets, 51%, was clearly larger than that of the frozen clay
 691 targets, $< 5\%$. The previous numerical simulations suggested that the target porosity could
 692 effectively increase the Q_D^* , but the tensile strength could not have a very large effect on

Fig. 20

the Q_D^* , and thus our results of the low v^* for porous gypsum targets and the similar v^* for the frozen clay targets with different tensile strengths are well consistent with the previous numerical results (Jutzi, 2015). The empirical relationship between v^* and Q is described by the following equation:

$$v^* = \varepsilon Q^\gamma, \quad (6)$$

where ε and γ are constants and are shown in Table 2 for each target.

4.6 Comparison with numerical simulations

4.6.1 Frozen clay targets

Next, the results from the laboratory experiments described in the previous sections were compared to the results of numerical simulations that used the same initial conditions. The simulations were carried out to 4 μ s. The mass distributions were compared in two cases with different strength, i.e., targets FC25 and FC45. The largest remnants were relatively well reproduced in the simulations in both cases (Fig. 21). However, the masses of the smaller fragments were slightly underestimated. As discussed above, the fragmentation behavior of the frozen clay may involve more complex processes than in the case of a monolithic rock, and the targets may be partly ductile rather than brittle. In the modelling, the partly ductile behavior was accounted for by using a very low internal coefficient of friction, which leads to enhanced plastic deformation before tensile fragmentation.

Additional runs with lower specific energy were performed to compute the shattering strength (Table 3). We obtained shattering strengths of $Q_S^* = 476$ J/kg (FC45) and $Q_S^* =$

Fig. 21

Table 3

1550 J/kg (FC25), respectively. These values are somewhat larger than those found in the impact experiments in the laboratory, which were $Q_S^* = 198_{-62}^{+61}$ J/kg for FC45 and $Q_S^* = 705_{-521}^{+563}$ J/kg for FC25. However, we note that the numerical simulations performed in this study were focused on the high impact energy disruption regime ($Q_D^* \gg Q_S^*$), and the slight overestimation of Q_S^* by the simulation did not affect the results for Q_D^* .

Figure 22 compares the mass–velocity distributions for three different specific energies. The overall agreement between the simulations and the experimental results is very good. The simulations also show a very small dependence of the mass–velocity distribution on the cohesion (FC25 vs. FC45), which is one of the key results from the experiments.

Fig. 22

4.6.2 Gypsum targets

In Fig. 23, the mass frequency distributions obtained in the numerical simulations using porous gypsum targets are compared to the experimental results. In the numerical calculations, we performed 3 runs for each of the 3 different specific energy regimes considered in the experiments. There was good agreement between the low and moderately high specific energies. In the case of the very high (2.5×10^4 J/kg) specific energy regime, the simulations underestimated the masses of the largest fragments.

Fig. 23

For the same 3 sets of 3 specific energy regimes, Fig. 24 shows a comparison of the mass–velocity distributions. As observed for the mass frequency distributions, there is some deviation between simulations in the very high specific energy regime (the simulations slightly underestimate the fragment velocities). Among the other specific

Fig. 24

energies, there is very good agreement. The simulations thus well reproduced the key finding of the experiments: the v^* of the porous targets was systematically lower than the v^* of the frozen clay targets.

5. Discussion

5.1 Impact strength in the gravity-dominated regime

The shattering strength, Q_S^* , which is the impact strength in the strength-dominated regime, is usually determined by using the relationship between m_l/M_t and Q as shown in Fig. 9a: The Q_S^* is defined as the Q at $m_l/M_t=0.5$. The dispersion strength, Q_D^* , which is the impact strength in the gravity-dominated regime, is determined by the same relationship between m_l/M_t and Q , except that the m_l of the largest fragment mass is usually a result of the gravitational re-accretion process of impact fragments. Therefore, numerical simulations including the gravitational attraction force are usually used to study the largest remnant mass m_l resulting from a catastrophic disruption in the gravity-dominated regime. In this study, we use a different approach and consider that m_l can be estimated by comparing the ejection velocities of the impact fragments with the escape velocity of the original target body, v_{esc} , before the disruption. To compute m_l , we assume that the fragments with the ejection velocities lower than v_{esc} are reaccumulated to form the largest remnant with a mass m_l . According to this simple assumption, Q_D^* can be estimated by the condition $v^* \leq v_{\text{esc}}$, because a mass equivalent to more than half of the original target body mass will have an ejection velocity lower than the escape velocity of

the original target body. At $v^*=v_{\text{esc}}$, m_i/M_t should be equal to 0.5. Assuming a homogeneous body with a density of ρ and a radius of R , the escape velocity can be written as $v_{\text{esc}} = \left(\frac{8}{3}G\pi\rho\right)^{1/2} R$. Then, Eq. (6) is equated to v_{esc} and Q_D^* is obtained as

$$Q_D^* = \left[\left(\frac{8}{3}G\pi\rho\right)^{1/2} \frac{R}{\varepsilon} \right]^{1/\gamma}, \quad (7)$$

where G is the gravitational constant. As a result, Q_D^* can be calculated for homogeneous target bodies with various radii, R , when the relationships between v^* and Q are obtained for various target bodies in laboratory experiments. Using this approach, we calculate the Q_D^* for the target bodies simulated by the frozen clay and the porous gypsum targets. Figure 25 shows the size dependence of Q_D^* for the frozen clay target body and the porous gypsum body, where the values of ε , γ , ρ are as shown in Table 2. It is clear both that Q_D^* increases with the increase of the radius with the power law index of 1.4 to 1.6, and that in the gravity-dominated regime, the porous gypsum targets are 2 to 3 times stronger than the frozen clay targets.

Fig. 25

5.2 Comparison with numerical simulations

Using the results of the numerical simulations (i.e., the mass–velocity distributions of the SPH particles), the catastrophic disruption threshold Q_D^* as a function of the scale R can be computed in a number of different ways. Here we compare the various approaches. In the following, R and M_{target} are the radius and the mass of the target body, respectively, and M is the mass of the disrupted target body which is effectively used to compute v_{esc} .

The FC45 simulations are used in this analysis.

- 1) Computation of v^* based on the mass–velocity distributions obtained in the SPH simulations of the *laboratory* scale impacts. Using $v^* = v_{\text{esc}}$ (the same approach as used for the experimental results in section 5.1) yields $Q_D^* = f(R)$. Here, v_{esc} is computed using $M = M_{\text{target}}$.
- 2) Identical to method (1) above, but v_{esc} is computed using $M = M_{\text{target}}/2$.
- 3) Computation of Q_D^* based on the *laboratory* scale simulations using an energy iteration method (comparing kinetic and potential energies of SPH particles; see e.g. Jutzi *et al.*, 2010). To compute Q_D^* for a given target size R , we use a scaled gravitational constant $G_{\text{scaled}} = G (R/R_{\text{lab}})^2$.
- 4) Computation of Q_D^* based on *large-scale* simulations using targets of size R , and using the same projectile to target the mass ratio M_p/M_t as in the laboratory scale impacts and a constant, laboratory-scale tensile strength. The energy iteration method is applied.

As can be seen in Fig. 26, methods (3) and (4) lead to identical outcomes. This means that the results of the simulations (in terms of Q_D^*) are self-similar and do not depend on the scale. We note that the same tensile strength was used for both the large-scale simulations and laboratory scale impacts. The use of a size-dependent tensile strength (such as that based on the Weibull model; see e.g. Jutzi and Michel, 2014) may lead to a slightly lower Q_D^* at large scales. The question of the scale-dependence of the tensile strength will be addressed in a future study.

The approach based on using $v^* = v_{\text{esc}}$ (applied on the laboratory scale simulation outcomes) leads to an overestimation of Q_D^* compared to methods (3) and (4), if $M =$

Fig. 26

M_{target} is used to compute the escape velocity (method (1)). However, good agreement is found between methods (3) and (4) when using $M = M_{\text{target}}/2$. Method (2) is therefore suitable for predicting Q_D^* in the gravity regime, using data from laboratory scale impacts.

As discussed in section 4.5.2, v^* can be scaled using $v^* = \varepsilon Q^\gamma$. We determine the parameters ε and γ by fitting the results of our lab-scale simulations using frozen clay targets (Fig. 27). We then use the approach $v^* = \varepsilon Q^\gamma = v_{\text{esc}}$ to compute $Q_D^* = f(R)$ and compare the scaling with the large-scale simulations (Fig. 28). There is a good agreement of the scaling with the simulations at large ($\gtrsim 10$ km) scales, if v_{esc} is computed using $M = M_{\text{target}}/2$ (method (2)). However, there is some deviation at lower scales. As discussed above, the Q_D^* curves as a function of scale start to deviate from a single power-law at smaller $\lesssim 10$ km scales (Fig. 28). This may be due to the increased effect of tensile strength at smaller scales (i.e., smaller specific impact energies leading to larger intact fragments). The transition from the gravity regime to the strength regime will be explored in a subsequent study.

Fig. 27

Fig. 28

5.3 Scaling law for the impact strength in the gravity-dominated regime

In this study, the relation $v^* = \varepsilon Q^\gamma$ was compared to experiments using a constant impactor/target mass ratio m_r . A more general relation would also include the variation of m_r , such as for example $v^* = \frac{\varepsilon}{2} m_r^\kappa v^{2\gamma}$. We note that this relation translates into $Q_D^* \sim R^{1/\kappa} v^{2-2\gamma/\kappa}$, which corresponds to $Q_D^* \sim R^{3\mu} v^{2-3\mu}$ (Housen and Holsapple, 1990) if $\gamma = 0.5$ and $\kappa = 1/3\mu$, where v is the collisional velocity and μ is a constant of the coupling parameter in the π scaling theory. Interestingly, both the experimental results

and the numerical simulations indicate that $\gamma \sim 0.7$ (Fig. 28), which suggests that Housen and Holsapple (1990) scaling $Q_D^* \sim R^{3\mu} v^{2-3\mu}$ does not fully capture the collisional outcomes in this regime. This issue will be addressed in a subsequent study that also includes experiments performed at different mass ratios m_r in order to explore the dependence on this parameter.

6. Conclusions

We numerically and experimentally studied the shattering and dispersion strengths of the target bodies simulating rocky and frozen planetesimals. The shattering strengths of these targets were experimentally determined to be 705 J kg^{-1} for FC25 and FC35, 198 J kg^{-1} for FC45 and 760 J kg^{-1} for porous gypsum. The difference of Q_D^* among the frozen clay targets may have been caused by the tensile strength, since the tensile strength of FC25 was twice as large as that of FC45. On the other hand, the median velocities of the frozen clays were almost the same in the three types of targets, irrespective of the shattering strength, but the median velocity of the porous gypsum was $1/3$ of those of the frozen clays, although the porous gypsum had a shattering strength similar to those of FC25 and FC35. Therefore, we speculate that the median velocity is independent of the tensile strength for non-porous targets composed of similar materials, and strongly dependent on the porosity for the targets with similar shattering strength. These dependencies of Q_S^* and v^* on various targets with different tensile strength and porosity were well reproduced by the numerical simulations.

The numerical model which succeeded at reproducing the laboratory outcomes for

the frozen clays was applied to large-scale simulations including the self-gravity, and the dispersion strength of target bodies was studied in a similar manner as for the frozen clays. For the laboratory impacts, the dispersion strength could be approximated by equating v^* with the escape velocity v_{esc} of target bodies, assuming that all the mass with a velocity lower than v_{esc} reaccumulates on the largest fragment body due to the gravity. Based on this assumption, a semi-theoretical equation was found for the dispersion strength $Q_D^* = \left[\frac{1}{\varepsilon} \left(\frac{2GM}{R} \right)^{1/2} \right]^{1/\gamma}$, where M and R are the effective target body with the gravity attracting a half of the original target mass. The large-scale simulations confirmed that this semi-theoretical equation for Q_D^* is well consistent with the large-scale numerical results when M was a half of the original target mass. Furthermore, it was found that this simple equation of Q_D^* is only valid at a scale larger than ~ 10 km, because at a scale smaller than ~ 10 km, not only the gravity but also the largest cohesive remnant would affect the impact strength.

Acknowledgments

We appreciate helpful comments of Dr. Guy Libourel to improve our manuscript. We wish to thank R. Suetsugu of Oshima College for useful comments on the numerical simulation, and K. Ogawa of JAXA and K. Shirai of Kobe University for help analyzing the X-ray images. We also thank T. Nagano for help conducting the impact experiments at JAXA. This series of experiments was supported in part by the Hypervelocity Impact

865 Facility at ISAS/JAXA, and by Grants-in-Aid for Scientific Research (nos. 17H06459
 866 and 19H00719) from the Japan Ministry of Education, Culture, Sports, Science and
 867 Technology.

868

869 **References**

870 Arakawa, M., 1999. Collisional disruption of ice by high-velocity impact. *Icarus* 142, 34–
 871 45.

872 Benz, W., Asphaug, E., 1999. Catastrophic disruptions revisited. *Icarus* 142, 5–20.

873 Benz, W., Asphaug, E., 1995. Simulations of brittle solids using smooth particle
 874 hydrodynamics. *Comput. Phys. Commun.* 87, 253–265.

875 Benz, W., Asphaug, E., 1994. Impact simulations with fracture. I-method and tests. *Icarus*
 876 107, 98–116.

877 Bottke Jr, W.F., Durda, D.D., Nesvorný, D., Jedicke, R., Morbidelli, A., Vokrouhlický, D.,
 878 Levison, H., 2005. The fossilized size distribution of the main asteroid belt. *Icarus* 175,
 879 111–140.

880 Bottke Jr, W.F., Nolan, M.C., Greenberg, R., Kolvoord, R.A., 1994. Velocity distributions
 881 among colliding asteroids. *Icarus* 107, 255–255.

882 Collins, G.S., Housen, K.R., Jutzi, M., Nakamura, A.M., 2019. Planetary impact
 883 processes in porous materials. In: Vogler T., Fredenburg D. (eds) *Shock Phenomena in*
 884 *Granular and Porous Materials. Shock Wave and High Pressure Phenomena*. Springer,

- 885 Cham. https://doi.org/10.1007/978-3-030-23002-9_4.
- 886 Fujiwara, A., & Tsukamoto, A., 1980. Experimental study on the velocity of fragments
887 in collisional breakup. *Icarus*, 44, 142-153.
- 888 Fujiwara, A., Kamimoto, G., Tsukamoto, A., 1977. Destruction of basaltic bodies by high
889 -velocity impact. *Icarus* 31, 277–288.
- 890 Fujiwara, A., Kawaguchi, J., Yeomans, D.K., Abe, M., et al., 2006. The rubble-pile
891 asteroid Itokawa as observed by Hayabusa. *Science* 312, 1330–1334.
- 892 Giblyn, I., Martelli, G., Farinella, P., Paolicchi, P., et al., 1998. The properties of fragments
893 from catastrophic disruption events. *Icarus* 134, 77–112.
- 894 Holsapple, K., Giblyn, I., Housen, K., Nakamura, A., Ryan, E., 2002. Asteroid impacts:
895 Laboratory experiments and scaling laws. Paolicchi, R.P. Binzel (Eds.), *Asteroids III*,
896 Univ. of Arizona Press, Tucson (2002), pp. 443–462.
- 897 Housen, K.R., Holsapple, K.A., 1999. Scale effects in strength-dominated collisions of
898 rocky asteroids. *Icarus* 142, 21–33.
- 899 Housen, K.R., Holsapple, K.A., 1990. On the fragmentation of asteroids and planetary
900 satellites. *Icarus* 84, 226–253.
- 901 Jutzi, M., 2015. SPH calculations of asteroid disruptions: The role of pressure dependent
902 failure models. *Planetary and Space Science* 107, 3–9.
- 903 Jutzi, M., Benz, W., Michel, P., 2008. Numerical simulations of impacts involving porous
904 bodies. I. Implementing sub-resolution porosity in a 3D SPH hydrocode. *Icarus* 198,
905 242–255.
- 906 Jutzi, M., Michel, P., Hiraoka, K., Nakamura, A.M., Benz, W., 2009. Numerical

- 907 simulations of impacts involving porous bodies. II. comparison with laboratory
 908 experiments. *Icarus* 201, 802–813.
- 909 Kawakami, S. I., Mizutani, H., Takagi, Y., Kato, M., Kumazawa, M., 1983. Impact experiments
 910 on ice. *J. Geophys. Res.*, 88, 5806-5814.
- 911 Kobayashi, H., Tanaka, H., Krivov, A.V., 2011. Planetary core formation with collisional
 912 fragmentation and atmosphere to form gas giant planets. *The Astrophysical Journal*
 913 738, 35.
- 914 Kobayashi, H., Tanaka, H., Krivov, A.V., Inaba, S., 2010. Planetary growth with
 915 collisional fragmentation and gas drag. *Icarus* 209, 836–847.
- 916 Leinhardt, Z. M., Stewart, S. T., 2011. Collisions between gravity-dominated bodies. I. Outcome
 917 regimes and scaling laws. *The Astrophysical Journal*, 745, 79.
- 918 Mizusako, F., Ogasawara, K., Kondo, K., Saito, F., Tamura, H., 2005. Flash x-ray
 919 radiography using imaging plates for the observation of hypervelocity objects. *Review*
 920 *of Scientific Instruments* 76, 025102.
- 921 Mizutani, H., Takagi, Y., Kawakami, S.I., 1990. New scaling laws on impact
 922 fragmentation. *Icarus* 87, 307–326.
- 923 Nakamura, A., Fujiwara, A., 1991. Velocity distribution of fragments formed in a
 924 simulated collisional disruption. *Icarus* 92, 132–146.
- 925 Nakamura, A.M., Michel, P., Setoh, M., 2007. Weibull parameters of Yakuno basalt
 926 targets used in documented high- velocity impact experiments. *J. Geophys. Res.* 112,
 927 E02001.
- 928 Nyffeler, B., 2004. Modelling of Impacts in the Solar System on a Beowulf Cluster.

- 929 University of Bern PhD thesis.
- 930 Schulson, E.M., Duval, P., 2009. Creep and fracture of ice. Cambridge University Press,
 931 New York, pp. 416.
- 932 Takagi, Y., Mizutani, H., Kawakami, S. I. ,1984. Impact fragmentation experiments of
 933 basalts and pyrophyllites. *Icarus*, 59, 462-477.
- 934 Watanabe, S., Hirabayashi, M., Hirata, N., Hirata, N., et al., 2019. Hayabusa2 arrives at
 935 the carbonaceous asteroid 162173 Ryugu - A spinning top-shaped rubble pile. *Science*
 936 364, 268–272.
- 937 Yasui, M., Arakawa, M., 2011. Impact experiments of porous gypsum–glass bead
 938 mixtures simulating parent bodies of ordinary chondrites: Implications for re-
 939 accumulation processes related to rubble-pile formation. *Icarus* 214, 754–765.
- 940 Yasui, M., Arakawa, M., Hasegawa, S., Fujita, Y., Kadono, T., 2012. In situ flash X-ray
 941 observation of projectile penetration processes and crater cavity growth in porous
 942 gypsum target analogous to low-density asteroids. *Icarus* 221, 646–657.
- 943 Yasui, M., Arakawa, M., Yoshida, Y., Matsue, K., Takano, S., 2020. Effects of oblique
 944 impacts on the impact strength of porous gypsum and glass spheres: Implications for
 945 the collisional disruption of planetesimals in thermal evolution. *Icarus* 335, 113414.
- 946 Yasui, M., Hayama, R., Arakawa, M., 2014. Impact strength of small icy bodies that
 947 experienced multiple collisions. *Icarus* 233, 293–305.

Figure captions

Fig. 1: (a) Photo of iron tracer particles set on a tracer plane of the frozen clay target before freezing. (b) Illustration showing the positions of twelve iron tracer particles and the aiming point for the launched projectile.

Fig.2: Photos of the frozen clay target FC45 (a) and porous gypsum target (b).

Fig. 3: Experimental set up for the X-ray radiography. A side view of the target hanging from the metal platform by strings is shown by (a) an illustration and (b) a photo. The projectile impacted from the right side. A front view of the target and the installed three flash X-rays and IPs is shown by (c) an illustration and (d) a photo taken from the side of the launching tube of the gun.

Fig. 4: Photo of fragments recovered in the impact experiment for FC45, Run no. 170922-2. The largest fragment is enclosed by a dashed line.

Fig. 5: X-ray images recorded on the three imaging plates (IP1, 2, 3) before the shot. (a) IP1, (b) IP 3, and (c) IP2. The large grey circle is the target, and the twelve small black circles appearing inside the circle are the iron tracers.

Fig. 6: (a) Laboratory coordinate system of a target. A Cartesian system is adopted

with the origin set at the center of the target. The impact direction is along the y -axis, and the z -axis is along the direction of gravity and directed upward. (b) Schematic illustration of the x - z coordinate system and the directions of the flash X-ray irradiations together with the planes in which the image plates were set.

Fig. 7: An X-ray image of Run no. 170224-1 for FC35 recorded on IP1 at 750 μ s after the impact. The original target shape is drawn by a large circle. The initial positions of iron tracers are shown by small black circles, and the displacement vectors between these initial positions and the tracer positions after the impact are shown by arrows.

Fig. 8: Definition of the impact point in the experimental coordinate system. (a) A snapshot of the impact disruption taken by the high-speed camera (Run no. 170725-4). The image is a side view of the target, and the white circle on the image is an original target shape. The definition of θ , which represents the angle deviation from the normal impact, is explained in the main text. (b) A flash X-ray image of IP3 (Run no. 170224-2), top view. The method used to determine the impact point is explained in the main text. The tracer positions before the shot are indicated with black circles, and those after the shot are shown with white circles. (c) A flash X-ray image of IP3 (Run no. 170224-1), top view. The definition of δ , which represents the angle of deviation from the normal impact, is explained in the main text.

Fig. 9: Relationship between the largest fragment mass normalized by the original target mass and the specific energy. (a) Three frozen clay targets. L.T. and R.T. indicate the targeted low temperature (-15°C) and room temperature, respectively. The solid line labeled FC25 is a fitted line for the data of FC25 and FC35, and the dotted line labeled FC45 is a fitted line for FC45. Three reference lines representing porous gypsum (Yasui et al., 2020), basalt (Fujiwara and Tsukamoto, 1980), and water ice (Arakawa, 1999) are shown on the same figure. (b) A porous gypsum target. The solid and dotted lines are the fitted line for this study and that obtained in Yasui et al. (2020), respectively.

Fig. 10: Mass frequency distributions described by the relationship between the cumulative number of fragments and the fragment mass normalized by the original target mass. (a) FC45. (b) FC25 and FC35. (c) Porous gypsum.

Fig. 11: Photos of the recovered impact fragments. (a) FC25 at $2.76 \times 10^3 \text{ J kg}^{-1}$ (Run no. 171110-1). (b) Porous gypsum at 9.99×10^3 (Run no. 180328-3).

Fig. 12: Relationship between the antipodal velocity and the specific energy. (a) Three frozen clay targets. L.T. and R.T. indicate the targeted low temperature (-15°C) and room temperature, respectively. The solid line labeled FC25 & 35 is a fitted line for the data of FC25 and FC35, and the dashed-dotted line labeled by FC45 is a fitted line for FC45. Three reference lines representing porous gypsum (Yasui et al., 2020),

basalt (Fujiwara and Tsukamoto, 1980)) and water ice (Arakawa, 1999) are shown on the same figure. (b) A porous gypsum target. The dotted line is the fitted line in Yasui *et al.* (2020).

Fig. 13: Flash X-ray images recorded on IP1 (right panels), IP2 (middle panels), and IP3 (left panels) for FC45. (a) Run no. 170609-2, $1.41 \times 10^3 \text{ Jkg}^{-1}$. The flash X-ray was irradiated at 100 μs (left panel), 500 μs (middle panel) and 1 ms (right panel). (b) Run no. 170727-1, $3.00 \times 10^3 \text{ Jkg}^{-1}$. The flash X-ray was irradiated at 250 μs (left panel), 750 μs (middle panel) and 1.5 ms (right panel). (c) Run no. 171025-4, $9.55 \times 10^3 \text{ Jkg}^{-1}$. The flash X-ray was irradiated at 50 μs (left panel), 750 μs (middle panel) and 750 μs (right panel). The velocity vectors of iron tracers in the center-of-mass system were measured on the x - y plane (left panels) and the y - z plane (right panels) for (d) Run no. 170609-2, (e) Run no. 170727-1, and (f) Run no. 171025-4. The color scale bar shows the speed of the iron tracers. The images in (d), (e) and (f) were obtained from those in (a), (b), and (c), respectively.

Fig. 14: Flash X-ray images recorded on IP1 (right panel), IP2 (middle panel), and IP3 (left panels). (a) FC45. Run no. 170726-1, $5.00 \times 10^3 \text{ Jkg}^{-1}$. The flash X-ray was irradiated at 100 μs (left panel), 500 μs (middle panel) and 1 ms (right panel). (b) FC25. Run no. 170608-3, $5.57 \times 10^3 \text{ Jkg}^{-1}$. The flash X-ray was irradiated at 50 μs (left panel), 250 μs (middle panel) and 750 μs (right panel). The velocity vectors of iron tracers in the center-of-mass system were measured on the x - y plane (left panels)

and the y - z plane (right panels) for (c) Run no. 170726-1 and (d) Run no. 170608-3. The color scale bar shows the speed of the iron tracers. The images in (c) and (d) were obtained from those in (a) and (b), respectively.

Fig. 15: Flash X-ray images recorded on IP1 (right panel), IP2 (middle panel), and IP3 (left panels). (a) FC45. Run no. 171025-4, $9.55 \times 10^3 \text{ J kg}^{-1}$. The flash X-ray was irradiated at 50 μs (left panel), 750 μs (middle panel) and 750 μs (right panel). (b) Porous gypsum. Run no. 180328-1, $9.81 \times 10^3 \text{ J kg}^{-1}$. The flash X-ray was irradiated at 50 μs (left panel), 500 μs (middle panel) and 500 μs (right panel). The velocity vectors of iron tracers in the center-of-mass system were measured on the x - y plane (left panels) and the y - z plane (right panels) for (c) Run no. 171025-4 and (d) Run no. 180328-1. The color scale bar shows the speed of the iron tracers. The images in (c) and (d) were obtained from those in (a) and (b), respectively.

Fig. 16: Relationship between the tracer velocity in the center-of-mass system and the distance from the impact point for Runs no. 171025-3, 171025-4, and 171025-5. The velocities of the tracer with the same number and with almost the same distance are enclosed by dashed circles. The position of each tracer is illustrated in the small figure at the right side.

Fig. 17: Division of the areas having the same velocity as the nearest iron tracer. A meshed element with the size of dr and $d\theta$ is shown in this schematic illustration of

the tracer plane. For the actual calculation, the mesh is gridded 0.01 mm radially and in 0.01° . Each meshed element is enclosed by a thin grey line, and twelve iron tracers shown by black circles are enclosed by thick grey lines and colored differently. The impact axis and the impact point are shown by a dashed line and a cross symbol.

Fig. 18: Mass-ejection velocity distribution of the frozen clay targets (FC25, FC35, FC45) shown by the relationship between the normalized cumulative mass and ejection velocity in the center-of-mass system. (a) $Q=2\sim3\times10^3 \text{ J kg}^{-1}$, (b) $Q=5\sim6\times10^3 \text{ J kg}^{-1}$, and (c) $Q=9\sim11\times10^3 \text{ J kg}^{-1}$. The normalized cumulative mass equal to 0.5 is shown by a dashed line.

Fig. 19: Mass-ejection velocity distribution of the porous gypsum targets shown by the relationship between normalized cumulative mass and ejection velocity in the center-of-mass system.

Fig. 20: Relationship between the median velocity, v^* , and the specific energy, Q , for different targets.

Fig. 21:

Comparison of the fragment mass distributions (frozen clay targets). Two cases are shown: one using the FC25 target (Run no. 171110-3) and one using the FC45 (Run no. 170913-1).

Fig. 22:

Comparison of velocity distributions (frozen clay targets). Run no. 171025-4 for FC45 and $Q=9.5 \times 10^3 \text{ J kg}^{-1}$, Run no. 170608-4 for FC45 and $Q=5.4 \times 10^3 \text{ J kg}^{-1}$, Run no. 170727-3 for FC45 and $Q=1.3 \times 10^3 \text{ J kg}^{-1}$, Run no. 170608-3 for FC25 and $Q=5.6 \times 10^3 \text{ J kg}^{-1}$.

Fig. 23:

Comparison of the fragment mass distributions (porous gypsum targets). The results for 3 different energy regimes are shown (see Table 3 for the experimental conditions): Blue: $\sim 4 \times 10^3 \text{ J/kg}$; Green: $\sim 9 \times 10^3 \text{ J kg}^{-1}$; Red: $\sim 2.5 \times 10^4 \text{ J kg}^{-1}$.

Fig. 24:

Comparison of velocity distributions (porous gypsum targets). The results for 3 different energy regimes are shown (see Table 1 for the experimental conditions): Blue: $\sim 4 \times 10^3 \text{ J/kg}$; Green: $\sim 9 \times 10^3 \text{ J kg}^{-1}$; Red: $\sim 2.5 \times 10^4 \text{ J kg}^{-1}$.

Fig. 25: Dispersion strength depending on the radius of target bodies estimated by the semi-theoretical Eqs. (6) and (7) with the parameters shown in Table 2.

Fig. 26:

Comparison of methods for the Q_D^* calculations.

1102

1103 **Fig. 27:**

1104 v^* as a function of specific energy. Also shown is the relation $v^* = \varepsilon Q^\gamma$ with $\varepsilon =$
1105 3.8×10^{-2} and $\gamma=0.72$.

1106

1107 **Fig. 28:**

1108 Comparison of large-scale simulation results and scaling.



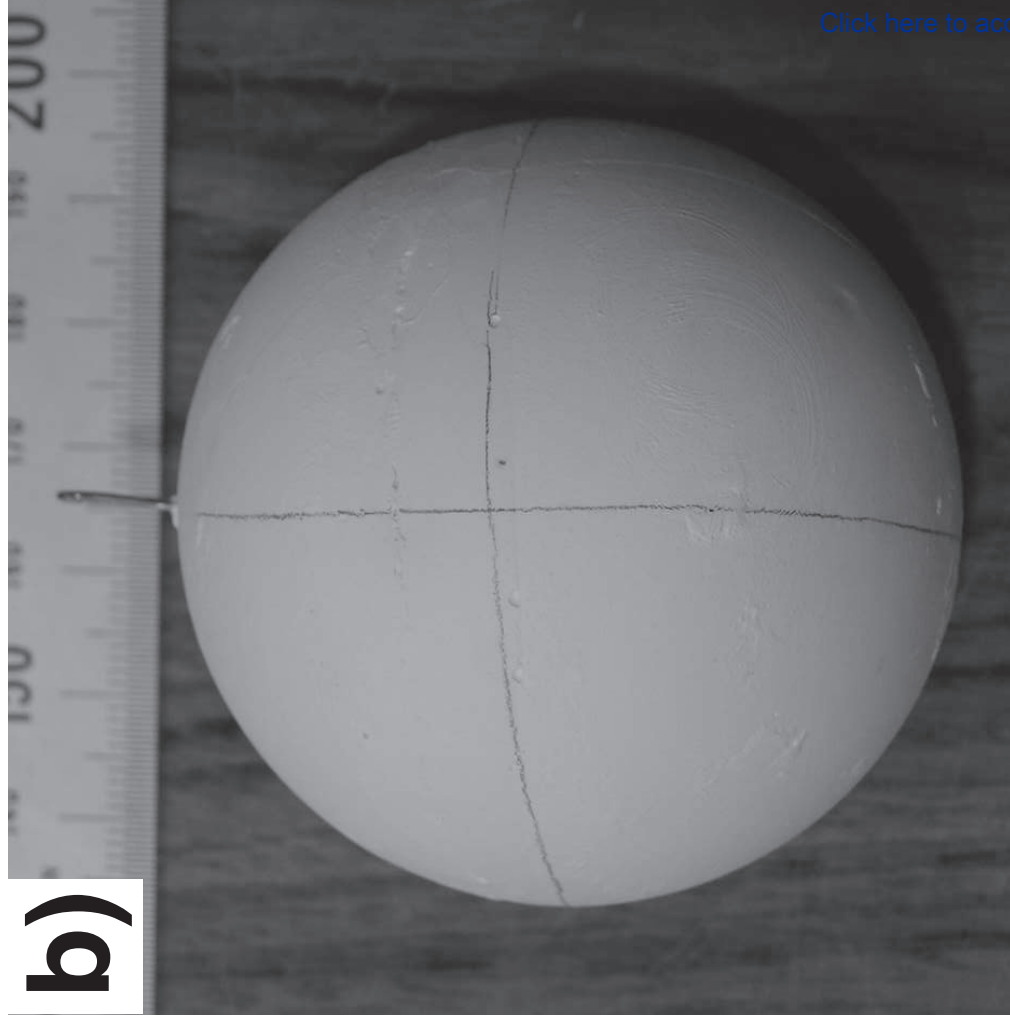
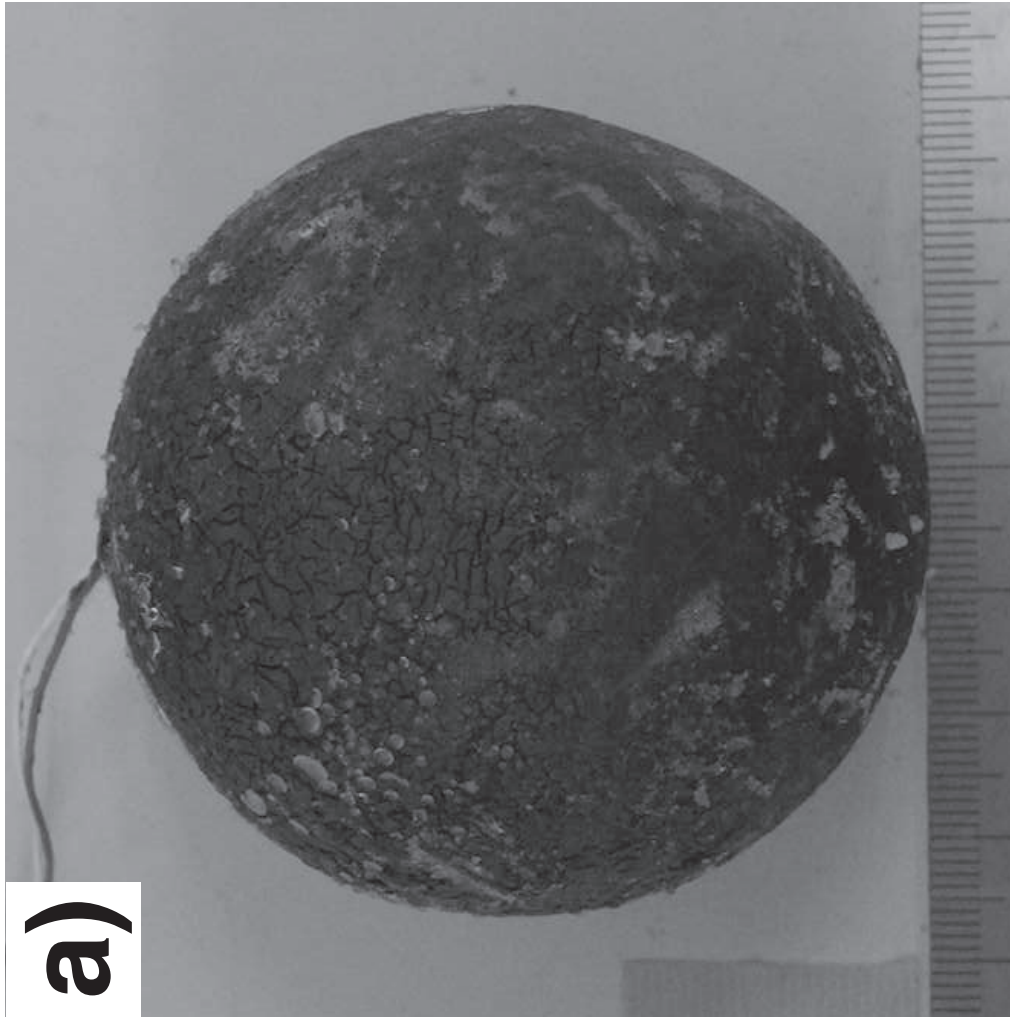


Figure3

[Click here to access/download;Figure;fig3.eps](#)

a)

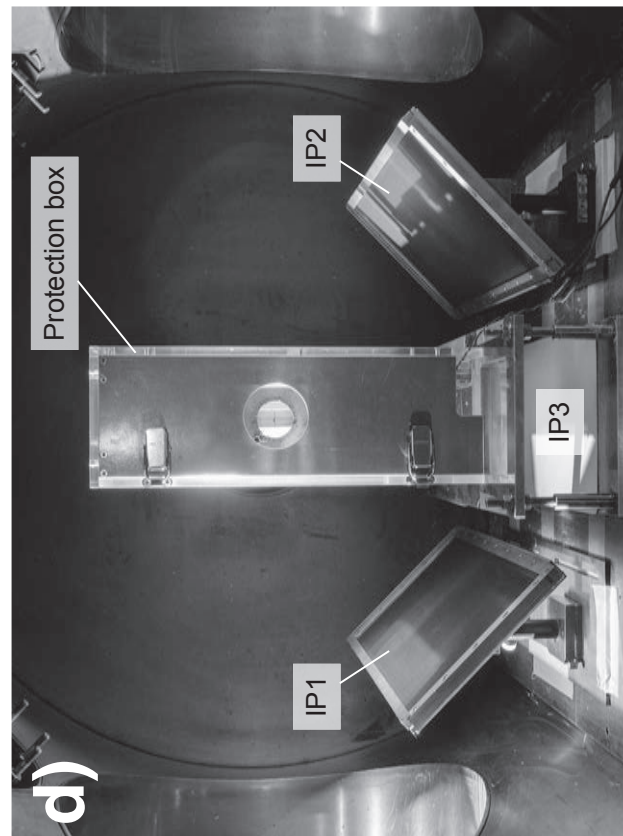
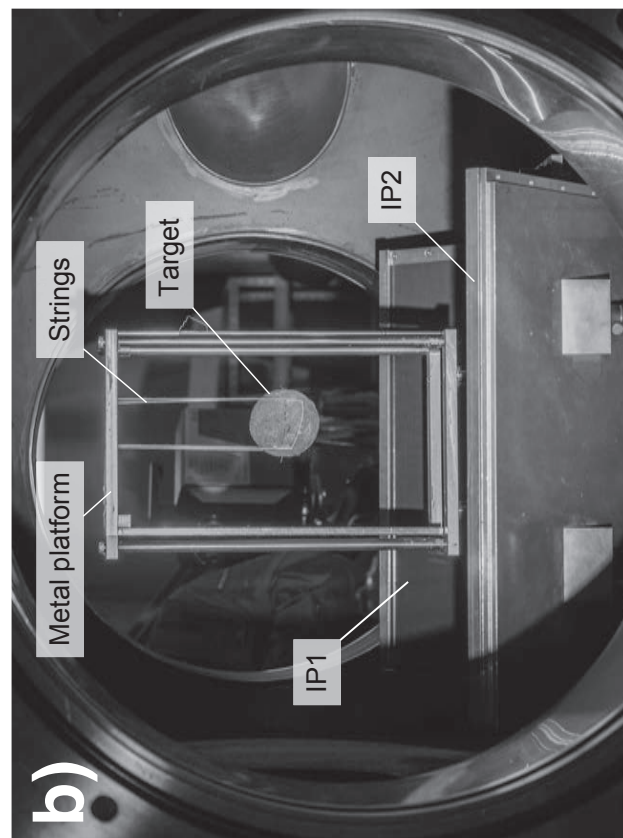
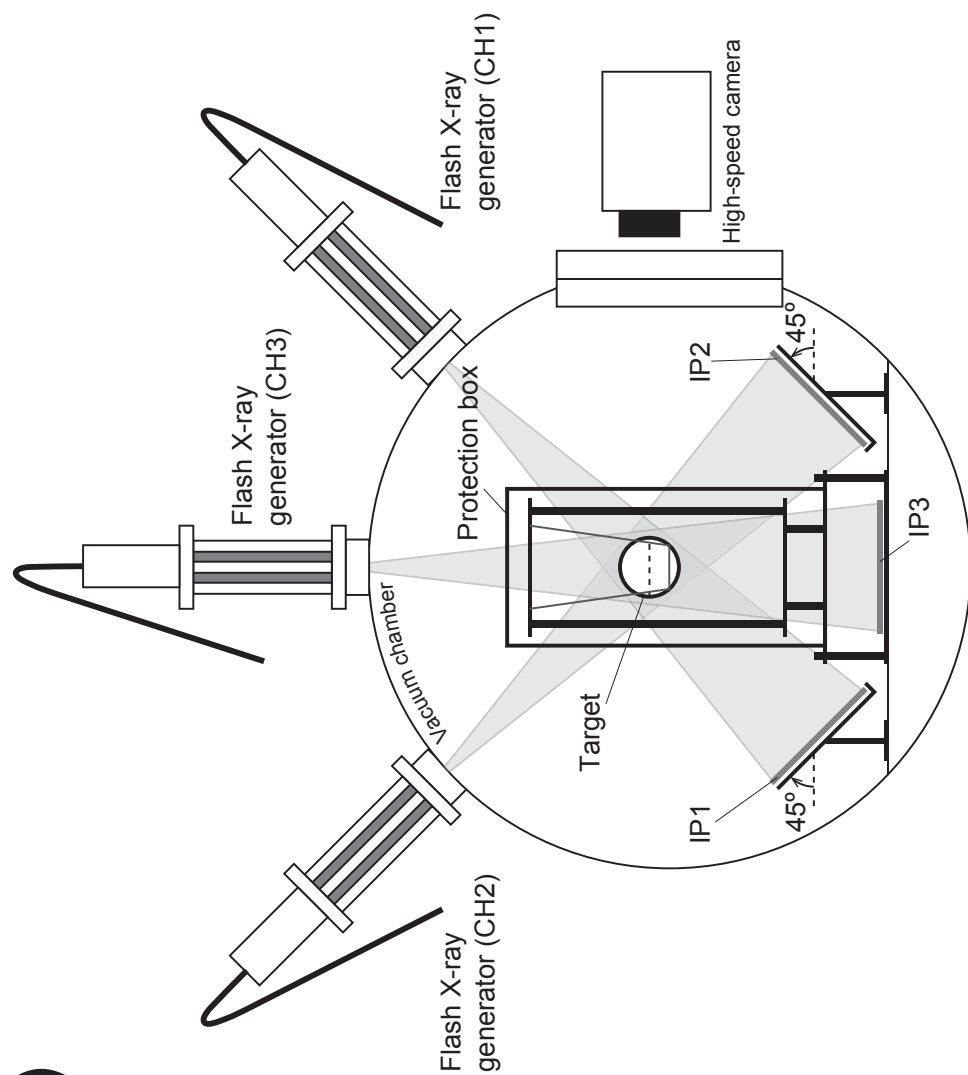
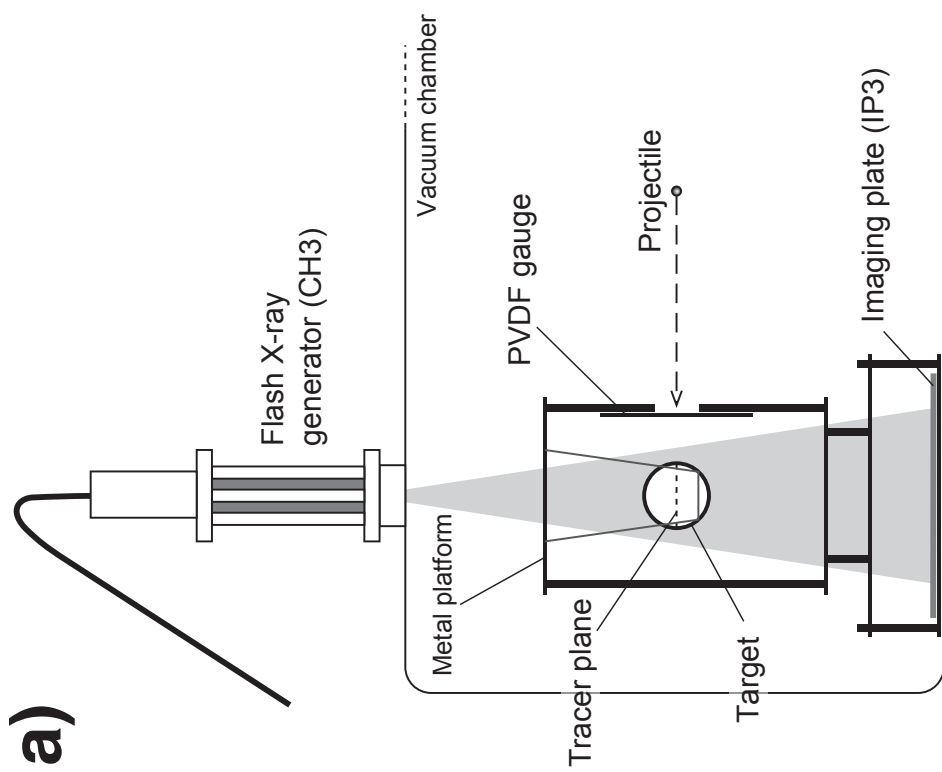
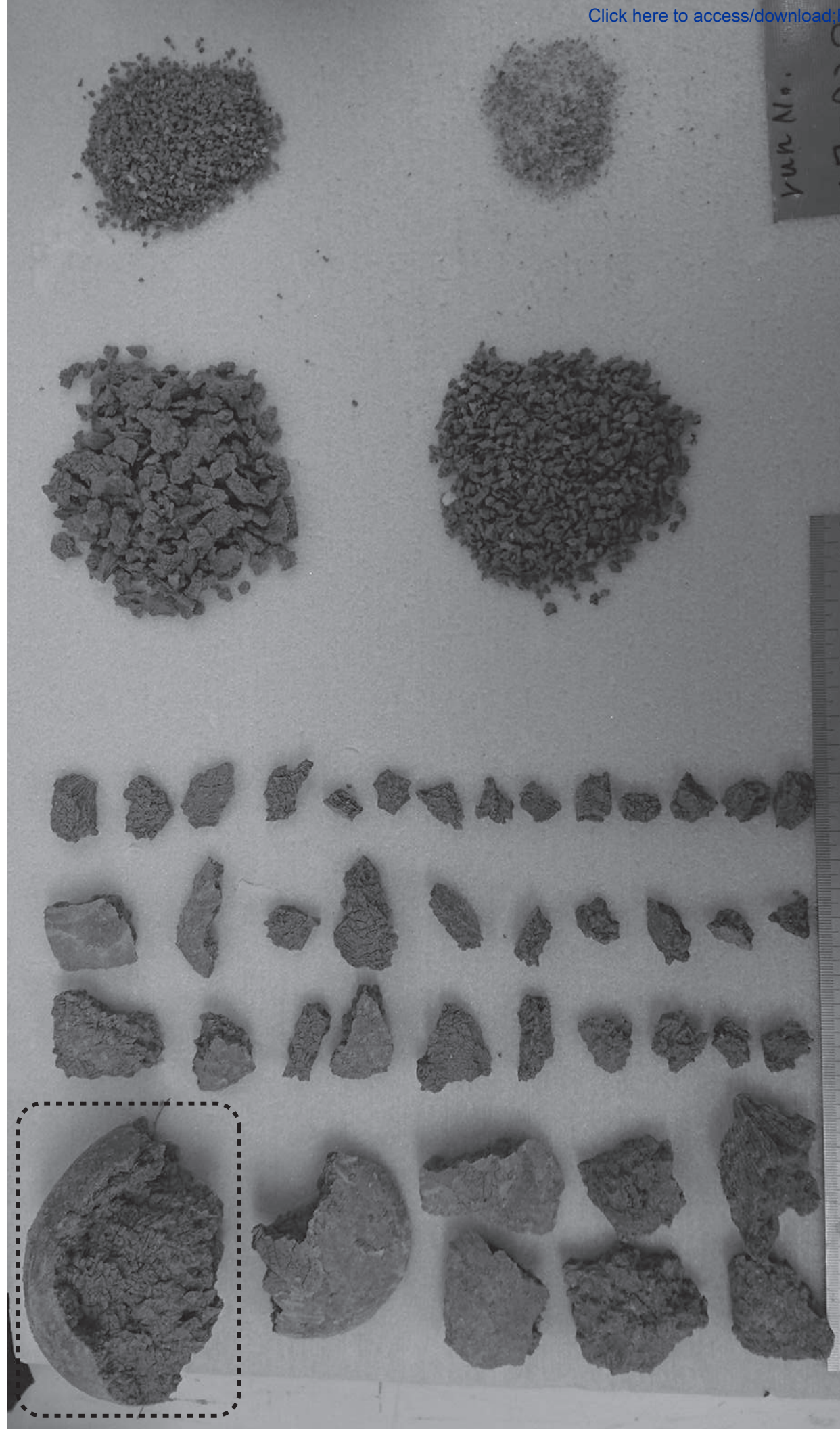


Figure4

[Click here to access/download;Figure;fig4.eps](#)

Largest fragment



10 cm

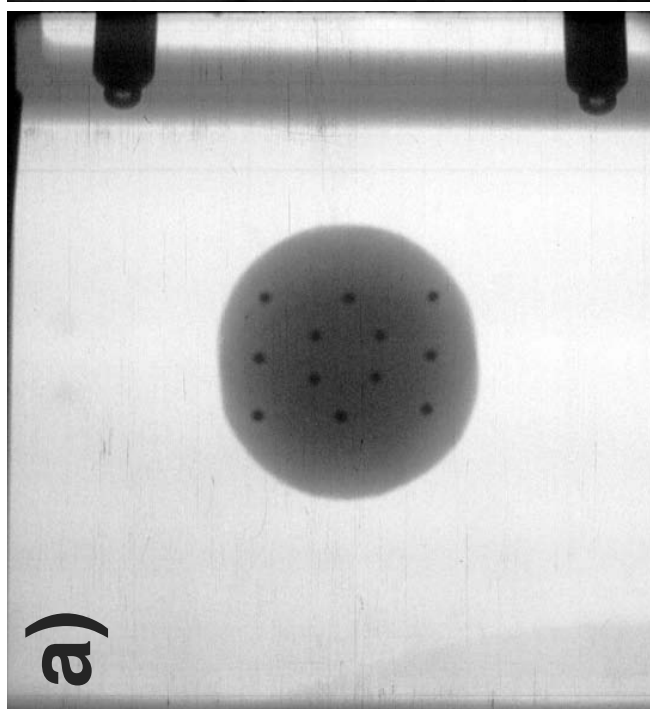
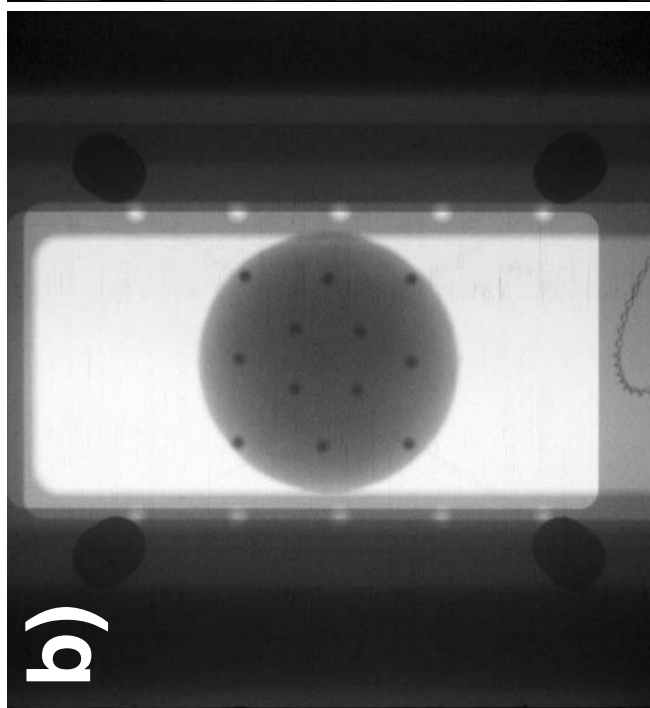
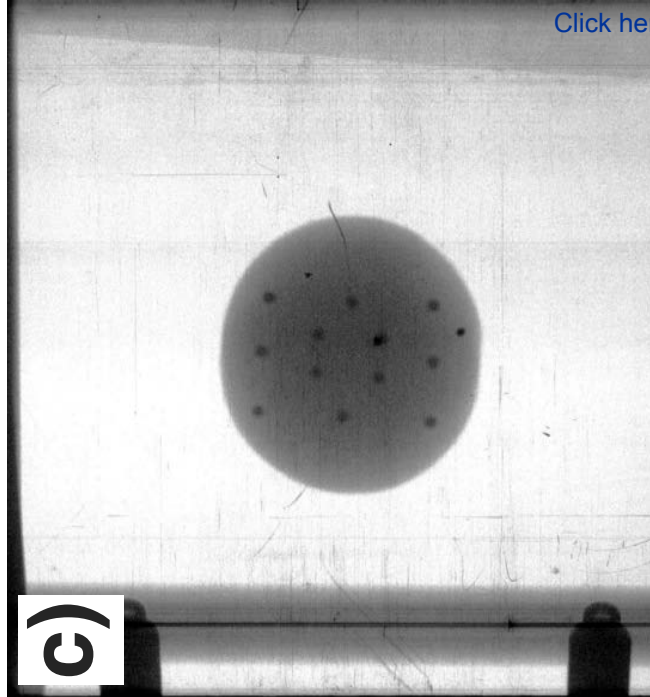
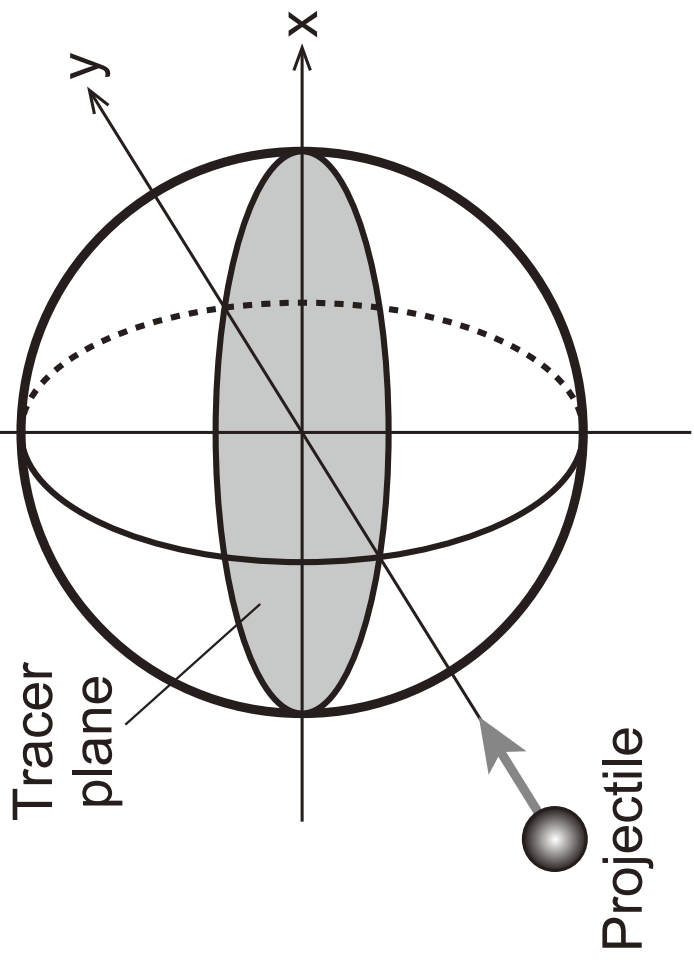


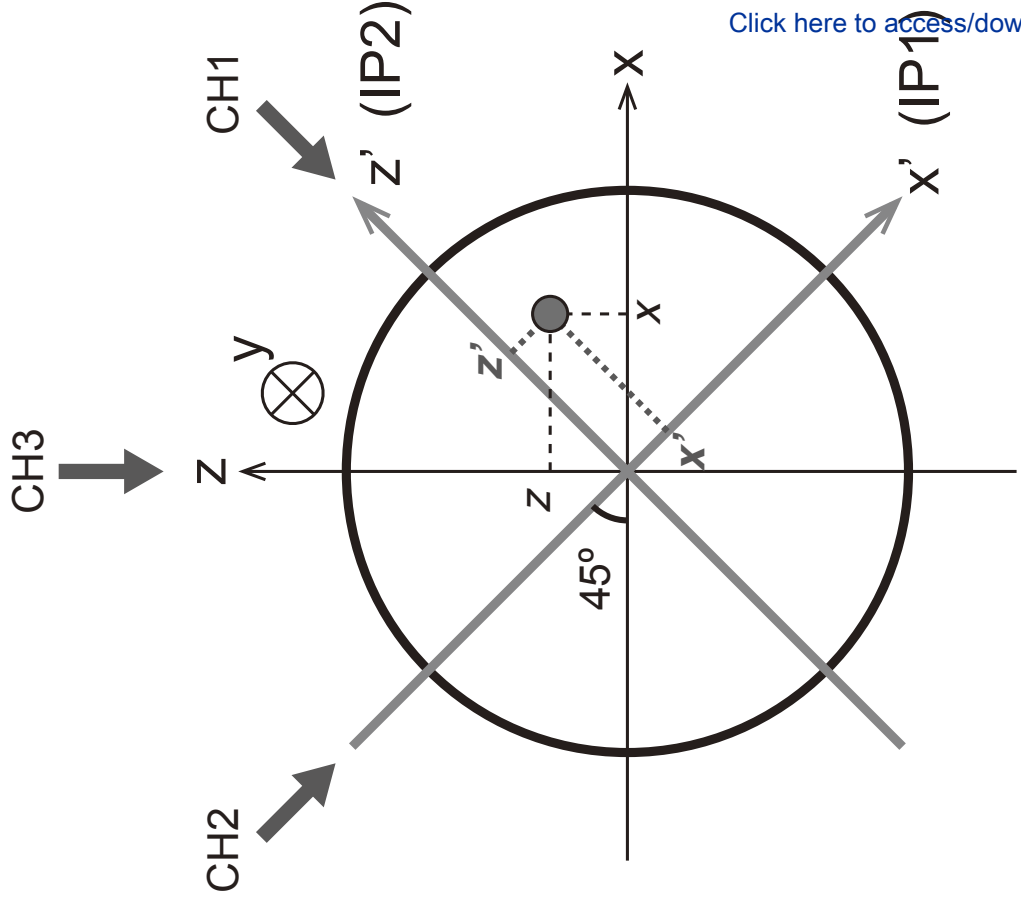
Figure6

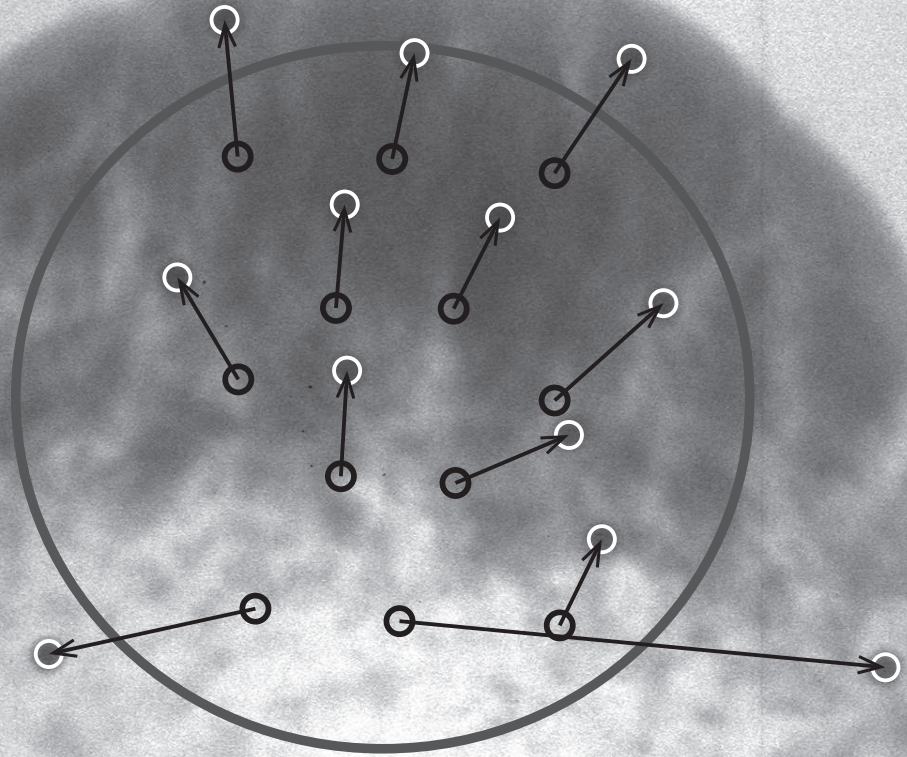
[Click here to access/download;Figure;fig6.eps](#)

a)



b)





[Click here to access/download;Figure;fig8.eps](#)

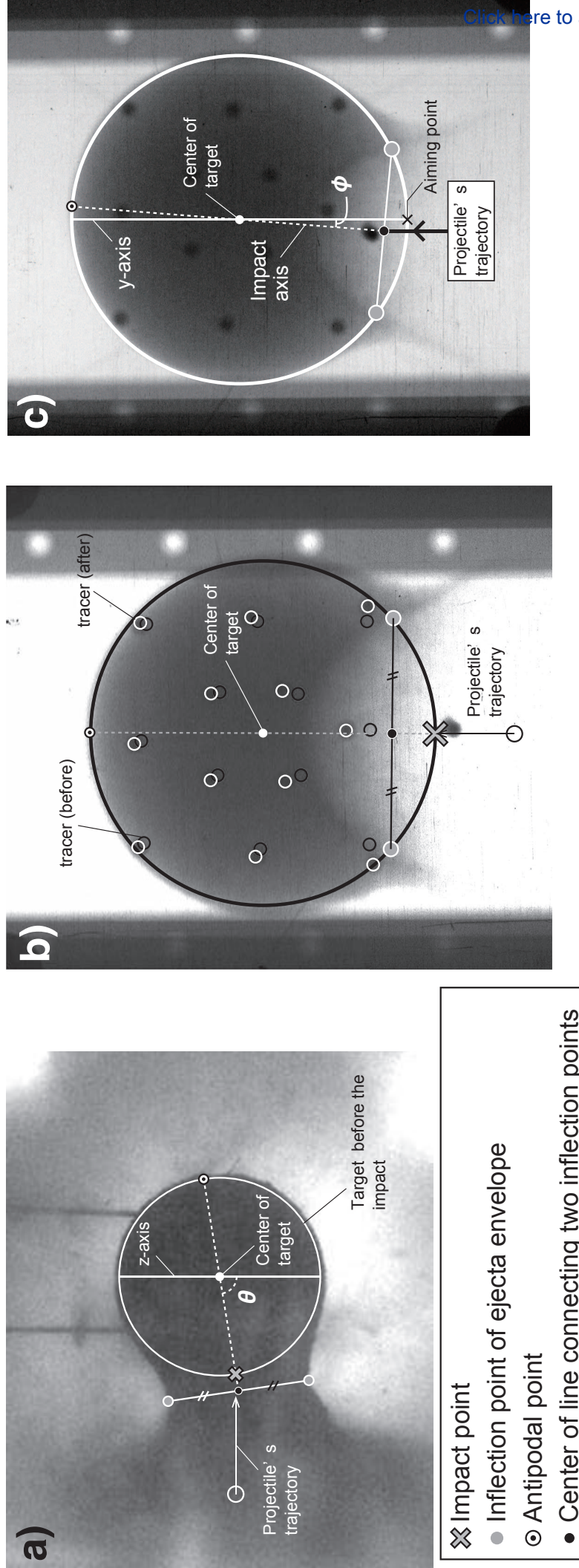


Figure9

[Click here to access/download;Figure;fig9.eps](#)

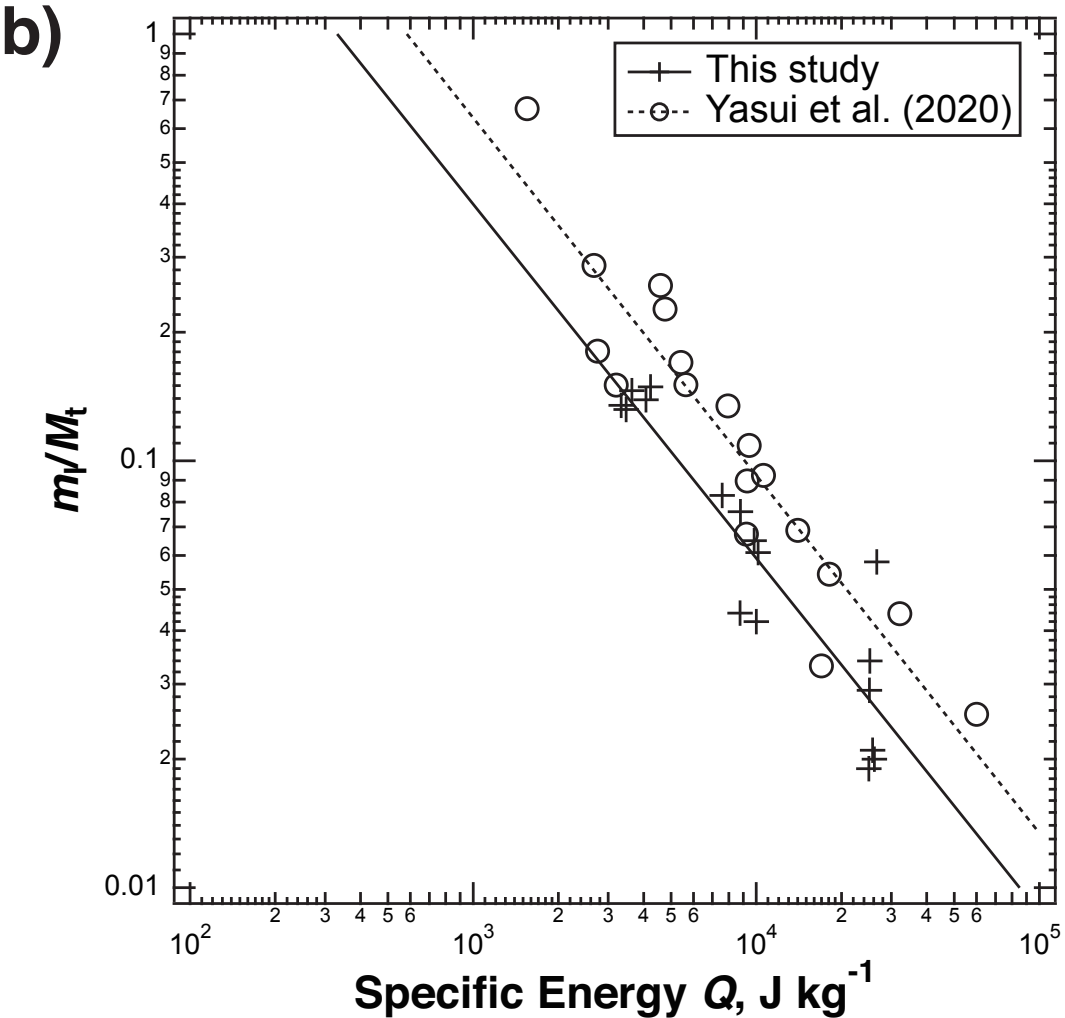
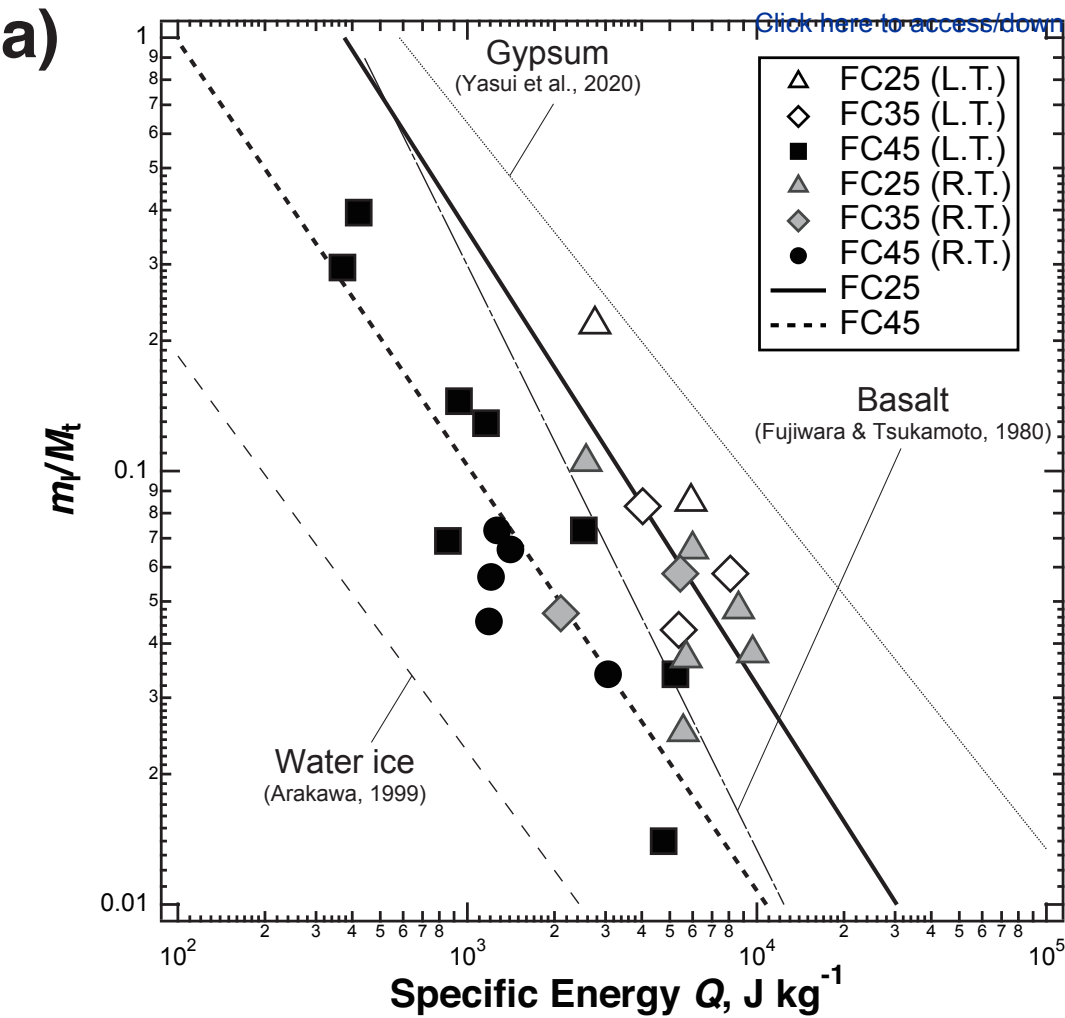
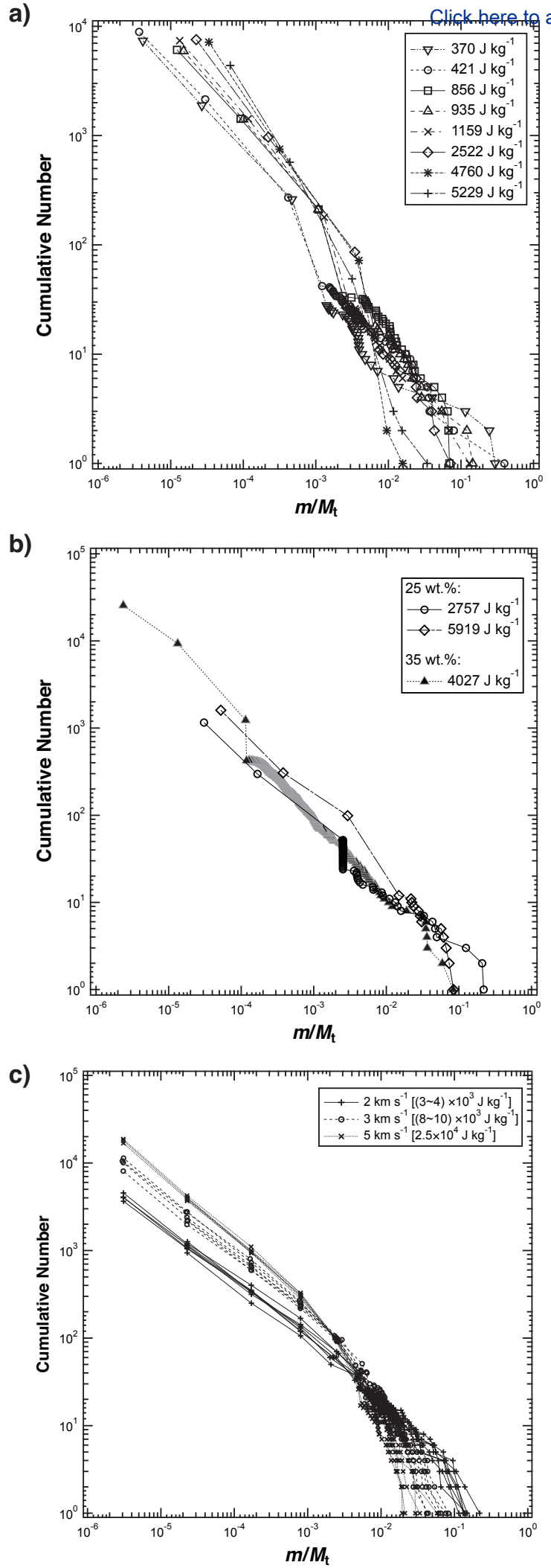
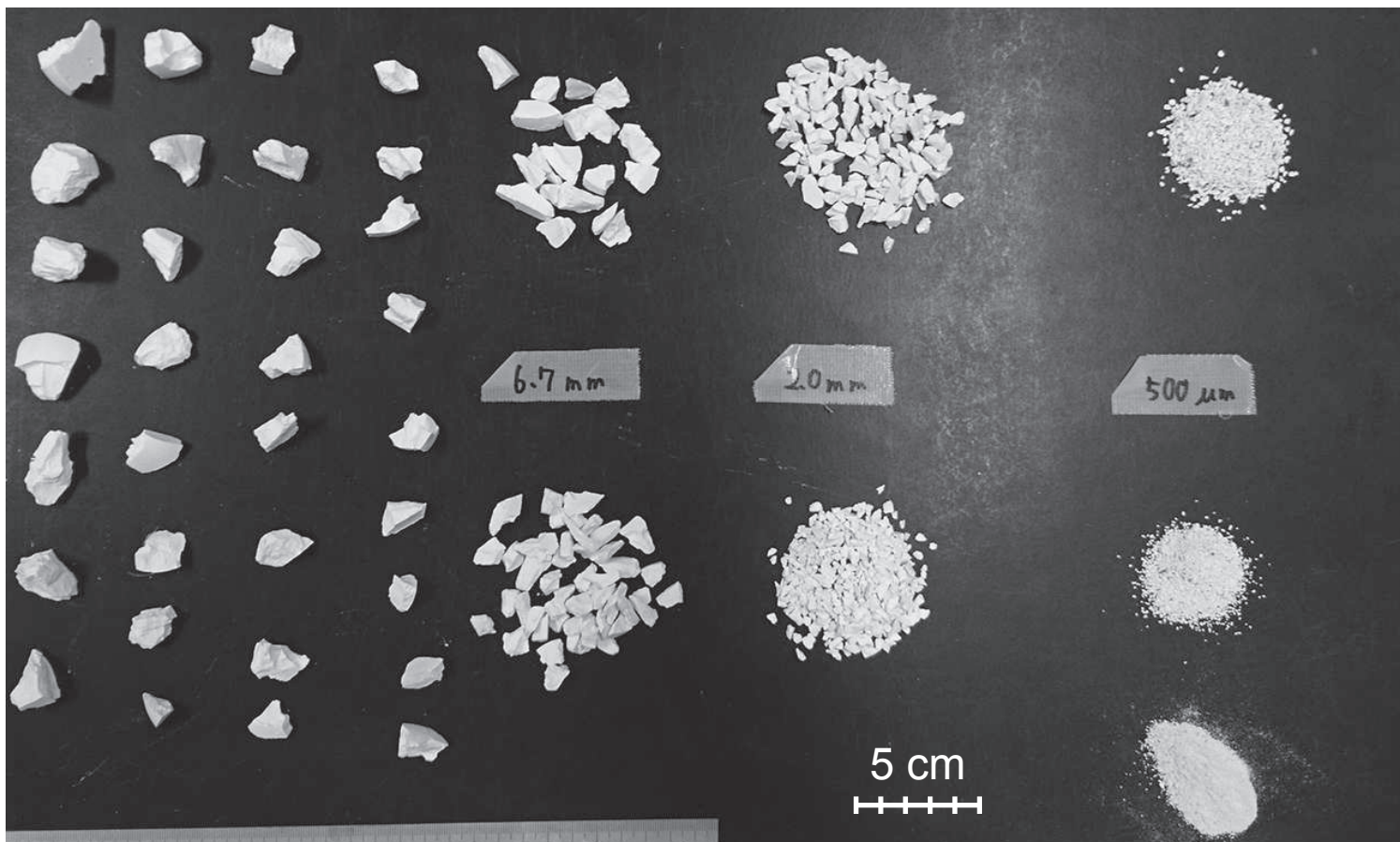


Figure10



a)**b)**

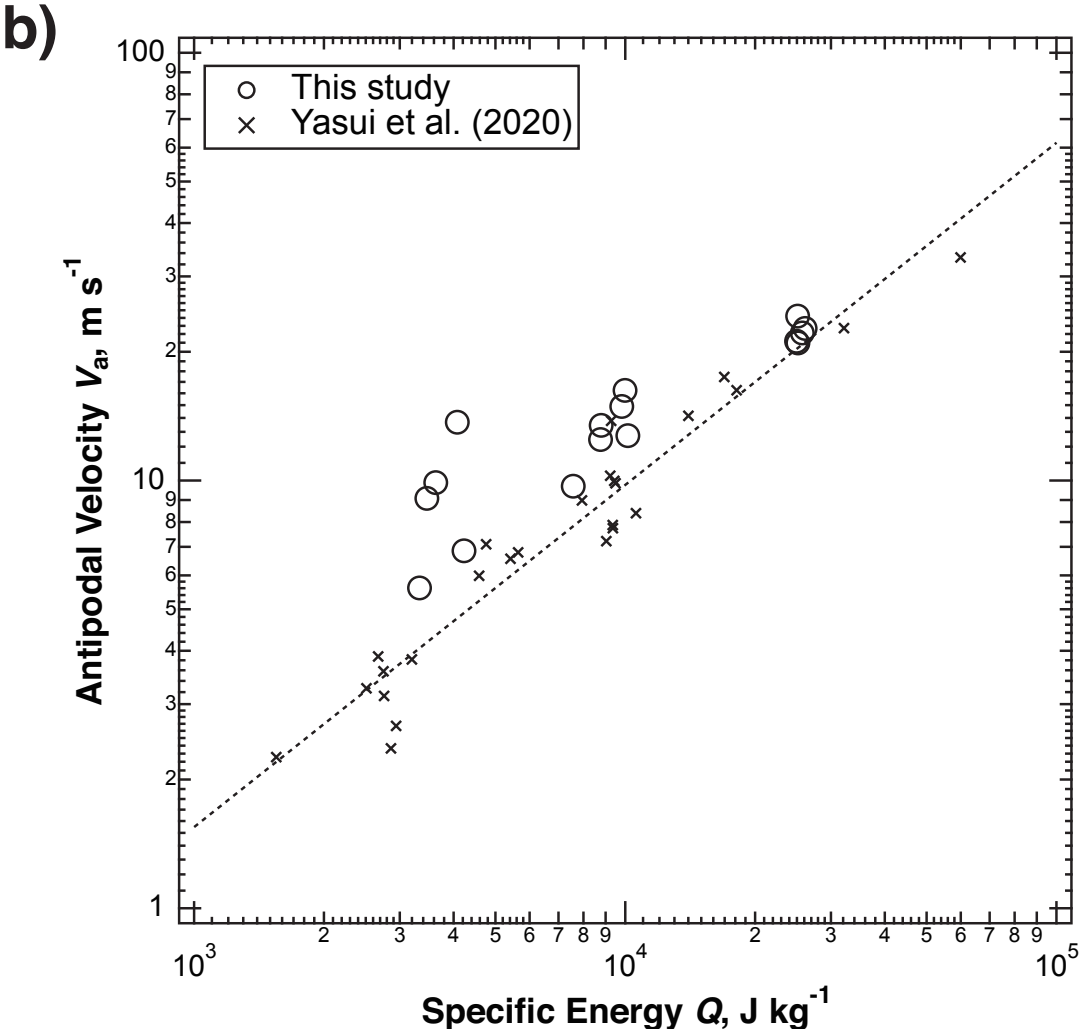
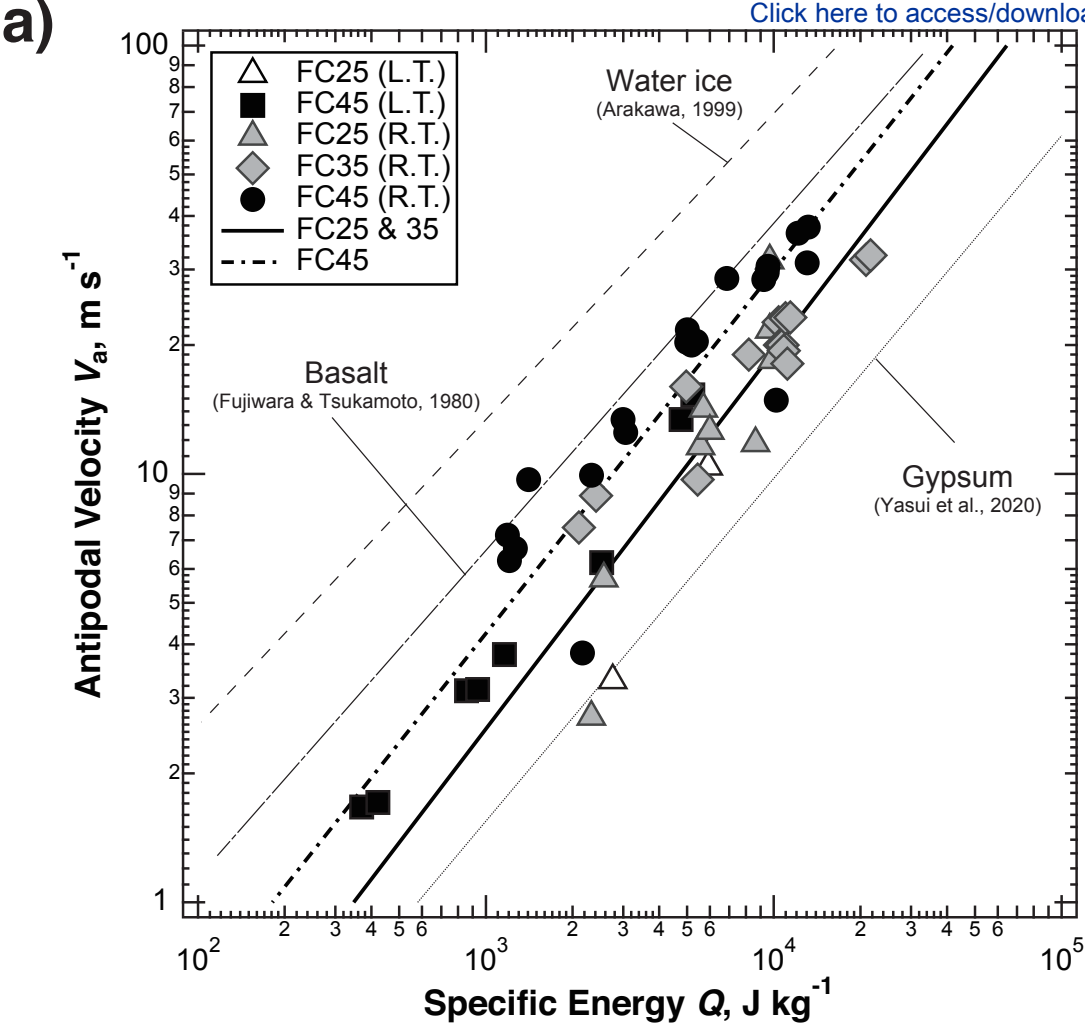
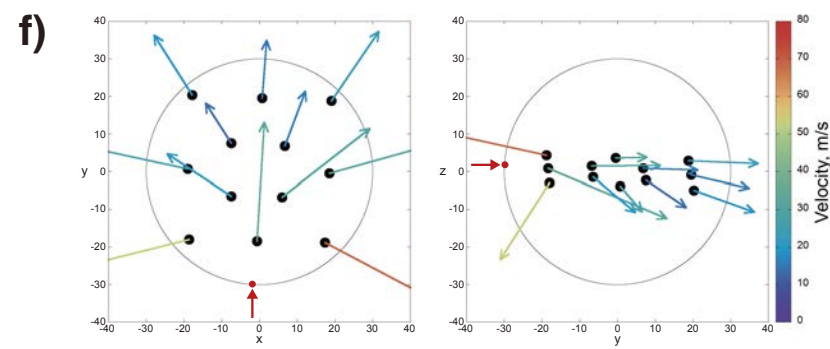
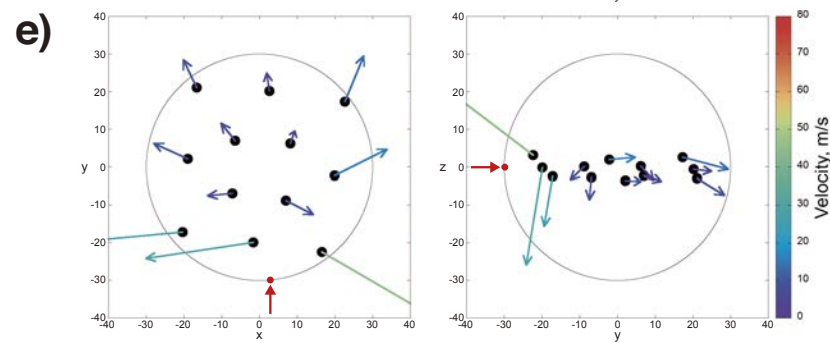
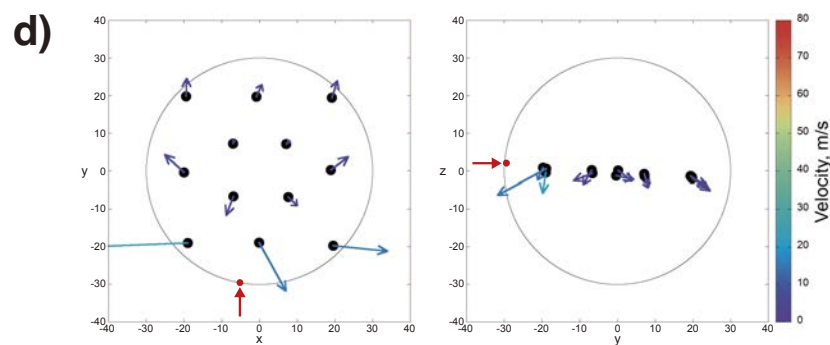
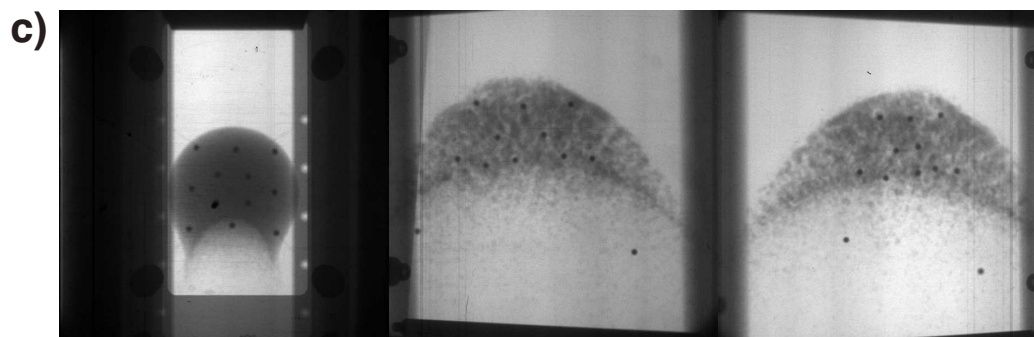
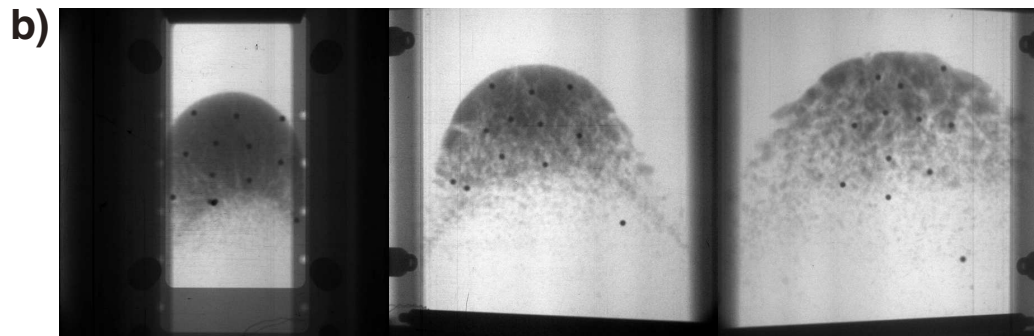
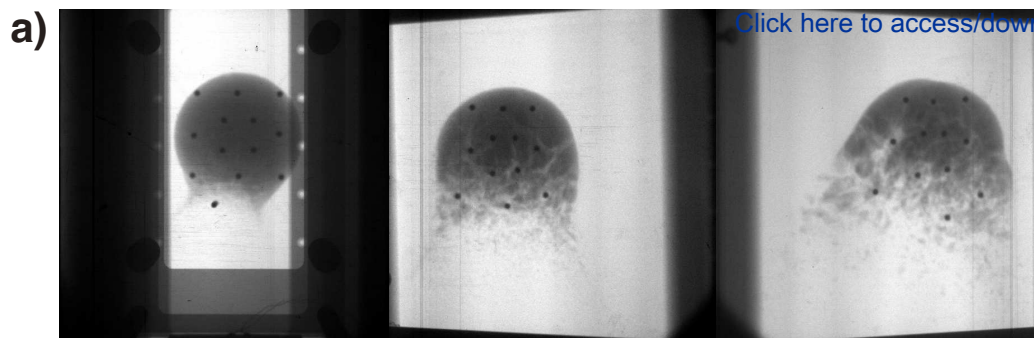
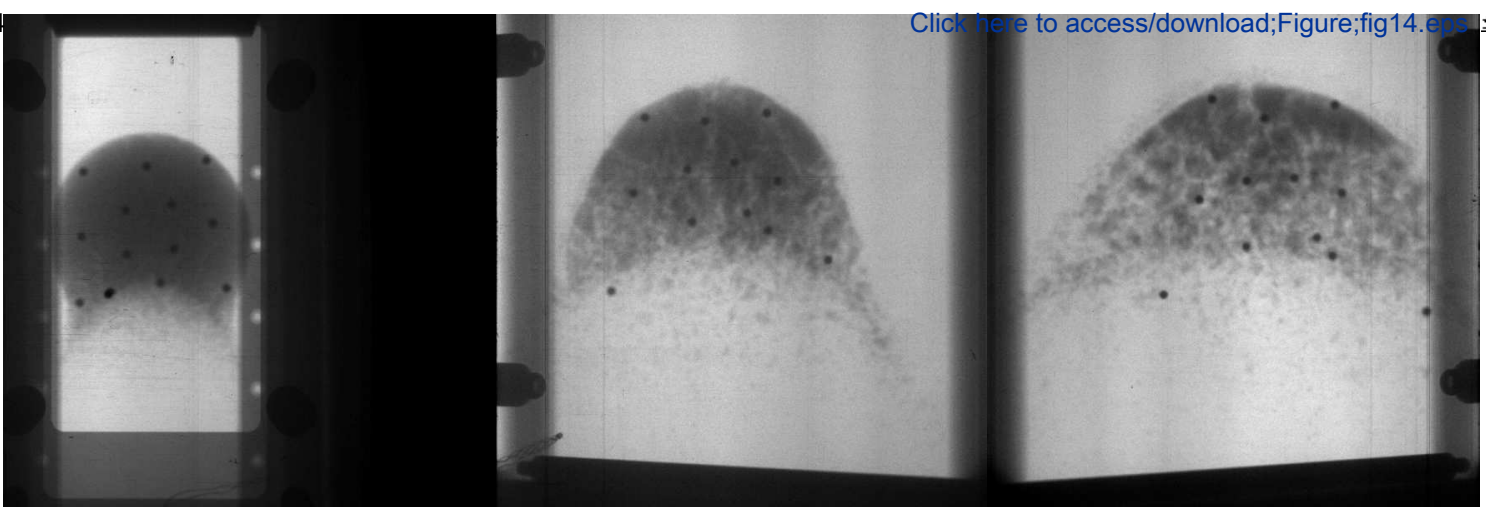


Figure13

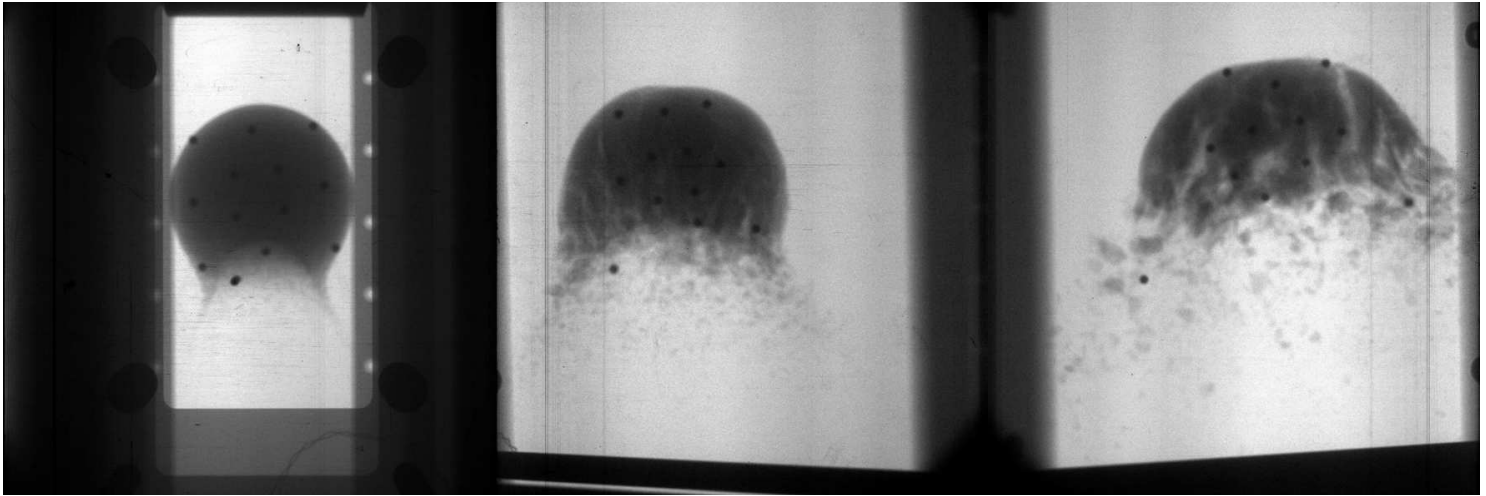
[Click here to access/download;Figure;fig13.eps](#)



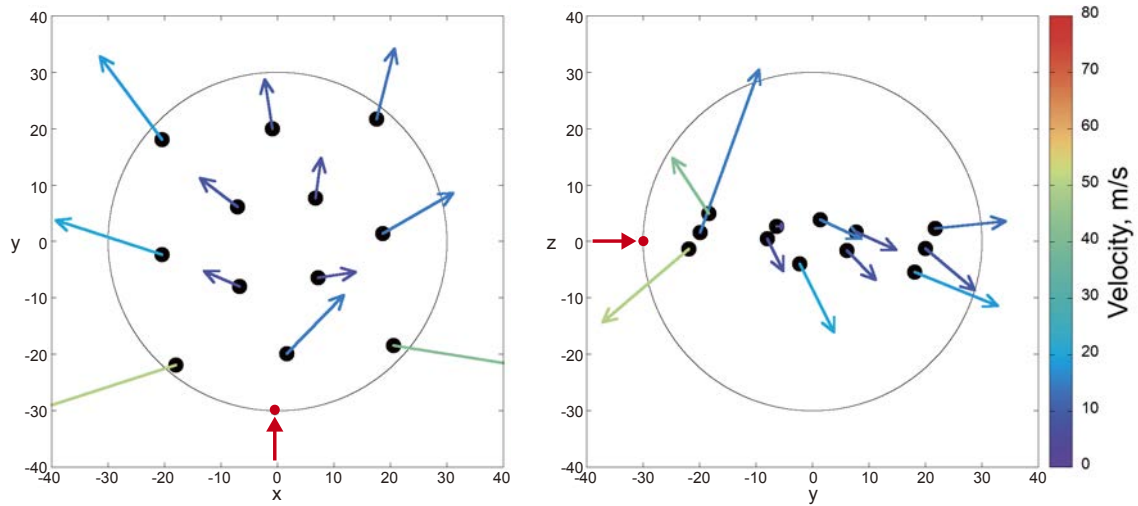
a)



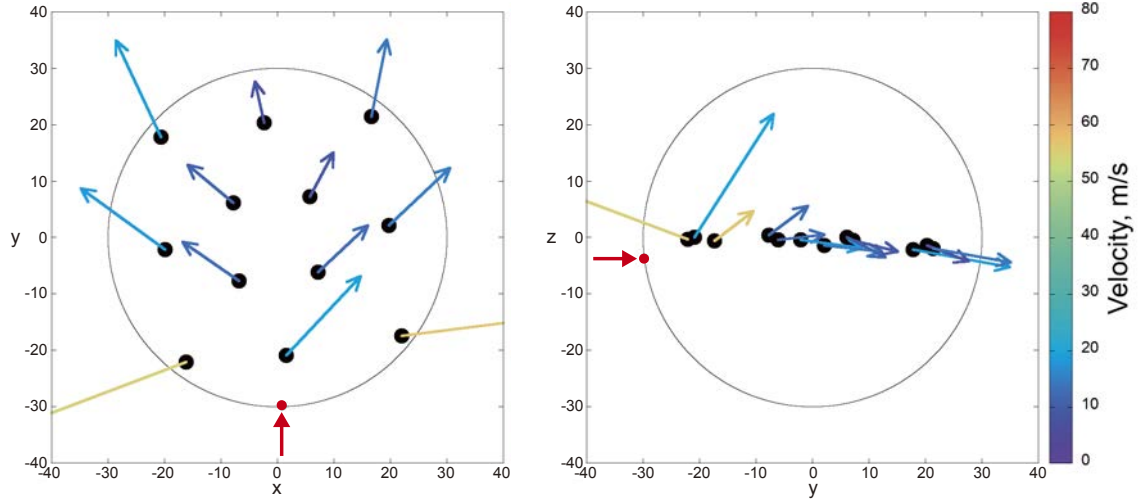
b)

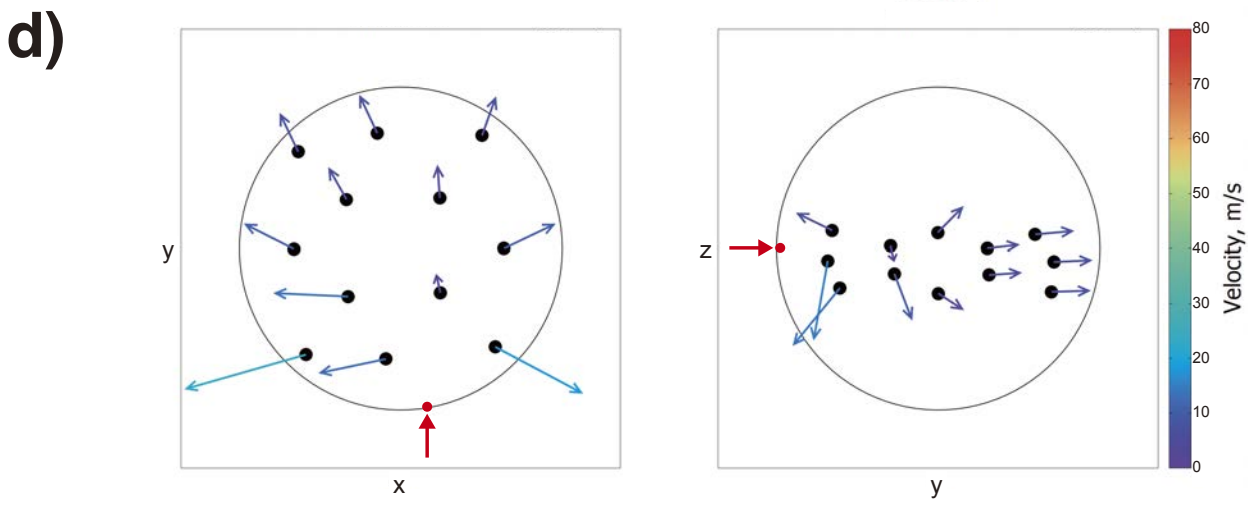
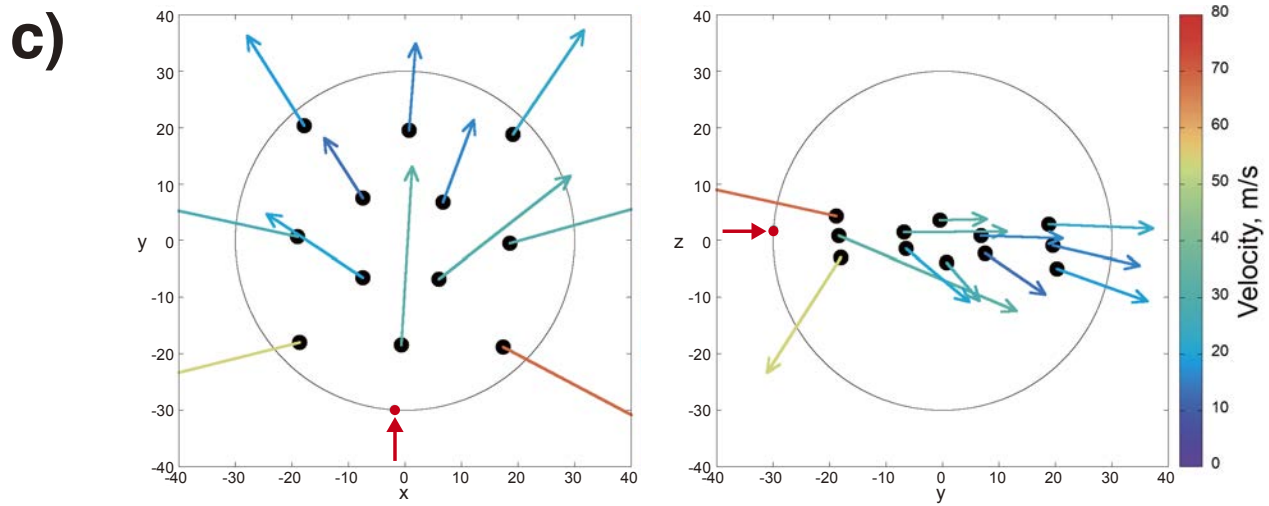
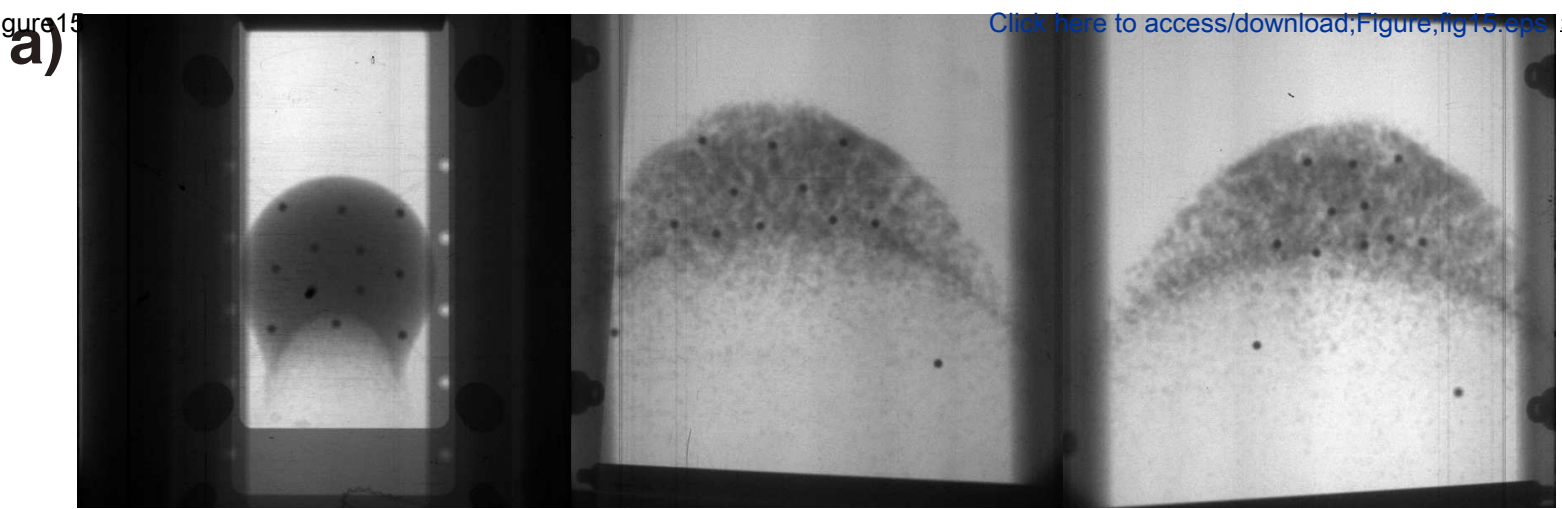


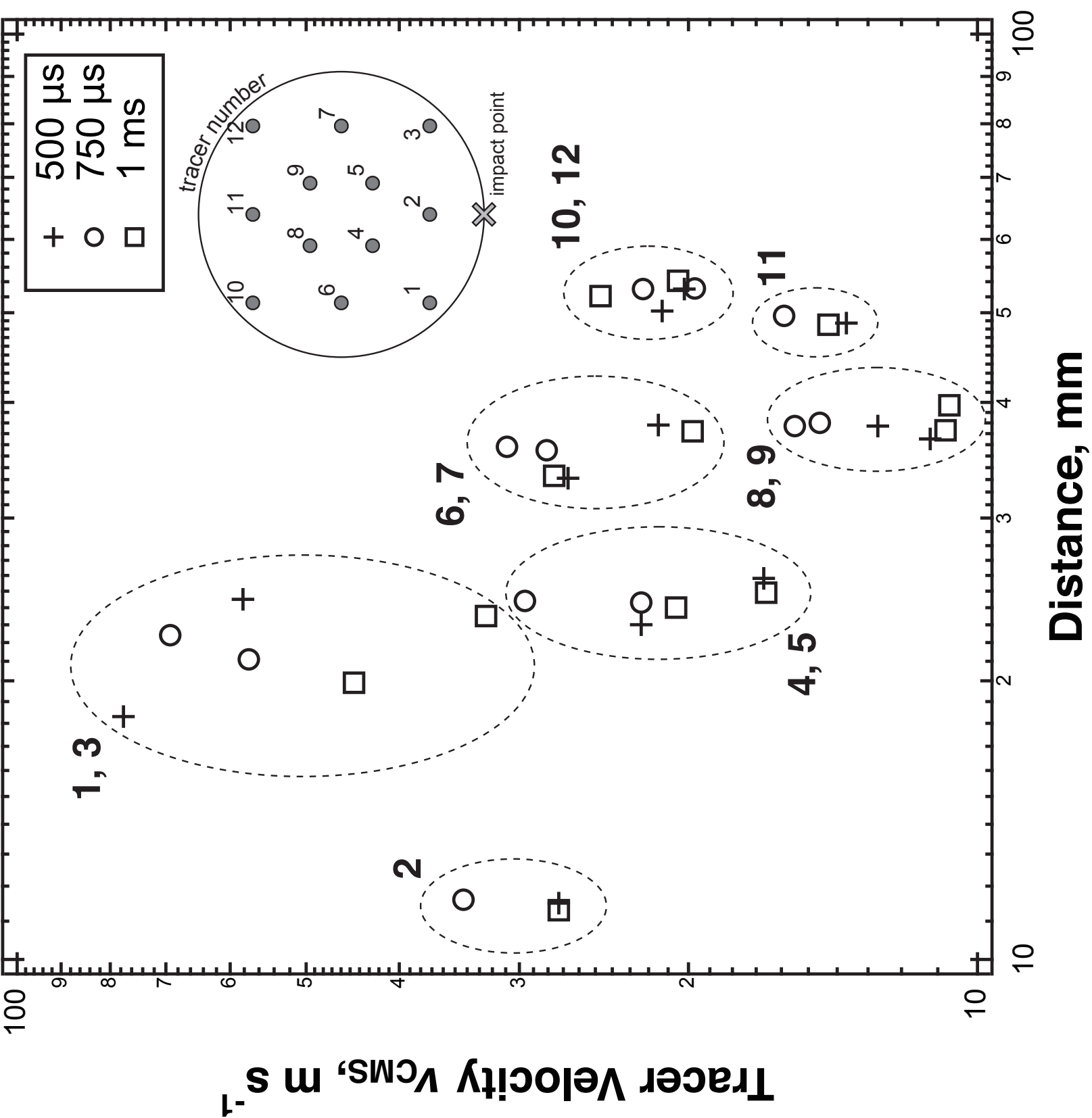
c)



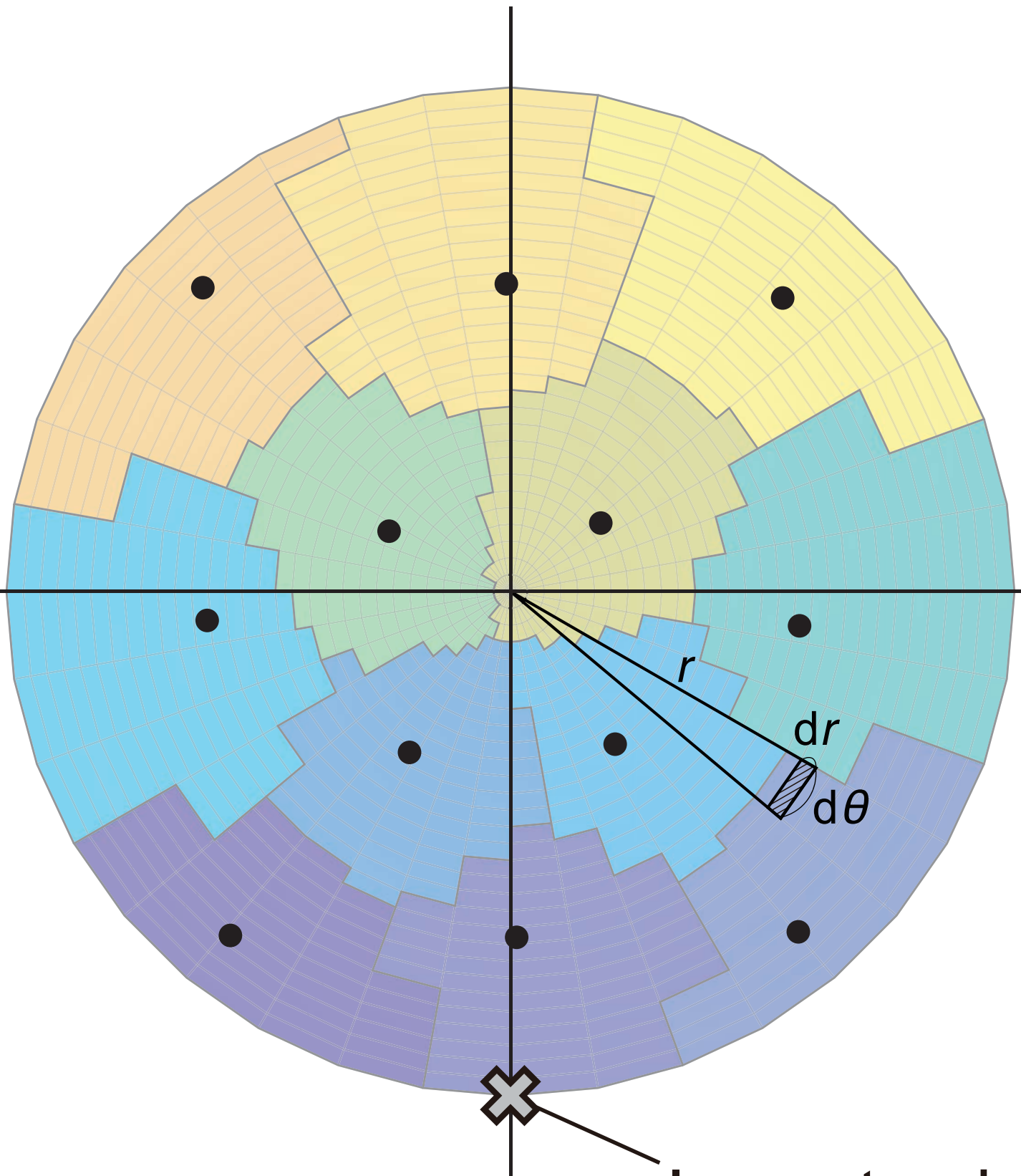
d)







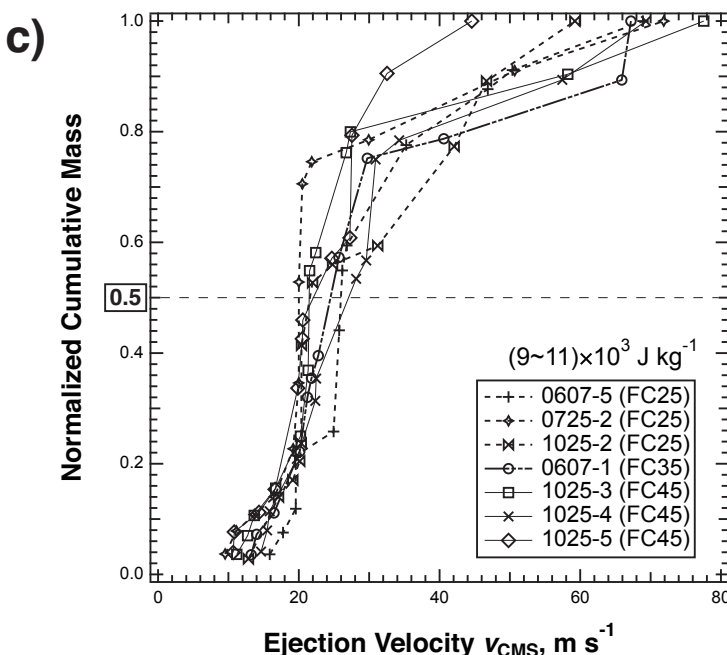
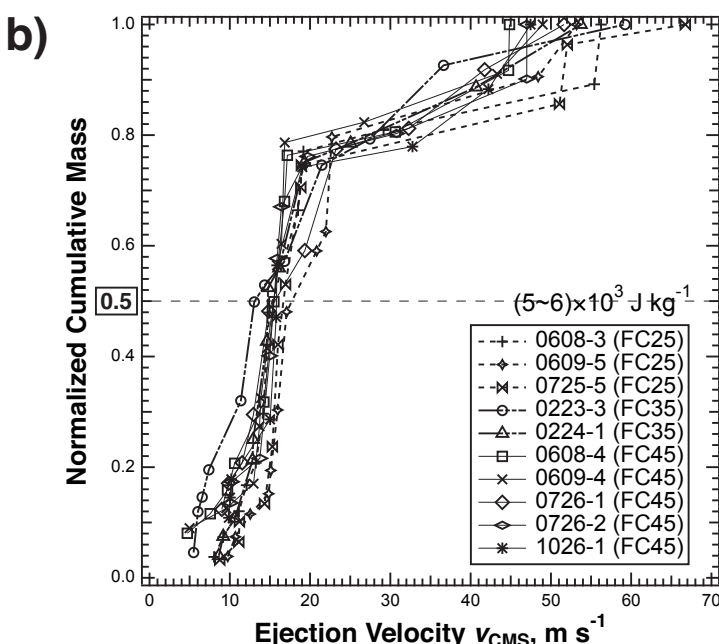
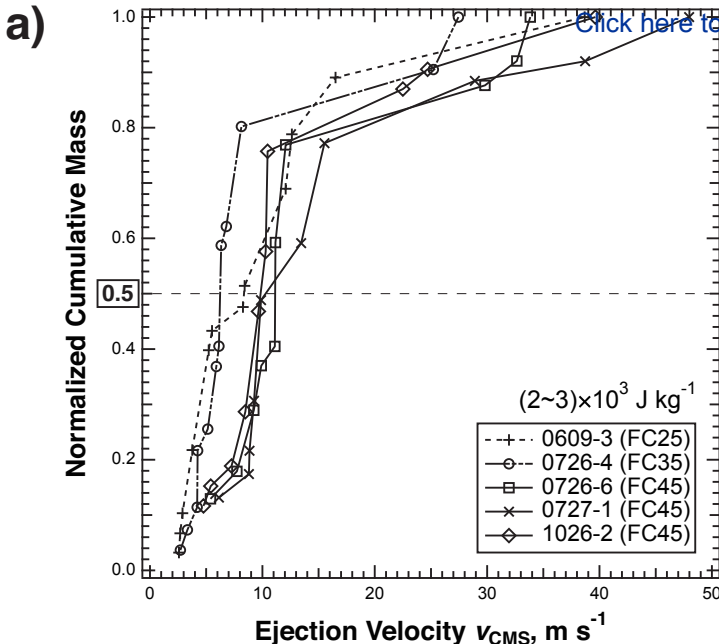
Impact axis

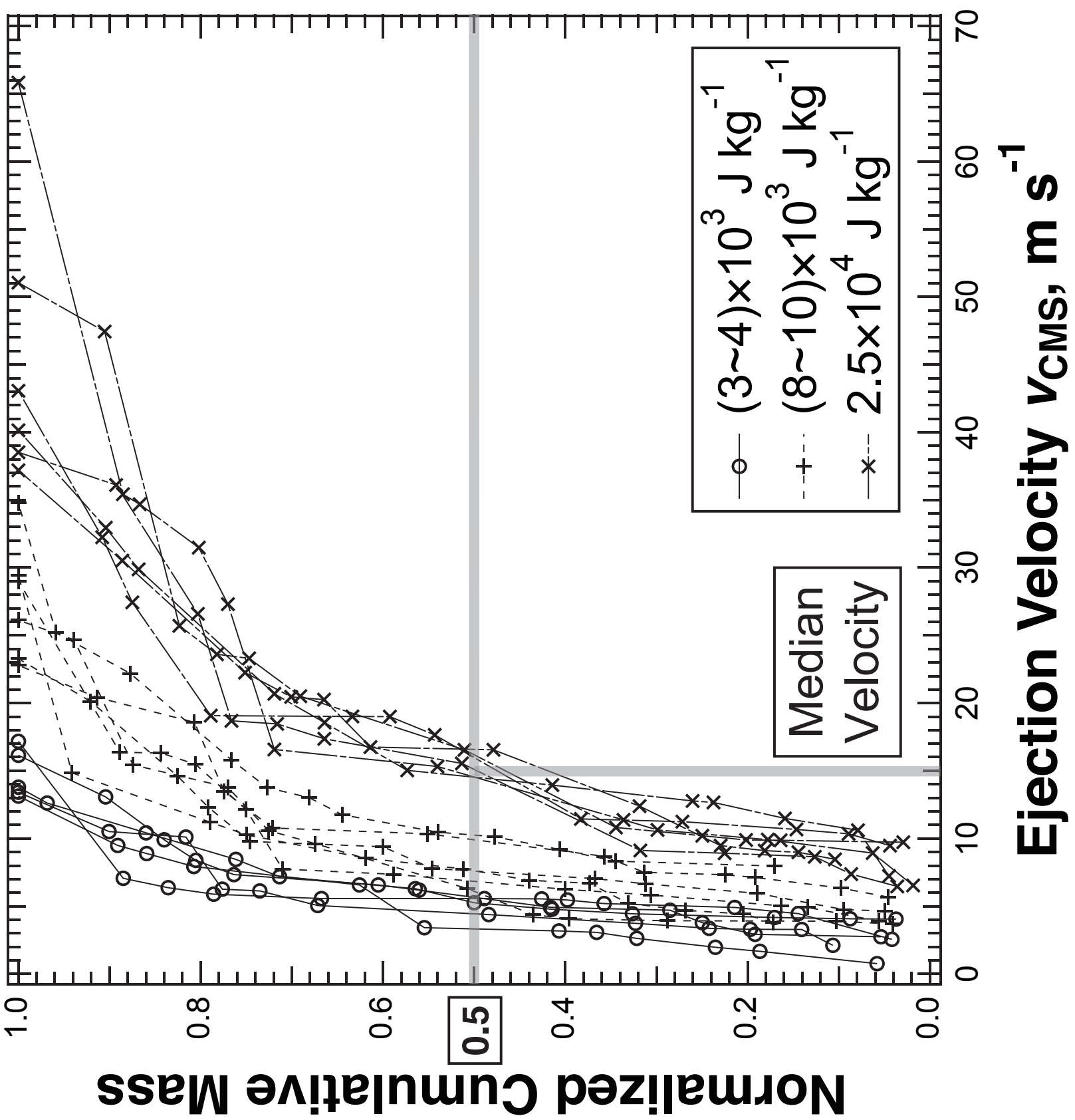


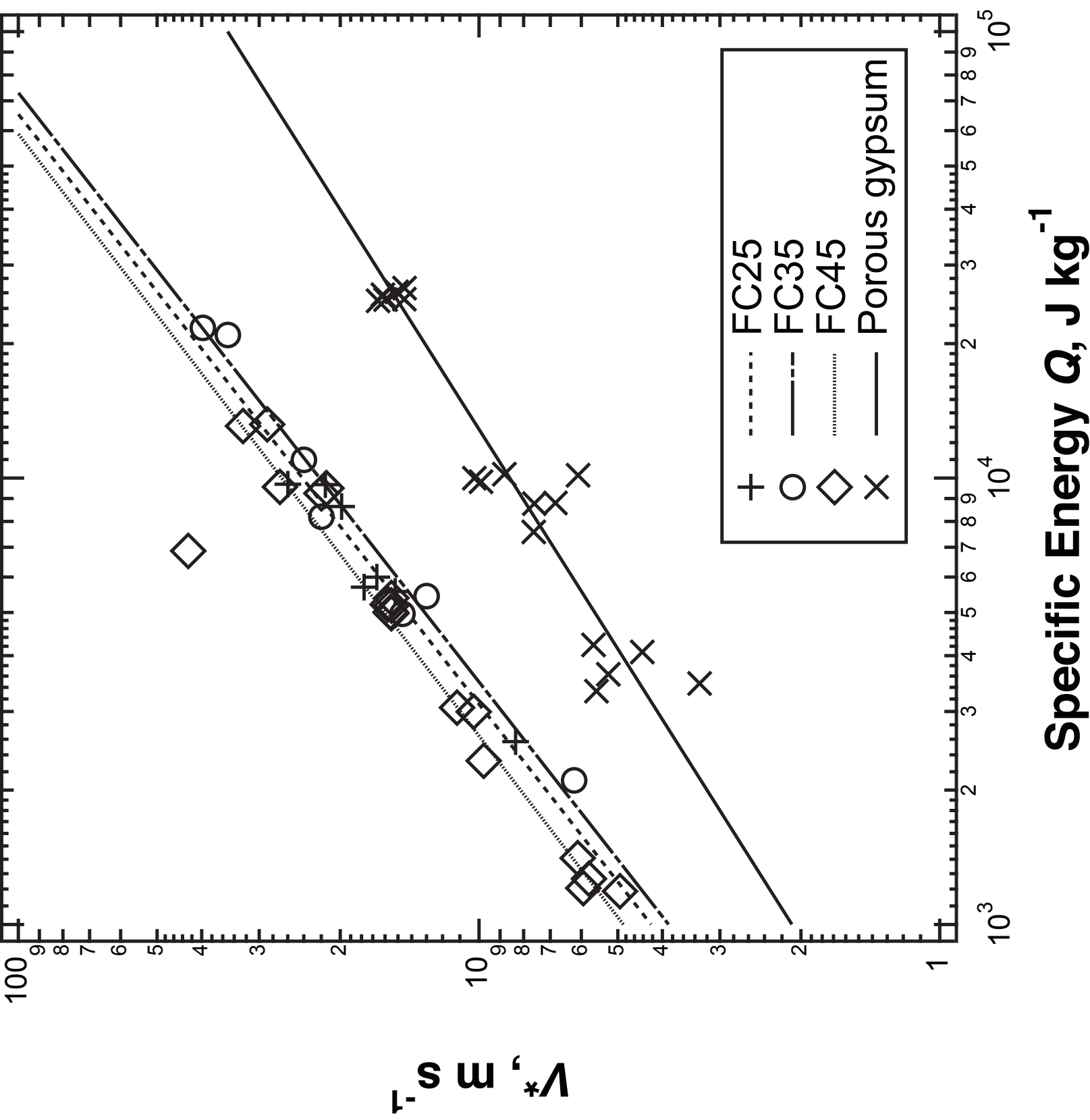
Impact point

Figure18

[Click here to access/download;Figure;fig18.eps](#)







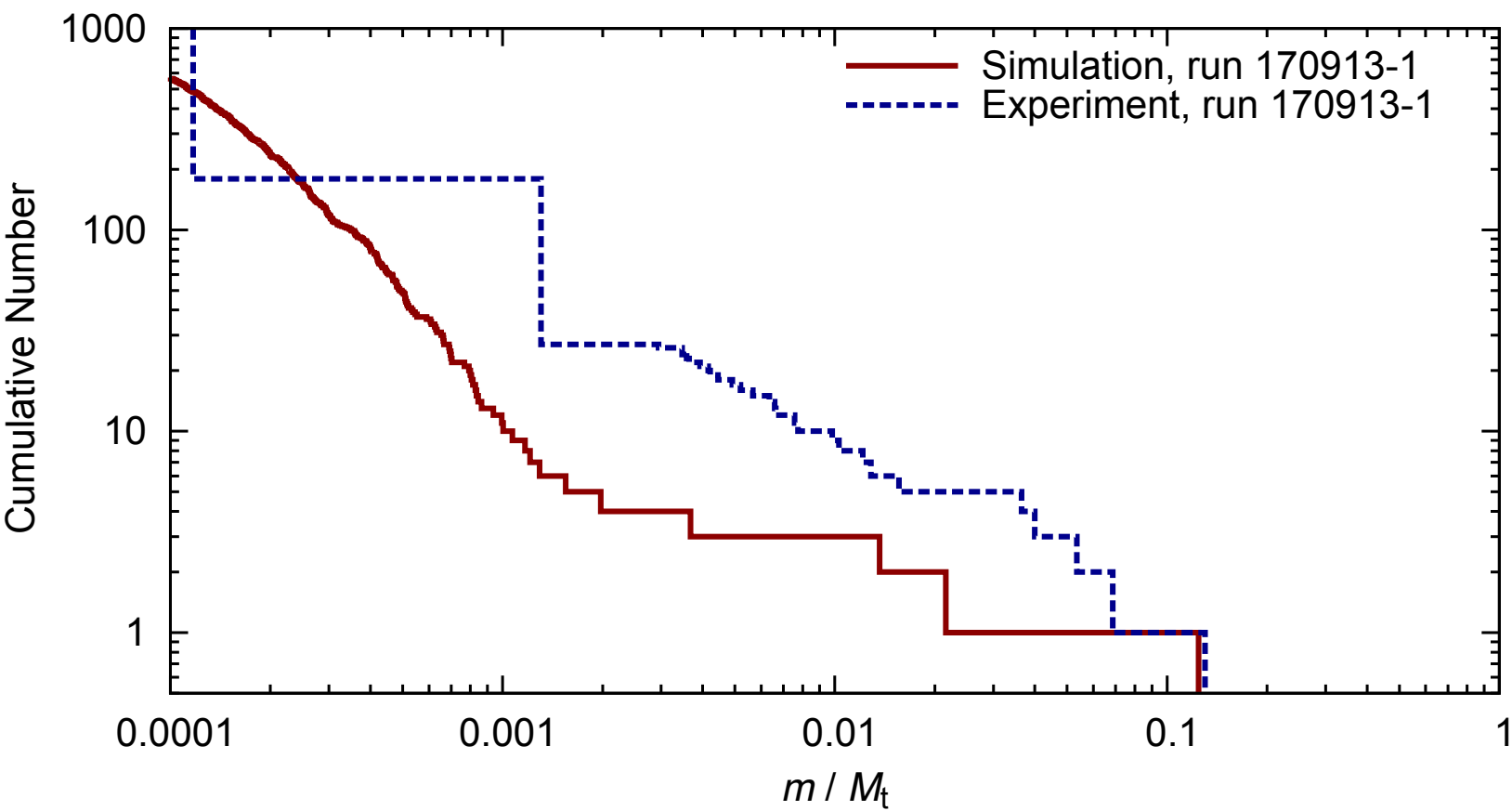
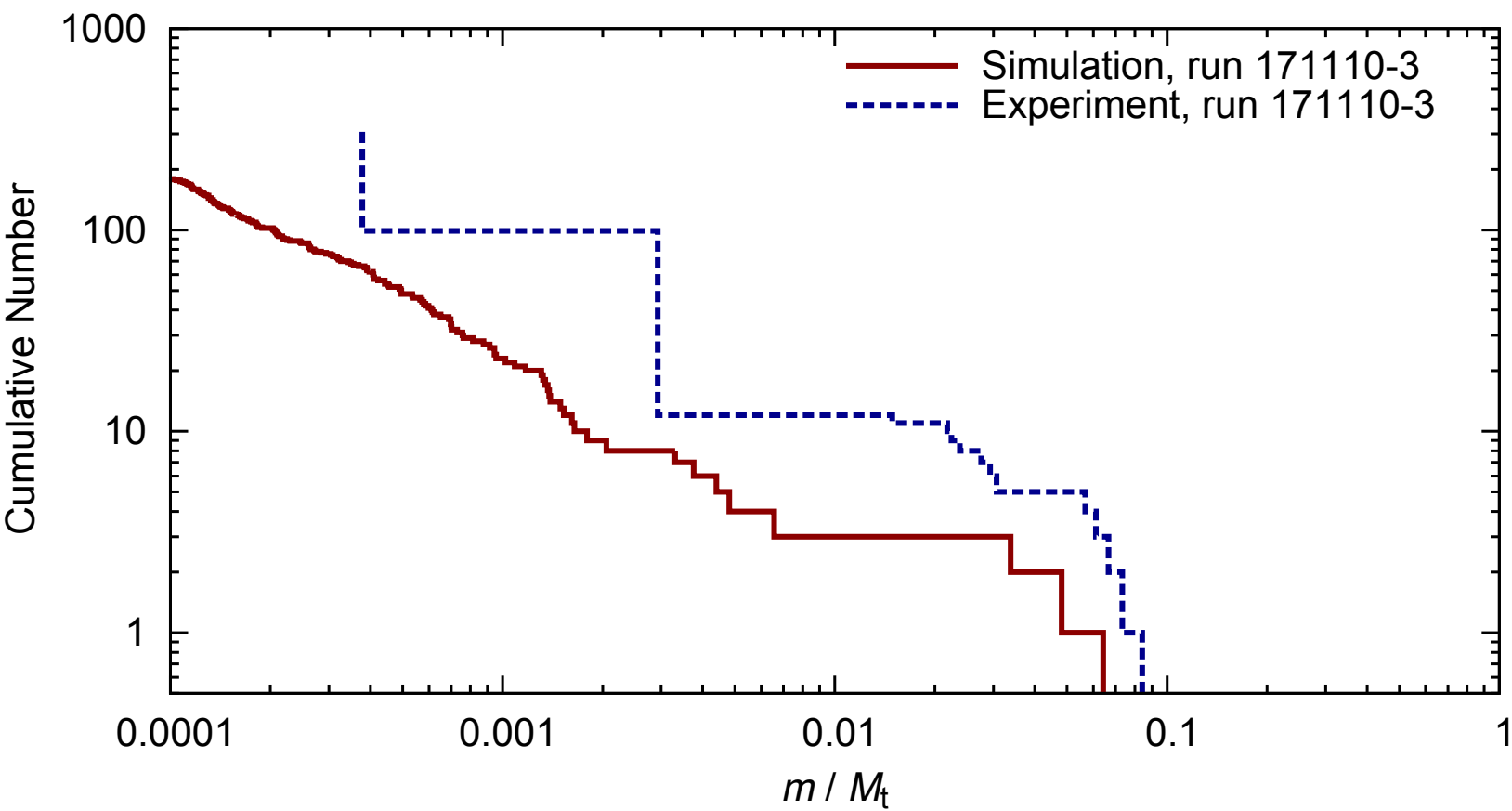


Figure22

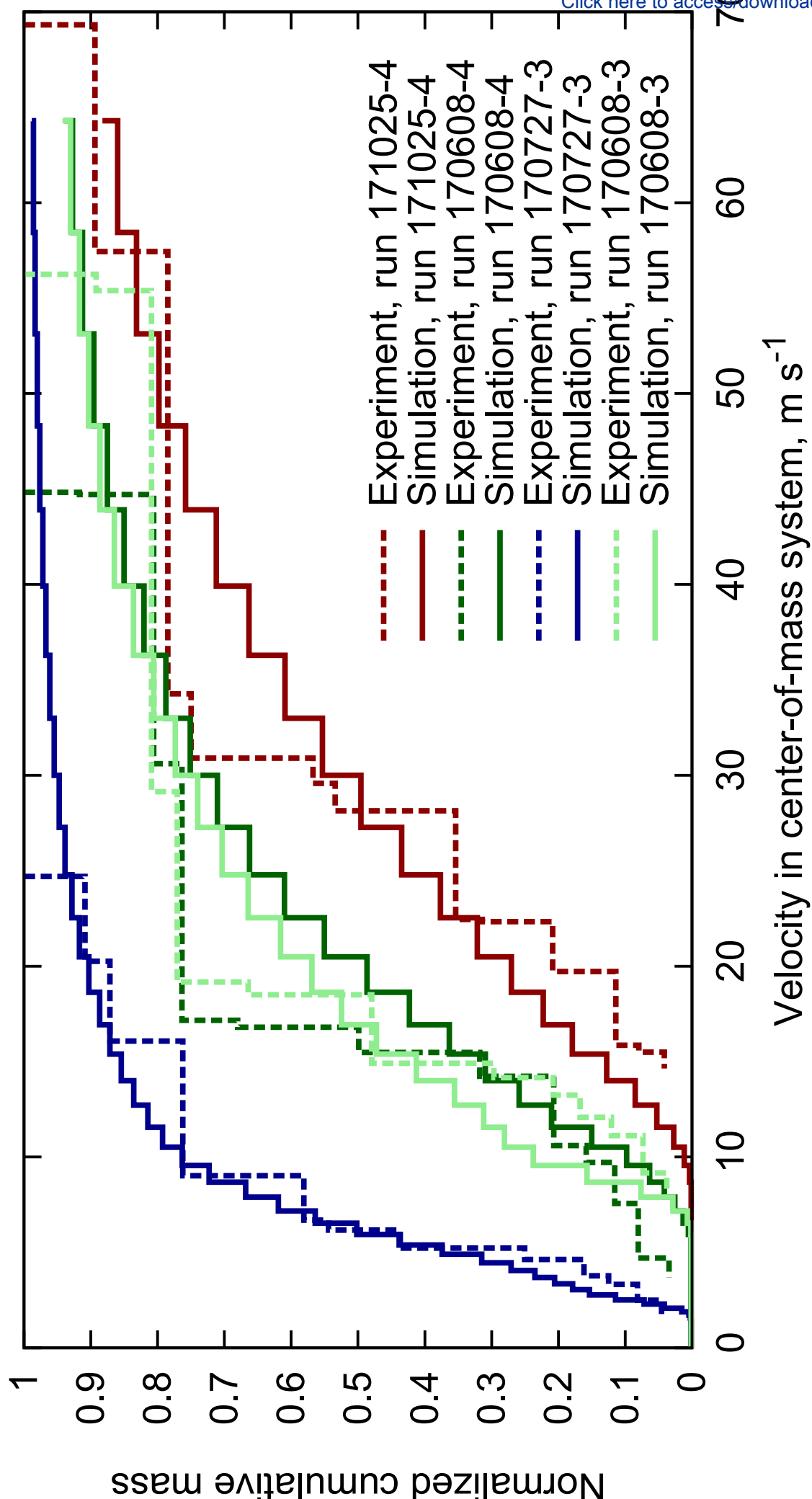


Figure23

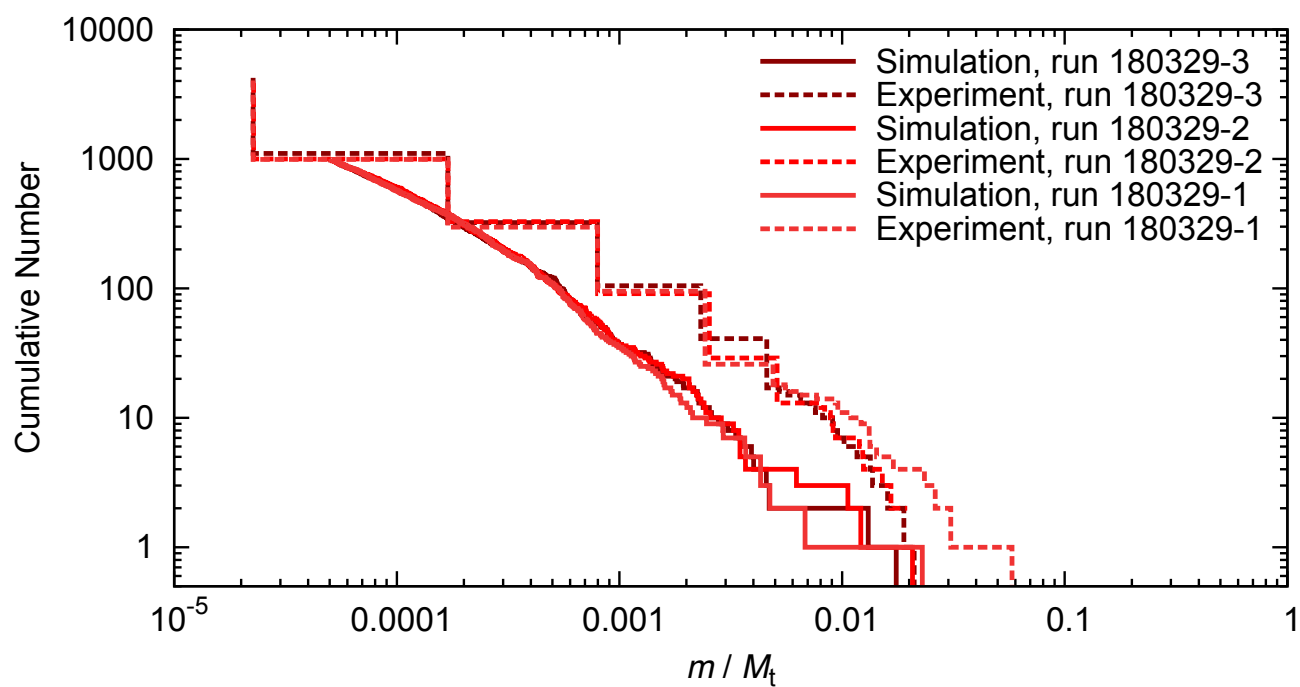
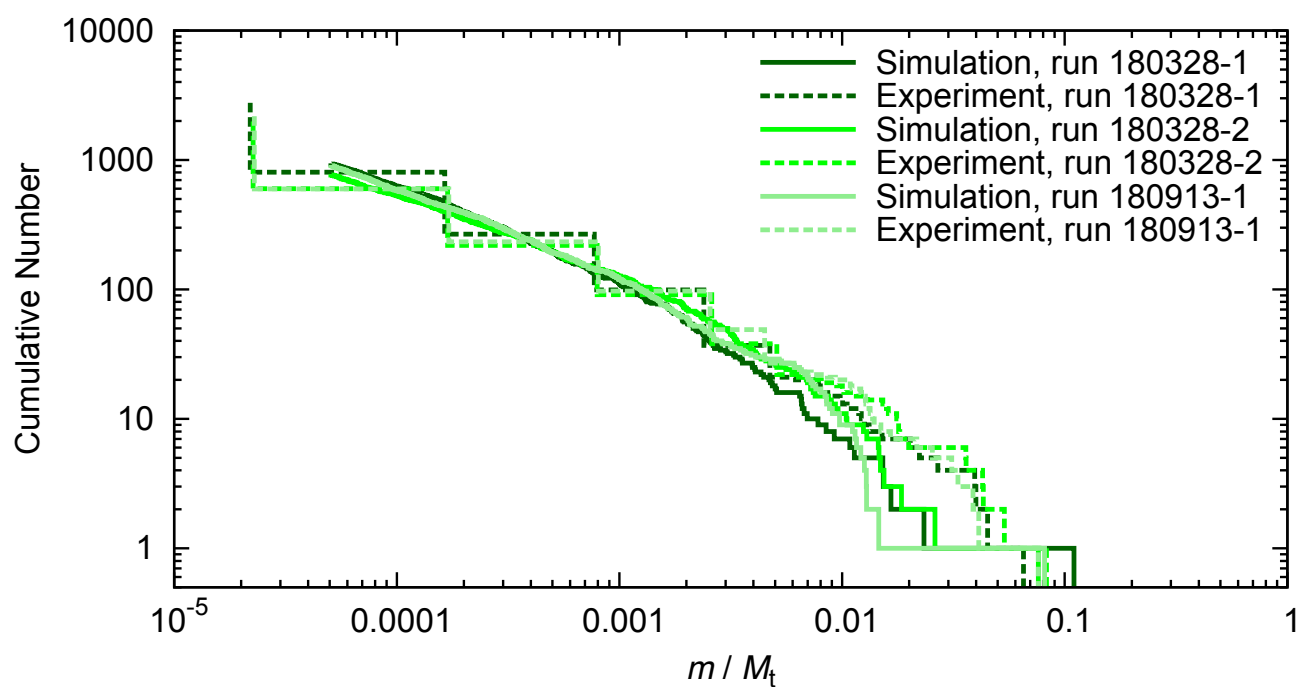
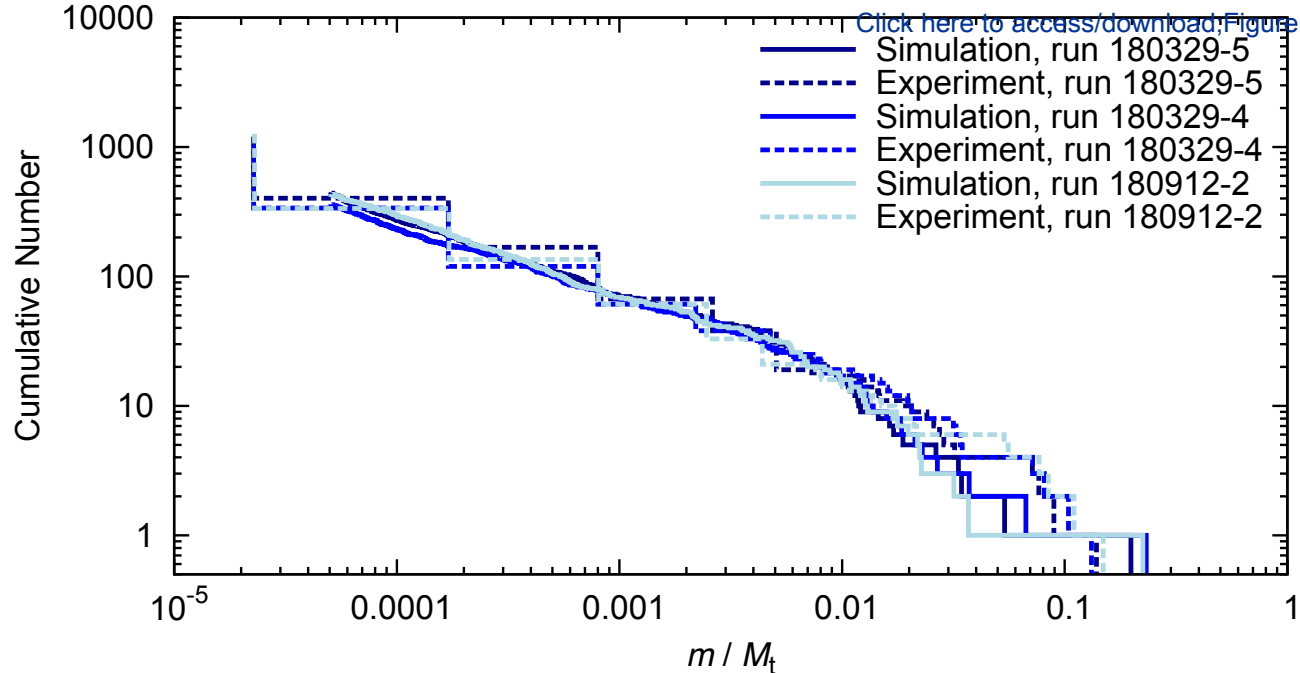
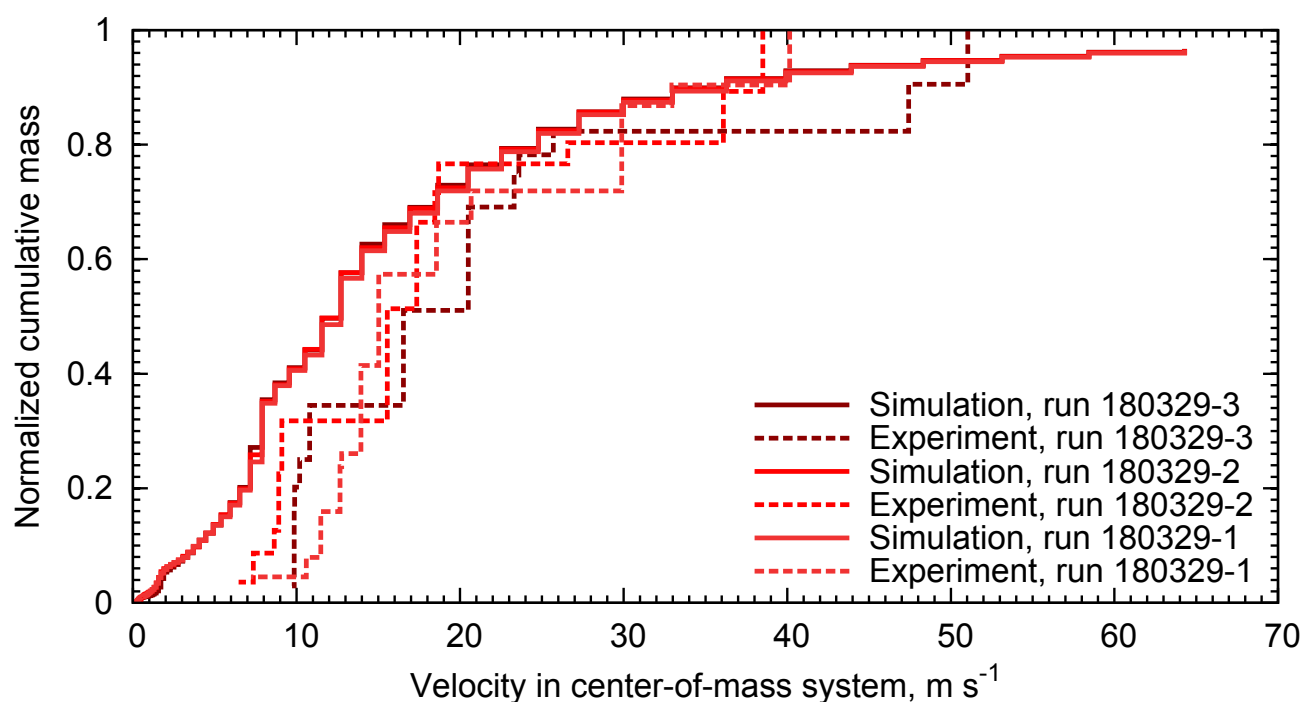
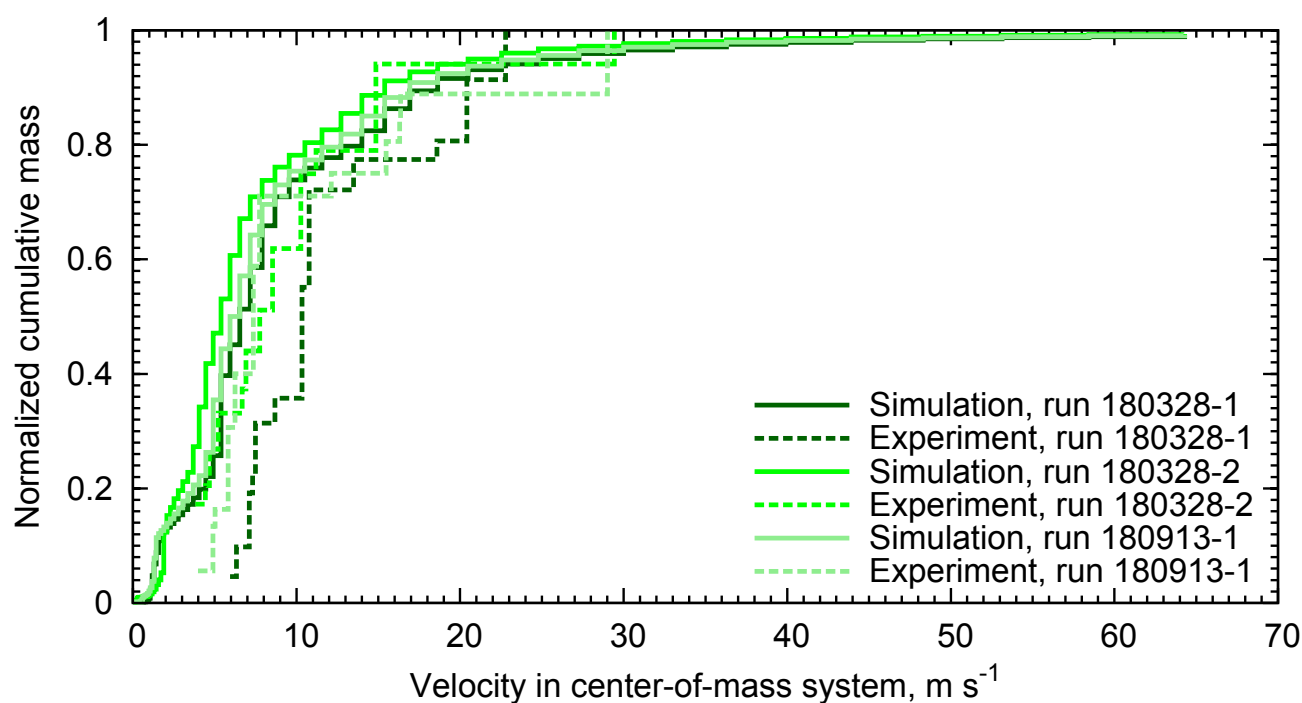
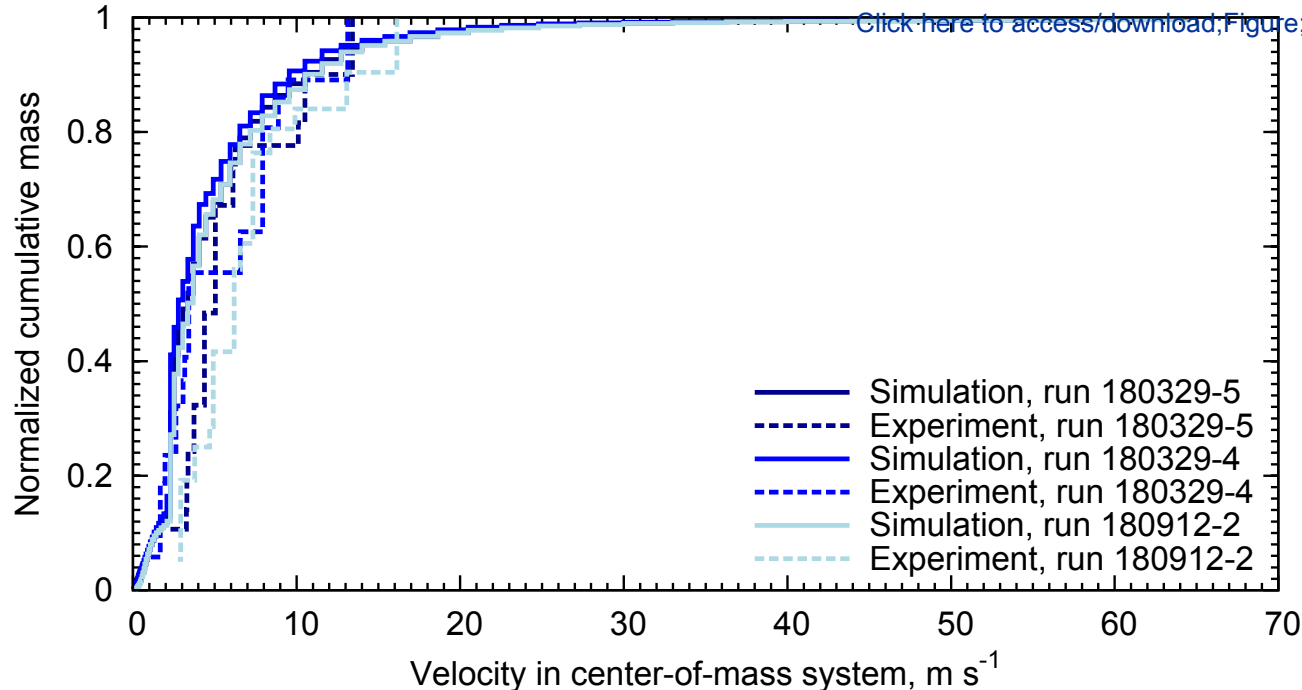
[Click here to access/download:Figure,fig23.eps](#)

Figure24

[Click here to access/download;Figure;fig24.eps](#)



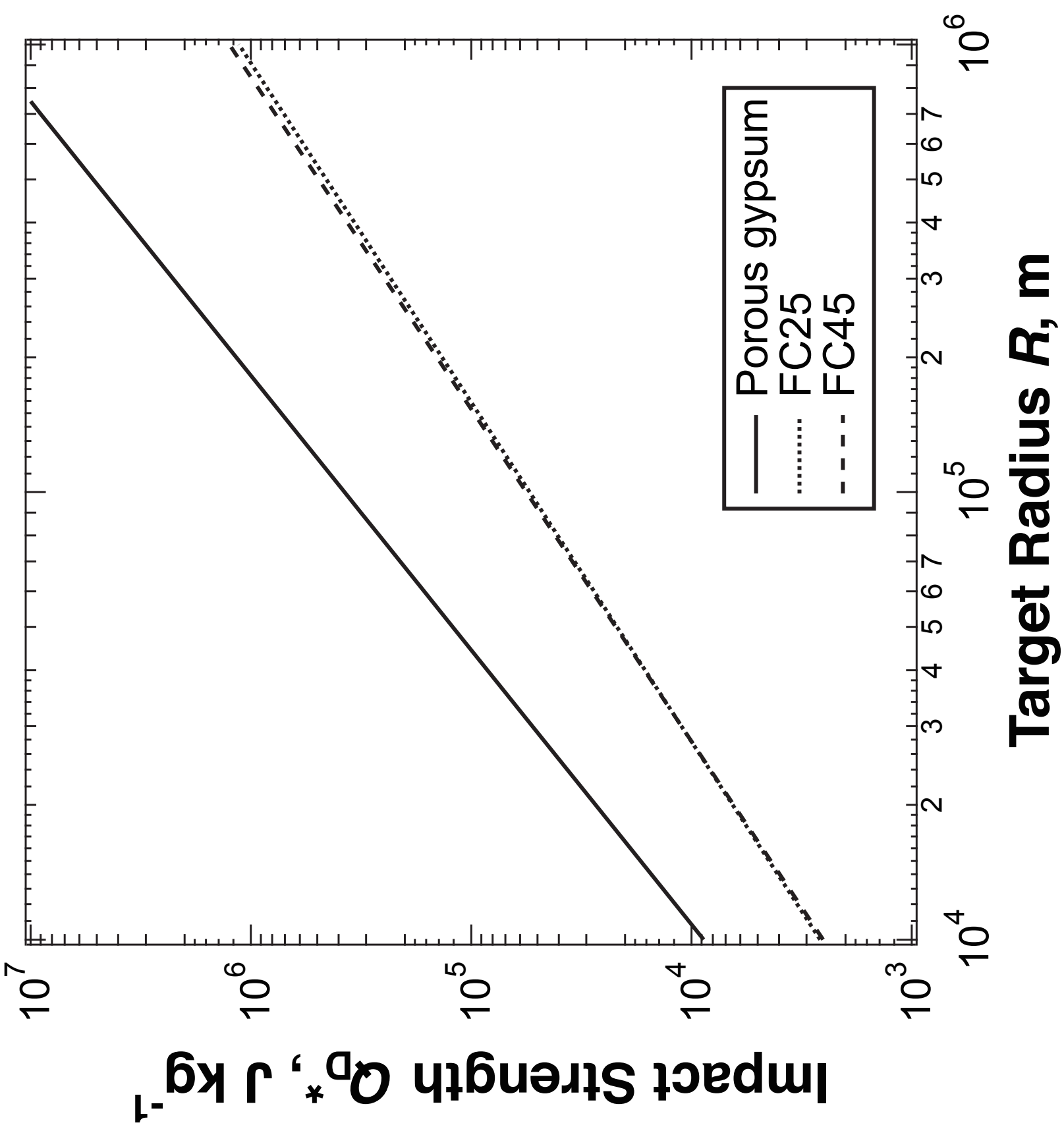
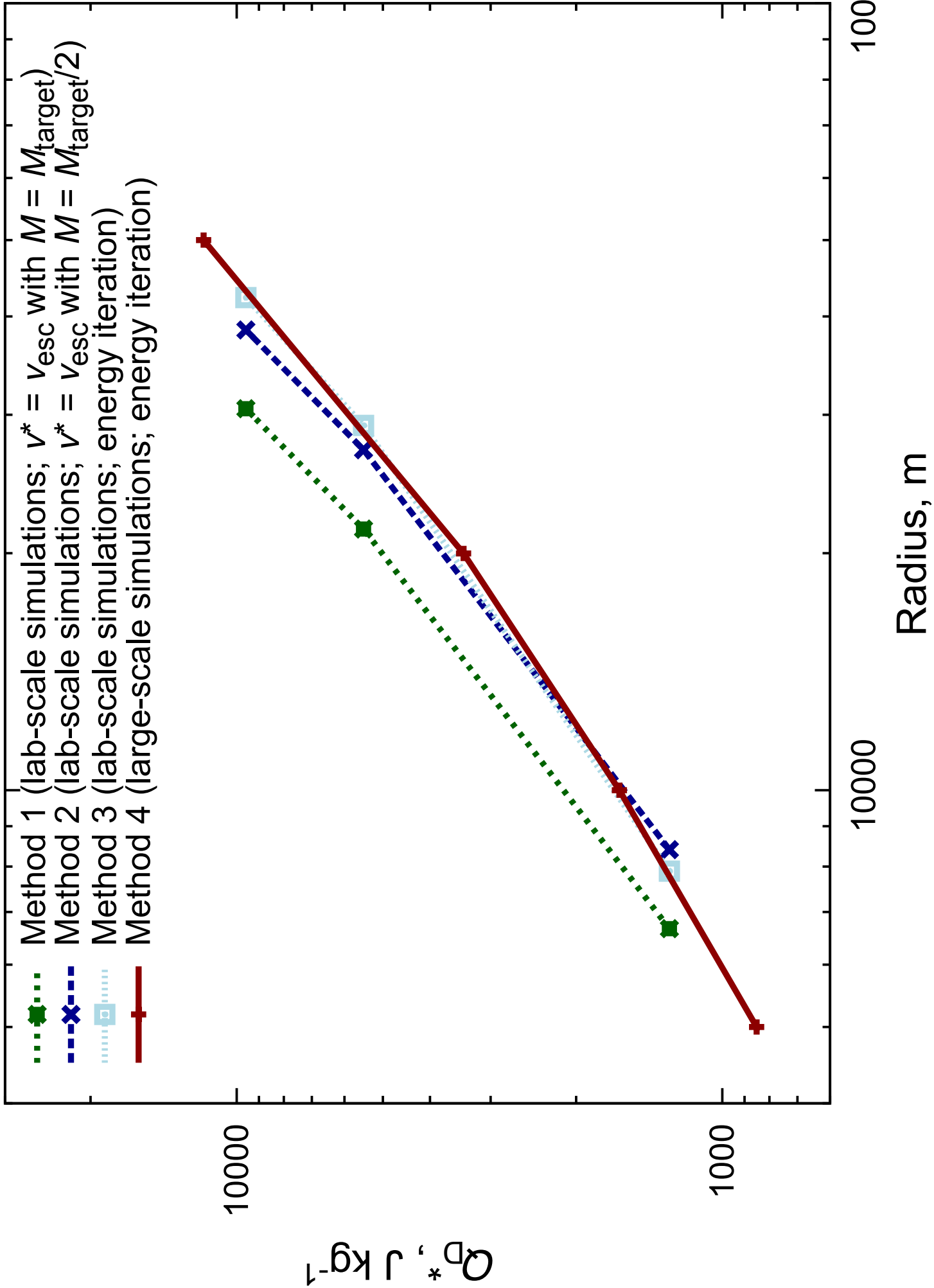
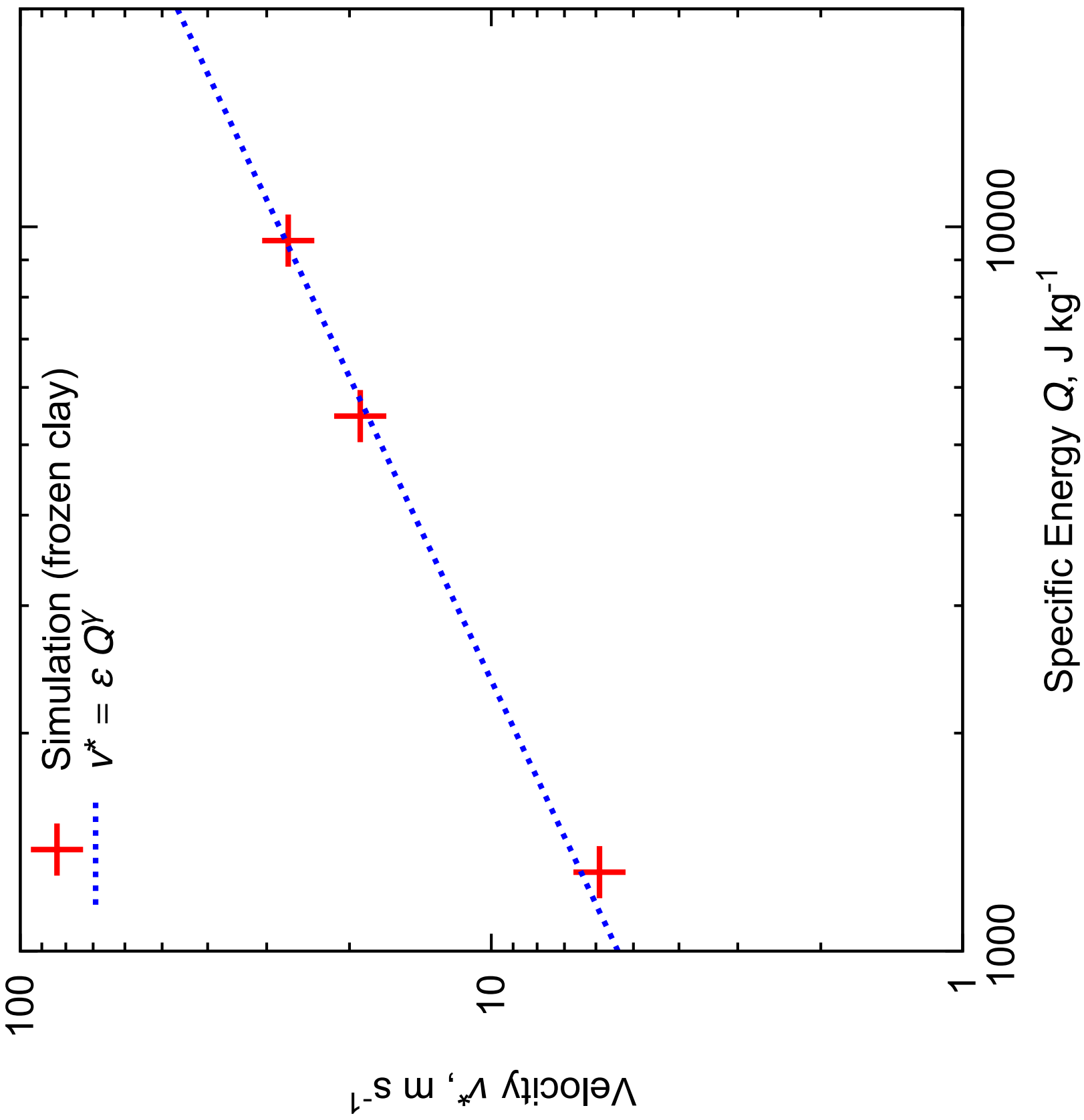


Figure26





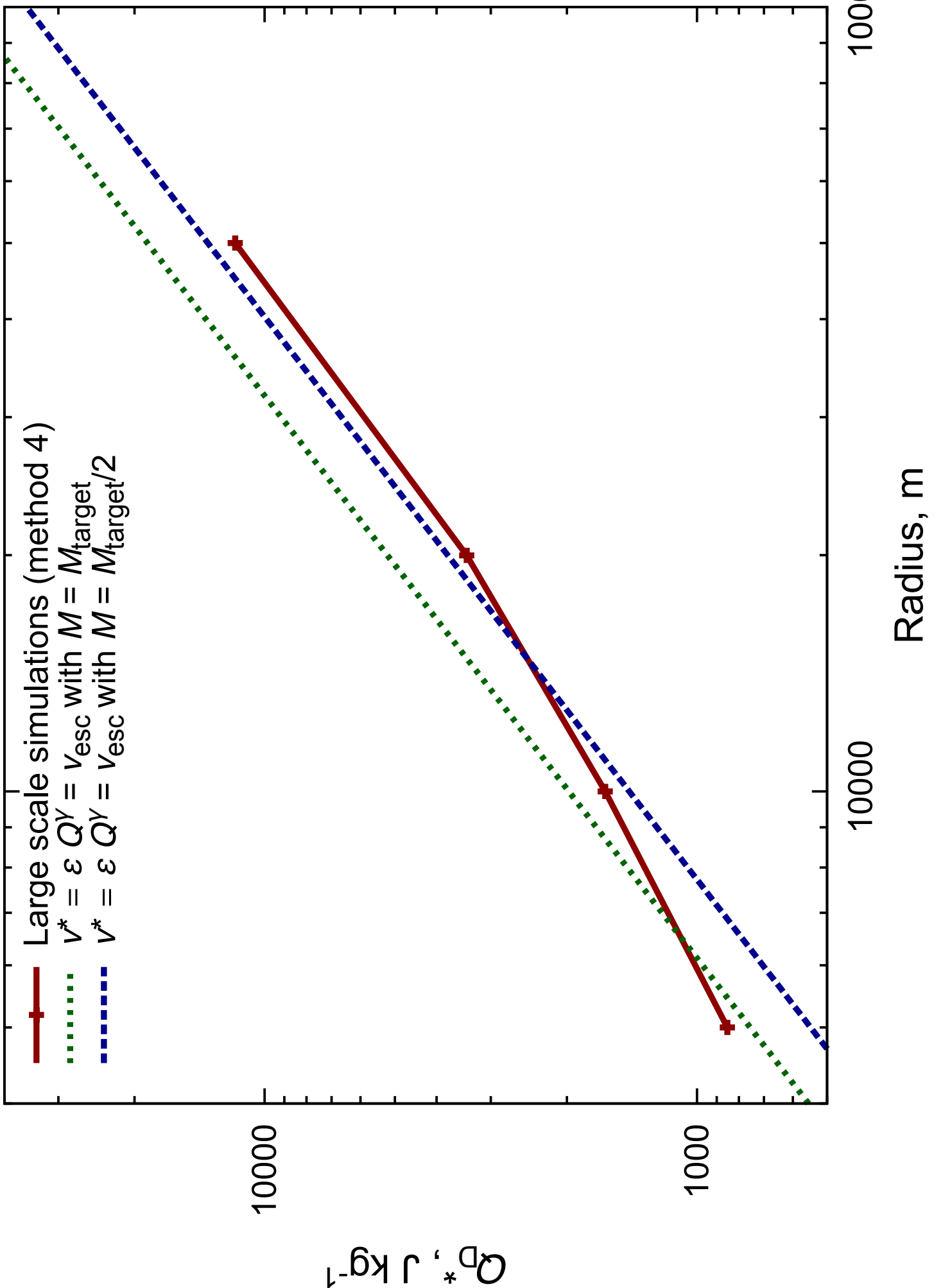


Table 1 Experimental conditions and results

Run number	Target mass	Impact velocity	Specific Energy	Largest fragment	θ , °	ϕ , °	Trigger timing of flash X-ray, μ s			v_a , m s ⁻¹	v_g , m s ⁻¹	v^* , m s ⁻¹
	M_t , g	v_i , km s ⁻¹	Q , J kg ⁻¹	mass m_l , g			CH3	CH2	CH1			
Frozen clay (water content: 25 wt.%)												
170607-5	205.1	4.17	9.68×10^3	–	90	7	100	500	1000	21.7	4.6	26.0
170608-3	205.5	3.17	5.57×10^3	5.1	94	-2	51	251	751	11.6	3.5	15.2
170609-1	205.9	1.54	1.32×10^3	161.5	90	–	98	498	998	–	1.7	–
170609-3	200.7	2.13	2.57×10^3	21.0	92	2	102	502	1002	5.7	2.4	8.3
170609-5	197.5	3.14	5.69×10^3	7.4	94	3	100	500	1000	14.2	3.6	17.8
170725-2	208.4	3.97	8.64×10^3	10.0	89	10	50	250	750	11.8	4.3	19.9
170725-5	204.1	3.28	5.99×10^3	13.4	81	9	100	500	1000	12.6	3.7	16.7
171025-2	213.2	4.25	9.66×10^3	8.1	–	–	150	750	750	–	4.5	21.6
171110-1*	95.1	2.78	2.76×10^3	20.77	78.4	–	–	–	–	3.3	1.98	–
171110-3*	45.0	2.80	5.92×10^3	3.8	81.1	–	–	–	–	10.4	4.23	–
Frozen clay (water content: 35 wt.%)												
170127-1*	19.5	1.75	5.37×10^3	0.84	–	–	–	–	–	–	6.12	–
170131-1*	202.9	4.91	4.03×10^3	16.76	–	–	–	–	–	–	1.64	–
170131-2*	195.9	6.83	8.09×10^3	11.45	–	–	–	–	–	–	2.37	–
170223-3	188.6	3.00	5.44×10^3	11.0	79	10	100	499	999	9.7	3.6	13.0
170224-1	191.7	2.89	4.96×10^3	–	83	-6	49	249	749	16.0	3.4	14.7
170224-2	190.5	5.91	2.09×10^4	–	90	-4	50	250	750	31.6	7.1	35.1
170224-3	187.9	5.98	2.17×10^4	–	90	6	100	500	1000	32.4	7.3	39.8
170607-1	189.1	4.27	1.10×10^4	–	82	-2	50	250	750	23.1	5.1	24.0
170607-2	186.3	4.32	1.14×10^4	–	87	14	100	500	1000	23.2	5.3	–
170725-3	188.1	3.68	8.19×10^3	–	90	0	100	500	1000	19.0	4.5	22.0
170726-4	191.5	1.88	2.10×10^3	9.0	98	–	248	748	1498	7.5	2.2	6.2
Frozen clay (water content: 45 wt.%)												
170607-4	167.3	4.22	1.21×10^4	–	98	–	50	250	750	36.5	5.8	–

[illegible]

171026-6	125.5	3.35	1.02×10^4	–	–	–	50	750	750	14.9	6.1	8.8
180328-1	126.3	3.30	9.81×10^3	8.2	90	9	51	501	501	15.0	5.9	9.9
180328-2	122.7	2.85	7.57×10^3	10.2	105	-7	48	999	998	10.0	5.3	7.6
180328-3	122.6	3.28	9.99×10^3	5.1	92	-1	–	87	87	16.0	6.1	10.3
180329-1	122.4	5.35	2.66×10^4	7.1	90	-6	51	501	501	–	9.9	14.5
180329-2	122.0	5.29	2.61×10^4	2.4	90	3	26	251	251	23.0	9.9	15.1
180329-3	122.5	5.26	2.57×10^4	2.6	92	-4	26	751	751	22.0	9.8	16.2
180329-4	121.8	1.92	3.47×10^3	16.1	93	13	48	498	498	9.0	3.6	3.3
180329-5	121.9	2.09	4.08×10^3	16.9	86	-6	102	1002	1002	14.0	3.9	4.4
180330-1	122.4	2.02	3.80×10^3	27.0	81	–	251	2001	–	–	3.8	–
180330-2	122.5	1.98	3.63×10^3	17.9	90	4	251	2001	2000	10.0	3.7	5.2
180330-3	121.8	3.29	1.01×10^4	7.4	88	9	51	251	251	13.0	6.2	6.1
180912-1	121.7	1.97	3.63×10^3	14.0	100	–	–	–	–	–	3.7	–
180912-2	120.8	2.12	4.23×10^3	18.0	100	5	502	1002	1002	7.0	4.0	5.7
180912-3	121.6	1.89	3.33×10^3	16.4	98	23	999	2000	1999	6.0	3.5	5.6
180913-1	121.2	3.06	8.79×10^3	9.2	91	18	251	501	501	13.0	5.7	6.8
180913-2	120.7	3.05	8.76×10^3	5.3	80	1	501	1001	1001	12.0	5.7	7.6
180913-3	121.7	5.18	2.51×10^4	4.1	94	-15	56	306	306	21.0	9.7	14.5
180913-5	120.9	5.16	2.51×10^4	3.5	94	-18	501	751	751	24.0	9.7	16.0
180914-1	120.6	5.14	2.49×10^4	2.3	78	-2	251	501	501	21.0	9.7	16.6

* The experiments were conducted by using the two-stage light gas gun in a cold room at Kobe University to obtain the impact strength Q_s^* .

θ and ϕ are an impact angle defined in Fig. 8a and c, respectively.

CH1, CH2 and CH3 are a channel number of a flash X-ray illustrated in Fig.3c.

v_a , v_g and v^* are an antipodal velocity, a velocity of a center-of-mass, and a median velocity, respectively.

Table 2 Physical properties of the targets and fitted parameters for Eq. (6)

Target	ε	γ	Bulk density ρ , g cm ⁻³	Tensile strength Y , MPa	Bulk sound velocity C_0 , kms ⁻¹	Shattering strength Q_s^* , J kg ⁻¹
FC45	$10^{-1.54 (\pm 0.22)}$	$0.742(\pm 0.061)$	1.67	1.10	2.38	705
FC35	$10^{-1.68 (\pm 0.21)}$	$0.758(\pm 0.053)$	1.57	-	-	198**
FC25	$10^{-1.64 (\pm 0.30)}$	$0.758(\pm 0.079)$	1.42	2.24	2.19	198**
FCs	$10^{-1.45 (\pm 0.15)}$	$0.710(\pm 0.041)$	-	-	-	-
FC _{num} ***	$10^{-1.42}$	0.72	-	-	-	-
Porous gypsum	$10^{-1.52 (\pm 0.20)}$	$0.613(\pm 0.050)$	1.12	2.3*	1.42*	760

* These data are from *Yasui et al.*, 2020.

** FC25 and FC35 were fitted **together** by Eq. (4) to determine Q_s^* .

*** **FC_{num}** was obtained from the numerical simulations for frozen clays.

Table 3 Additional simulation for the determination of Q_s^* .

Target	Impact velocity v_i , km s ⁻¹	Specific energy Q , J kg ⁻¹	m_i/M_t	Shattering strength Q_s^* , J kg ⁻¹
FC45	2.43	794	0.22	476
FC45		397	0.57	
FC25	2.8	4091	0.2	1550
FC25		2058	0.44	

Note: Constant velocity is used rather than constant mass ratio as in the laboratory experiments.